University of Southampton

Magnetization Reversal Processes in “Bottom-Up” and “Top-Down” Magnetic Nanostructures

by

Alexander Goncharov

Thesis submitted for examination for the degree of
Doctor of Philosophy

School of Physics and Astronomy
March 2005

ACKNOWLEDGMENTS

First, I would like to thank my supervisor Professor Peter de Groot for giving me the opportunity to commence my studies and for his continuous help and support over this period. I am very grateful to Alexander Zhukov, Senior Research Fellow, for his extensive help in understanding of the nature of magnetism and experiment.

I am also thankful to our technical support staff - Denis, Colin, Tom for their patience and always willing to help.

Many thanks go to Kestas, Salvita, Vassili and Alexei for being my friends.

Finally I am very grateful to Alya, my parents Vassili and Riya and my sister Irina. Without their love and support writing of this thesis could have been much more difficult task.

UNIVERSITY OF SOUTHAMPTON

ABSTRACT

FACULTY OF SCIENCE

SCHOOL OF PHYSICS AND ASTRONOMY

Doctor of Philosophy

Magnetization Reversal Processes in "Bottom-Up" and "Top-Down" Magnetic Nanostructures

by Alexander Goncharov

In this thesis results are presented on the experimental investigation of reversal mechanisms in magnetic nanostructures prepared both using "bottom-up" and "top-down" techniques. Highly ordered magnetic dot arrays and anti-dot networks of Ni, Co and CoPt on sub-micron scales have been prepared using self-assembly single and double template methods. This technique enabled us to create highly ordered magnetic dot and anti-dot nanostructures with 3D architectures on length scales ranging from 20 – 1000 nm. We found that patterning transverse to the film plane, which is a unique feature of this method, results in novel magnetic behaviour. The coercive field B_c, was found to demonstrate an oscillatory dependence on film thickness in anti-dot structures. The magnetization curves of our dot arrays reveal a wealth of different behaviour depending on array parameters. Varying the parameters in the preparation (sphere diameter, film thickness and composition) allows us to produce materials with predetermined magnetic parameters. Results have been interpreted using simple domain wall models and 3D micromagnetic simulations. The self-assembly template technique offers the potential of a low-cost preparation method for sub-micron patterned magnetic media.

We also studied arrays of different NiFe nanostructures prepared using e-beam lithography. This includes square arrays of anti-dots with various diameters, nano-dots with elliptical shape and aspect ratio a/b ~ 2, arrays of nano-rings with round and square shapes. Magnetic properties are strongly affected by the shape of the nano-elements. Experimental investigation of the azimuthal behaviour of the coercivity with the magnetic field applied in the plane of the film revealed that magnetostatic energy plays a vital role in the properties of the switching field.

All nanostructures in this project have been characterized by bulk magnetometry, MOKE and MFM.

Chapter 1. Introduction

Properties of bulk nanostructured magnetic materials have been studied for more then sixty years[1,2,3,4,5]. Fabrication of thin nanostructured films remained quite a challenging task until the early 1970's when a big progress in deposition techniques had been made. Further progress in fabrication of micron and sub-micron magnetic structures has been made recently, allowed studying magnetic properties in nanostructures with scales comparable to main magnetic length scales (magnetic domain wall width, exchange length etc.). Fundamental studies of such structures reveal significant changes in magnetic properties. For example, a magnetization reversal mechanism in nanostructures with characteristic length scale comparable to a domain wall width can change drastically. In addition to the size dependence, magnetic behaviour in nano-scale materials is well affected by an order in the structure; shape of the elements or structure itself and by interaction between nanoelements (such as exchange or dipolar coupling). From technological point of view, magnetic nanostructured materials are important in applications such as magnetic recording[6] and magnetic random access memory (MRAM)[7]. Continuous miniaturization of nanostructures has led to a significant growth in magnetic recording density over last forty years and now reaching value of 100 Gbit per square inch[6]. However, continuous increase in the recording density is limited by enhancement of thermal effects resulting in so-called superparamagnetic limit. This fact drives scientist to develop other methods of recording such as perpendicular recording or patterned recording media[6].

Modern fabrication techniques in nanotechnology can be divided into two general classes: "bottom-up"- nanostructuring process starts from a substrate, and "top-down" – when nanostructuring starts from the top of the film. The central method in the "top-down" class is an e-beam lithography combined with lift-off, mask or etching techniques[8]. This method is very flexible to shapes of designed nanostructures and produces samples with an excellent order. The main disadvantage of "top-down" techniques is high cost, which limits their application to fundamental research. Nanostructures from “bottom-up” methods are often prepared by deposition of materials through templates. Various types of templates have been used up to now in nano-fabrication, such as molecular, liquid crystals or templates from self-assembled spheres. More information about preparation methods can be found in Ref. 8.

There are several different types of nanostructures such as particle arrays, arrays of anti-dots, thin films, multilayered films, nano-clusters and nanowires[9]. Recent studies revealed a rich variety of interesting magnetic behaviour in these structures. For example, magnetic switching process in arrays of nano-scale magnetic dots, which are candidates for the high-density patterned magnetic recording media, has been studied experimentally and numerically. Results showed that reversal process is well dependent on the shape, aspect ratio, and lateral size of the dot[10,11]. Effects of intra-dot coupling in arrays have been also studied experimentally and theoretically[12,13]. Results showed that the magnetostatic interaction, arising from the high-order dot magnetic multipole moments, plays an important role in the magnetization reversal process of periodical arrays of close-packed dots. Two-dimensional arrays of sub-micron holes (antidots) in continuous ferromagnetic films have also been studied extensively[14,15,16,17]. This interest has been stimulated by the prospectives of such anti-dot systems for magnetic storage aplications[18,19]. It has been found that magnetization reversal mechanism in anti-dot structures occurs through formation of domain walls, which is different from the dot reversal[20,21]. One more important class of nanostructures, that have promising prospects in MRAM application, is nano-rings. They have attracted much attention due to their shape, which eliminates a highly energetical vortex core in the reversal process. Recently switching process has been studied in single ferromagnetic rings[22,23] and in arrays of interacting rings[24,25]. These studies revealed that reversal in the rings occurs through two quasi-saturated states known as an “onion state” and a vortex state. But in contrast to the known vortex state observed in circular dots now the vortex is formed without any core.

In this work we have investigated magnetic and transport properties in nanostructures prepared using “bottom-up” and “top-down” techniques. We analyze details of the magnetic reversal mechanism, its dependence on nanostructure parameters. Analysis of experimental results is supported by numerical simulations.

Chapter 3 presents survey of sample preparation techniques as well as experimental facilities for investigation and characterization of nanostructures, used in this work. We give a brief review of self-assembly and e-beam lithography methods.

Magnetization reversal mechanism and its dependence on the array parameters such as period, film thicknesses etc. are described in chapter 4. We report on oscillatory thickness dependence of the coercive field in anti-dot structures, coercivity dependence on the hole diameter and magnetic anisotropy inside domains that have hexagonal shapes. Also, 2D and 3D models of the domain wall pinning are described. Finally, the results on reversal mechanism in quasi-spherical dots are presented.

Chapter 5 is devoted to investigation of switching processes in nanostructures prepared by e-beam lithography. We present experimental studies of an in-plane anisotropy of the coercive field in 2D arrays of elliptical dots, nano-rings, and anti-dots accompanied by micromagnetic simulation results. In the last paragraph of chapter 5 we discuss magneto-transport properties of the square array of connected nano-rings. At the beginning a brief introduction into the anisotropic magnetoresistance (AMR) mechanism in transition metals is given. Results on magnetoresistive measurements are presented for different directions of the magnetic field and the electric current.

References

---

[1] C. Kittel, Rev. Mod. Phys. **21**, 541 (1949)

[2] W.F. Brown, Jr., Phys. Rev. **105**, 1479 (1957)

[3] E.H. Frei, S. Shtrikman, and D. Treves, Phys. Rev. **106**, 446 (1957)

[4] A. Aharoni, Rev. Mod. Phys. **34**, 227 (1962)

[5] E.H. Frei and W.F. Brown, Jr., J. Appl. Phys. **39**, 993 (1968)

[6] A. Moser et al. J. Phys. D: Appl. Phys. **35** R157 (2002)

[7] J. G. Zhu, and Y. Zheng, and G.A. Prinz, J. Appl. Phys. **87**, 6668 (2000)

[8] J.I. Martin et al. J. Magn. Magn. Mater. **256**, 449 (2003)

[9] R. Skomski J. Phys.: Condens. Matter **15**, R841 (2003)

[10] R.P. Cowburn et al. Phys. Rev. Lett. **83**, 1042 (1999)

[11] T. Shinjo et al., Science **289**, 930 (2000)

[12] V. Novosad et al. Phys. Rev. B **65**, 060402-1 (2002)

[13] K. Yu. Guslienko Phys. Lett. A. **278**, 293 (2001)

[14] I. Guedes et al. Phys. Rev. B **66**, 014434-1 (2002)

[15] I. Guedes et al. Phys. Rev. B **62**, 11719 (2000)

[16] P. Vavassori et al., Phys. Rev. B **59**, 6337 (1999)

[17] C. A. Grimes et al., J. Appl. Phys. **81**, 4720 (1997)

[18] R.P. Cowburn, A.O. Adeyeye, and J.A. Bland, Appl. Phys. Lett. **70**, 2309 (1997)

[19] R.P. Cowburn et al. J. Magn. Magn. Mater. **173**, 193 (1997)

[20] A.A. Zhukov et al. J. Appl. Phys. **93,** 7322 (2003)

[21] A.A. Zhukov et al. J. Mag. Mag. Mat. **272-276,** 1621 (2004)

[22] S.P.Li, et al. Phys. Rev. Lett. **86**, 1102 (2001)

[23] J. Rothman, et al. Phys. Rev. Lett. **86**, 1098 (2001)

[24] U. Welp, et al. J. Appl. Phys. **93**, 7056 (2003)

[25] U. Welp, et al. Phys. Rev. B, 054408-1 (2003)

Chapter 2. Magnetism in nano-structures

2.1 Basics of ferromagnetism

Until Weiss, in 1906, developed his hypothesis of the molecular field in ferromagnetic materials, nobody could explain such a high saturation value of magnetization in iron at low fields compared to paramagnetic materials. In his theory the molecular field, which can magnetize a substance to saturation in the absence of a magnetic field, is proportional to the magnetization[1]:

$$\mathbf{H}_m = \eta \mathbf{M} \tag{2.1}$$

where η is the molecular field coefficient. The second assumption that Weiss made is that a ferromagnet, in the demagnetized state is divided into domains – small regions in which magnetization is saturated to M_S. The direction of the magnetization in various domains is different leading to a zero net magnetic moment. The magnetization process takes place through movement of domain walls, which increases sizes of domains with the magnetization having a direction favorable with the applied field until the sample becomes a large single domain. Finally the magnetization of the domain rotates to the applied field direction and the substance saturates. Molecular field theory explained the phenomenology of ferromagnetism but it did not give insight into the physical origin of this field. Attempts to assign the molecular field to the pure magnetic dipolar field failed because the value of the molecular field in iron at least is 1000 times larger. Later, in 1928, the physical origin of the molecular field proved to be the quantum mechanical exchange interaction[1]. The exchange forces can be easily understood by considering the hydrogen molecule with covalent bonding. There are attractive Coulomb interactions between electrons and protons and repulsive interaction between two electrons or two protons. But there is another non-classical force or exchange force arising from the Pauli exclusion principle and from the fact that electrons are indistinguishable. Let us consider the case of two indistinguishable non-interacting electrons. The full wavefunction of this system consists of spatial and spin parts:

$$\Psi = \varphi(r)\chi(S) \tag{2.2}$$

Where Ψ must be antisymmetric – to Fermi-Dirac statistics. The spin wavefunction also has two forms - symmetric for the triplet state ($S=1,\ 2S+1=3$) or antisymmetric for the singlet state ($S=0,\ 2S+1=1$). The Pauli exclusion principle for fermions requires that the total wavefunction should be antisymmetric or in other words if the spatial function is symmetric then the spin function must be antisymmetric and vice versa. From this we can write two possible total wavefunctions corresponding to triplet and singlet states for this system:

$$\Psi_S = \sqrt{\frac{1}{2}}\left[\varphi_1(1)\varphi_2(2)+\varphi_1(2)\varphi_2(1)\right]\chi_S \tag{2.3}$$

$$\Psi_T = \sqrt{\frac{1}{2}}\left[\varphi_1(1)\varphi_2(2)-\varphi_1(2)\varphi_2(1)\right]\chi_T \tag{2.4}$$

where T and S are denoting triplet and singlet functions and $\varphi_1(1)$ means electron 1 in the state 1 and so on. If interaction between electrons is considered one can obtain for energies in these two states[2]:

$$E_S = E_0 + C_{ij} + J_{ij} \text{ and } E_T = E_0 + C_{ij} - J_{ij} \tag{2.5}$$

here C_{ij} and J_{ij} are Coulomb and exchange integrals[2]:

$$C_{ij} = \int \varphi_i^*(1)\varphi_j^*(2)\left(\frac{e^2}{r_{12}}\right)\varphi_i(1)\varphi_j(2)dv \tag{2.6}$$

$$J_{ij} = \int \varphi_i^*(1)\varphi_j^*(2)\left(\frac{e^2}{r_{12}}\right)\varphi_i(2)\varphi_j(1)dv \tag{2.7}$$

With integration over the whole ferromagnetic body. J_{ij} gives the value of the exchange interaction for two electrons in states i and j. Depending on the sign of J_{ij}, the ground state can be either a singlet or triplet one. Using this phenomenology we can explain appearance of ferromagnetism in $3d$ metals. Fig. 2.1 shows the Bethe-Slater curve describing the variation of the exchange integral with the ratio r_a/r_{3d}. Here r_a is the atom radius and r_{3d} the radius of $3d$ shell of electrons because d-electrons are responsible for ferromagnetism in metals.

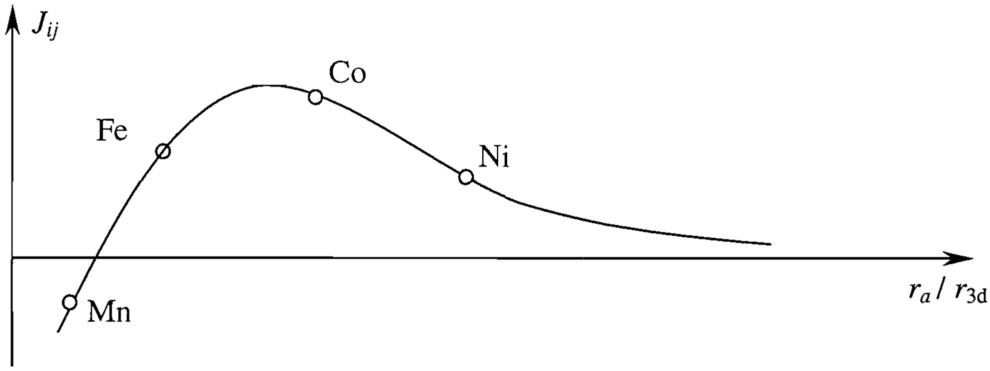

Fig. 2.1 Bethe-Slater curve (schematic representation)

As can be seen from, the figure, for materials with large distances between atoms the ground state is a triplet and the exchange integral is positive. If we bring atoms of the same kind closer, exchange forces favoring parallel spins, increase and reach maximum. If the distance further decreases, the ground state becomes a singlet with a negative exchange integral. This behaviour can be understood if we analyze the properties of the wavefunction. It can be shown that if interatomic distance is large, the triplet state has the lower energy while for close packed atoms the spatial part of the wavefunction becomes symmetric leading to antisymmetric spin part (singlet). This behaviour is caused by an overlap of electronic orbitals[1,2]. The Bethe-Slater curve separates ferromagnetic metals like Fe, Co, Ni from the 3*d* elements with lower *Z*, like Mn and Cr.

In order to explain observed experimental values for μ_{at} at zero temperature for Ni, Fe and Co - 0.6, 2.22, and 1.72 Bohr magnetons respectively, we should consider band structures of solids. We know that in ferromagnetic Ni, for example, all shells from 1*s* to 3*p* are filled and electrons only occupy 8 from 10 electronic states in the 3*d*-shell having 5 electrons in spin-up states and 3 in spin-down. So the spin imbalance is 2, which is not consistent with the experimental value for μ_{at}. But the real structure of electronic states in metals is much more complicated than that we have discussed before. When atoms are brought together in a crystal lattice, discrete electronic states broaden to bands due to overlapping of electronic orbitals. Let us consider the simplest case of modified 1*s* orbital containing two electrons in spin-up and spin-down states. If the distance between two atoms is reduced to a value allowing for 1*s* orbitals to overlap, then from Pauli exclusion principle the single 1*s* level should split into two with two electrons in each state. Similarly if we have N atoms then each level should split into *N* levels and form a band. Fig. 2.2 shows a schematic representation of the density of states for 3*d* metals. Ni contains 10 electrons in outer 4*s* and 3*d* shells. So the Fermi level drawn in the picture is just below the top of the 3*d* band. This mixing of *d* and *s* states results in crystalline Ni having 9.4 electrons occupying the *d*-shell and the remaining 0.6 electrons in the *s*-shell. Then the spin imbalance in the 3*d* shell would be 10 - 9.4 = 0.6. The exchange interaction shifts spin-up and spin-down states as shown in the figure giving rise to spontaneous magnetization. We can now summarize the criteria required for existence of ferromagnetism in metals as follows: first of all, the metal should have a large value of the exchange integral allowing for spontaneous magnetization to exist, and second there should be a large density of states at the Fermi level so that the increase in the energy due to the spin alignment will be small. This condition is known as the Stoner criterion. This criterion is fulfilled in cases of three elements: Ni, Fe and Co.

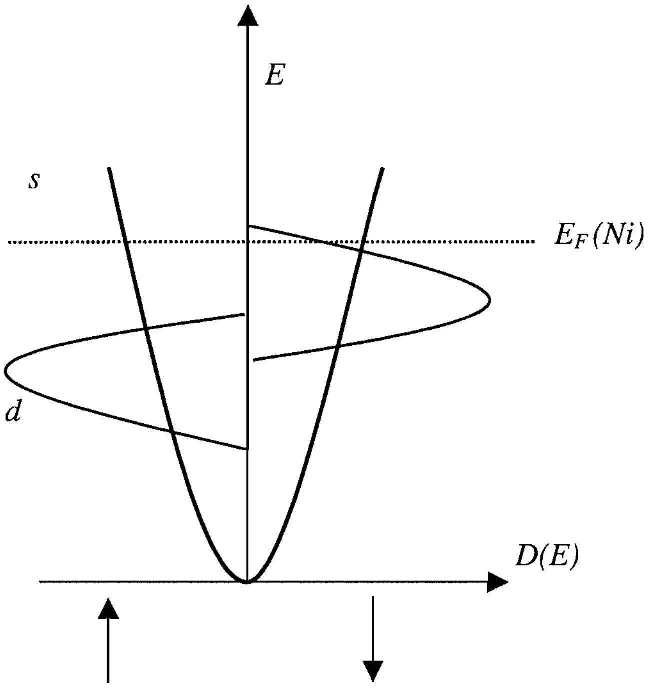

Fig. 2.2 A schematic representation of 4s and 3d bands for a transitional metal. The Fermi level corresponds to Ni. Exchange splitting for spin-up and spin-down states is shown only for 3d band.

2.2 Magnetic energy densities in micromagnetics

In our analysis of full energy we shall start from the exchange energy, already discussed in previous paragraph. It was shown that this energy has quantum mechanical origin and can be described by the Heisenberg Hamiltonian[3]: $H = -2\sum_{i>j} J_{i,j} \mathbf{S}_i \mathbf{S}_j$, with the exchange integral $J_{i,j}$. This is a fundamental result of quantum theory and we will use it to derive an equation for the exchange energy in the assumption that spins can be treated as classical vectors. In this approximation we can write exchange energy in terms of the angle between spin i and spin j:

$$E_{ex} = -2\sum_{i>j} J_{ij} \mathrm{S}^2 \cos\vartheta_{ij} \qquad (2.8)$$

Here, ϑ_{ij} is the angle between spins. The next very important approximation is interaction with the nearest neighbours when neighbouring spins misaligned by a small angle $\vartheta_{ij} << 1$. In this we can write for the energy loss from the state with all spins parallel[4]:

$$\Delta E_{ex} = 2J\mathbf{S}^2 \sum \left(1-\cos\vartheta_{ij}\right) \approx J\mathbf{S}^2 \sum \vartheta_{ij}^2 \qquad (2.9)$$

Because $\vartheta_{ij} << 1$ it can be expressed through unit vectors parallel to the local spins as: $\left|\vartheta_{ij}\right| \approx \left|\mathbf{s}_i - \mathbf{s}_j\right|$. Expanding this into the Taylor series for slowly changing ϑ_{ij} we can obtain approximation: $\left|\vartheta_{ij}\right| \approx \left|(q_i \cdot \nabla)\mathbf{s}\right|$, where q_i is the vector directed from lattice point *i* to *j*. Substituting this into the (2.9) and summing over the nearest neighbours in a cubic lattice with lattice constant *a*, we obtain for exchange energy[3,4]:

$$E_{ex} = JS^2a^2 \sum_i \left[(\mathbf{m}_i \cdot \nabla)\mathbf{s}\right]^2 = \frac{1}{2}C\left[(\nabla m_x)^2 + (\nabla m_y)^2 + (\nabla m_z)^2\right] \qquad (2.10)$$

Where $\mathbf{m}_i$ is a unit vector along the magnetization direction and $C = \frac{2JS^2}{a}k$ is the exchange constant describing the strength of the exchange interaction. This exchange constant is related to the exchange stiffness *A* as: *C* = *2A*. The difference in exchange constant for various crystal structures (bcc, hcp etc) is only in a multiplication factor *k*, which is 1 for the simple cubic lattice.

The next energy term is the magnetocrystalline anisotropy energy. This anisotropy acts in such a way that the magnetization tends to lie along particular crystallographic directions inside a ferromagnetic body. These directions are called directions of easy magnetization. The directions along which it is difficult to magnetize the material are called hard axis directions. The excess in the magnetic energy, which is required to saturate the material in hard direction, is the anisotropy energy. The magnetocrystalline anisotropy has a quantum mechanical origin. This includes coupling of the atomic orbitals to the given crystal field and spin-orbit interaction allowing for the spin to have only particular orientations relative to orbital moment **L**, (Ref. 2). The anisotropy of hexagonal crystals is uniaxial and depends only on one parameter, the angle θ between the easy axis (c-axis) and the magnetization direction. Mathematically it is written as follows[3]:

$$E_u = -K_1 \cos^2\theta + K_2 \cos^4\theta = -K_1 m_z^2 + K_2 m_z^4 \tag{2.11}$$

Here **m** is a unit vector along the magnetization direction and the *z*-axis is parallel to the easy *c*-axis. The energy is a function of even powers of $\cos\theta$ because of the symmetry – the easy direction is equivalent for +*θ* and – *θ*. For cubic anisotropy as in case of Ni and Fe the energy density is an expansion starting from the fourth power:

$$E_c = K_1(\alpha_1^2\alpha_2^2 + \alpha_2^2\alpha_3^2 + \alpha_3^2\alpha_1^2) + K_2\alpha_1^2\alpha_2^2\alpha_3^2 \tag{2.12}$$

Where $\alpha_1, \alpha_2, \alpha_3$ are directional cosines referring to the cube unit vectors.

Next we shall consider the magnetoelastic energy terms. This is another type of anisotropy, called magnetostriction, which arises from the interaction of the magnetization and mechanical strain of the lattice. The crystal lattice deforms depending on the magnetization in the ground state. To find out the nature of the magnetoelastic interaction we start from the total energy density including the elastic energy term[4]:

$$\begin{aligned} E &= K_1\left(\alpha_1^2\alpha_2^2 + \alpha_2^2\alpha_3^2 + \alpha_3^2\alpha_1^2\right) + \\ &+ B_1\left(\alpha_1^2 e_{xx} + \alpha_2^2 e_{yy} + \alpha_3^2 e_{zz}\right) + B_2\left(\alpha_1\alpha_2 e_{xy} + \alpha_2\alpha_3 e_{yz} + \alpha_3\alpha_1 e_{zx}\right) + \\ &+ \frac{1}{2}c_{11}\left(e_{xx}^2 + e_{yy}^2 + e_{zz}^2\right) + \frac{1}{2}c_{44}\left(e_{xy}^2 + e_{yz}^2 + e_{zx}^2\right) + c_{12}\left(e_{yy}e_{zz} + e_{xx}e_{zz} + e_{xx}e_{yy}\right) \end{aligned} \tag{2.13}$$

Here K_1 is the magnetocrystalline anisotropy constant, c_{ij} are elastic modules and e_{ij} are strains. Magnetoelastic coupling constants B_1 and B_2 are defined as:

$$\frac{1}{\alpha_i\alpha_j}\frac{\partial E_K}{\partial e_{ij}}=\begin{cases}B_1 \rightarrow i=j\\ B_2 \rightarrow i\neq j\end{cases} \tag{2.14}$$

Where E_K is the cubic anisotropy energy term. To find the equilibrium state we need to minimize this energy density with respect to strains e_{ij} by solving six linear equations[2,4]:

$$\frac{\partial E}{\partial e_{ii}}=B_1\alpha_i^2+c_{11}e_{ii}+c_{12}\left(e_{jj}+e_{kk}\right)=0$$
$$\frac{\partial E}{\partial e_{ij}}=B_2\alpha_i\alpha_j+c_{44}e_{ij}=0$$

(2.15)

Substituting values for e_{ij} found from equations (2.15) into the formula for strains $\frac{\delta l}{l}=\sum_{i\geq j}e_{ij}\beta_i\beta_j$, we can write for the strain in the direction $\vec{\beta}=\left(\beta_1,\beta_2,\beta_3\right)$ for the magnetization lying in the direction[4] $\vec{\alpha}=\left(\alpha_1,\alpha_2,\alpha_3\right)$:

$$\begin{aligned}\frac{\delta l}{l}=&\frac{3}{2}\lambda_{100}\left(\alpha_1^2\beta_1^2+\alpha_3^2\beta_3^2+\alpha_3^2\beta_3^2-\frac{1}{3}\right)+\\&+3\lambda_{111}\left(\alpha_1\alpha_2\beta_1\beta_2+\alpha_1\alpha_3\beta_1\beta_3+\alpha_2\alpha_3\beta_2\beta_3\right)\end{aligned} \tag{2.16}$$

With $\lambda_{100}=-\frac{2}{3}\frac{B_1}{c_{11}-c_{12}}$ and $\lambda_{111}=-\frac{1}{3}\frac{B_2}{c_{44}}$. In the case of an isotropic magnetostriction ($\lambda_{100}=\lambda_{111}$) the equation (2.16) is simplified[4]:

$$\frac{\delta l}{l}=\frac{3}{2}\lambda\left[\left(\alpha_1\beta_1+\alpha_2\beta_2+\alpha_3\beta_3\right)^2-\frac{1}{3}\right]=\frac{3}{2}\lambda\left(\cos^2\xi-\frac{1}{3}\right) \tag{2.17}$$

where ξ is the angle between the magnetization and direction of the stress. Effect of magnetostriction on the magnetic behaviour is that the mechanical stress induces additional anisotropy. The contribution in the second order of λ is described by equation[2]:

$$E = (K_1 + \Delta K_1) \cdot (\alpha_1^2\alpha_2^2 + \alpha_2^2\alpha_3^2 + \alpha_3^2\alpha_1^2) \tag{2.18}$$

with

$$\Delta K_1 = \frac{9}{4}\left[(c_{11} - c_{12})\lambda_{100}^2 - 2c_{44}\lambda_{111}^2\right] \tag{2.19}$$

This contribution does not depend on the sign of λ and is only dependent on the difference between λ_{100} and λ_{111}. This term should vanish in the case of isotropic magnetostriction. Furthermore, if the magnetocrystalline anisotropy is uniaxial, then it can be shown that the contribution to the anisotropy induced by the stress σ is given by the equation[2]:

$$K_{eff} = K_1 + K_{me} = K_1 - \frac{3}{2}\lambda\sigma \tag{2.20}$$

Hence, the magnetoelastic energy for the isotropic magnetostriction has a form[2,4]:

$$E_{me} = -\frac{3}{2}\lambda\sigma\cos^2\xi \tag{2.21}$$

Magnetostatic energy arises from the classical interactions between the volume and surface magnetic charges. This interaction leads to the fact that the field inside the ferromagnetic body is not the same as the field outside and the difference, which is called the demagnetizing field, is a function of the shape. In the case of uniformly magnetized sample (which can only be realized for an ellipsoid) the demagnetizing field can be written in the form:

$$H_d = -NM \tag{2.22}$$

where N in the general case is a second order tensor responsible for the anisotropic interaction. For particular case of uniform magnetization in the body, which has an ellipsoidal shape, this matrix has a diagonal form with a trace $N_x + N_y + N_z = 1$ in SI units, where values N_i are called demagnetizing factors for the x,y,z directions respectively. The magneto-static energy for the sample of volume V with homogeneous magnetization than can be evaluated as follows[3]:

$$E_m = \frac{1}{2}V\left(N_x M_x^2 + N_y M_y^2 + N_z M_z^2\right) \tag{2.23}$$

This magneto-static term is a sort of anisotropy energy, responsible for the shape effects in ferromagnetic samples. The shape anisotropy field is proportional to the difference in the demagnetizing fields for two orthogonal directions:

$$H_{shape} = M_s \Delta N \tag{2.24}$$

The shape anisotropy constant can be then evaluated by $K_{shape} = M_s^2 \Delta N / 2$ (see Ref. 2).

Zeeman energy is the potential energy of a magnetic moment in a magnetic field. This energy is written in a form:

$$E_Z = -\mu_0 \mathbf{M} \cdot \mathbf{H} \tag{2.25}$$

2.3 Magnetic properties of fine nano-particles

It is a well-known fact that ferromagnetic materials subdivide into domains to save the magnetostatic energy. Ferromagnetic domains are the regions in the magnetic material where direction of the magnetization remains constant. But formation of these domains costs exchange and anisotropy energies to rotate magnetic moments from one domain to another. Thus, in small particles formation of domains can become unfavorable and a single domain state occurs. We can estimate to the first approximation the critical radius for a spherical particle assuming that a single domain state appears when its radius becomes comparable to the domain wall width. More analytic approach gives for materials with large anisotropy constant K_u:

$$R_c \approx 9\frac{\sqrt{AK_u}}{\mu_0 M_s^2} \tag{2.26}$$

where A is the exchange stiffness and M_s is the saturation magnetization. If the magnetocrystalline anisotropy is weak than we should only estimate the cost in exchange energy to form domains. Now the cost in exchange energy is compared with magnetostatic energy, which is saved. This approach gives for the critical radius value[2]:

$$R_c \approx \sqrt{\frac{9A}{\mu_0 M_s^2}\left[\ln\left(\frac{2R_c}{a}\right)-1\right]} \tag{2.27}$$

The critical radius given by (2.27) is derived under the assumption that the magnetization is allowed to curl remaining parallel to the surface of the sphere.

Magnetization process in single domain particles can be studied by finding the magnetic configuration with the lowest energy, which includes terms described in previous section. Analytically this problem could be solved if we solve Brown's differential equation derived in Ref. 3:

$$\mathbf{m}\times\left(C\nabla^2\mathbf{m}+M_s\mathbf{H}-\frac{\partial w_a}{\partial\mathbf{m}}\right)=0 \qquad (2.28)$$

With boundary conditions on the surface:

$$\mathbf{m}\times\left(C\frac{\partial\mathbf{m}}{\partial n}+\frac{\partial w_s}{\partial\mathbf{m}}\right)=0 \qquad (2.29)$$

Here w_s and w_a are surface and volume anisotropy energy densities. These equations mean that in the ground state the torque is zero and the magnetization is parallel to an effective field:

$$\mathbf{H}_{eff}=\frac{C}{M_s}\nabla^2\mathbf{m}+\mathbf{H}-\frac{1}{M_s}\frac{\partial w_a}{\partial\mathbf{m}} \qquad (2.30)$$

Solving this set of linear equations is known as the nucleation problem. The analysis is started from the completely saturated state and then the field is slowly reduced. The nucleation field is defined as the field when the saturated state becomes unstable and changes in the magnetization state occur. The nucleation process in fine particles has been studied by the linearization of the Brown's equation under the assumption that the magnetic field is homogeneous and parallel to the easy axis, the sample is an ellipsoid and the material has no surface anisotropy[3]. Then the magnetic field can be expressed as:

$$H_x=-\frac{\partial U}{\partial x},\quad H_y=-\frac{\partial U}{\partial y},\quad H_z=H_a-N_zM_s-\frac{\partial U}{\partial z} \qquad (2.31)$$

Where N_z is the demagnetising factor in the z-direction and U is the magnetostatic potential, which is the solution of differential equations:

$$\nabla^2 U_{in} = 4\pi\nabla\cdot\mathbf{M} = 4\pi M_s\left(\frac{\partial m_x}{\partial x} + \frac{\partial m_y}{\partial y}\right), \qquad \nabla^2 U_{out} = 0 \tag{2.32}$$

With boundary conditions:

$$U_{in} = U_{out}, \qquad \frac{\partial U_{in}}{\partial n} - \frac{\partial U_{out}}{\partial n} = 4\pi\mathbf{M}\cdot\mathbf{n} \tag{2.33}$$

Using these assumptions and neglecting terms, which are non-linear in m_x or m_y, the equation (2.28) can be rewritten for m_x and m_y as:

$$\begin{aligned} \left[C\nabla^2 - 2K_1 - M_s\left(H_a - N_z M_s\right)\right]m_x &= M_s\frac{\partial U_{in}}{\partial x} \\ \left[C\nabla^2 - 2K_1 - M_s\left(H_a - N_z M_s\right)\right]m_y &= M_s\frac{\partial U_{in}}{\partial y} \end{aligned} \tag{2.34}$$

Where C is the exchange constant, K_1 is the anisotropy constant (e.g. cubic or uniaxial) and M_s is the saturation magnetization. These equations should be solved together with the boundary conditions:

$$\frac{\partial m_x}{\partial n} = \frac{\partial m_y}{\partial n} = 0 \tag{2.35}$$

Solutions of Brown's linearized equation correspond to two magnetization reversal modes. One is a coherent rotation mode when all the magnetization rotates coherently and the second is a curling mode with the magnetization forming a flux closure configuration. The limitations of Brown's equation do not allow obtaining a vortex mode but curling is a good approximation for this state. If we find solutions for a particle with an ellipsoidal shape than it will be possible to write analytical solutions for a sphere and infinite cylinder.

Let us first consider a coherent rotation mode. In this case volume magnetic charges are zero, which gives us $\nabla^2 U_{in} = 0$. This leads to a homogeneous field inside an ellipsoid, given by:

$$\frac{\partial U_{in}}{\partial x} = N_x M_s m_x, \qquad \frac{\partial U_{in}}{\partial y} = N_y M_s m_y \tag{2.36}$$

where N_x and N_y are demagnetising factors along x- and y- directions. Substitution of (2.36) into (2.34) gives the expression for the nucleation field in the case of coherent rotation in an ellipsoidal particle[3]:

$$H_n = -\frac{2K_1}{M_s} + (N_z - N_x)M_s \tag{2.37}$$

This solution for nucleation field has the same form as in the Stoner-Wohlfarth model showing that the S-W model is a mode of Brown's equation.

Another mode is curling, which is also a solution of Brown's equation. We will show solutions for an infinite cylinder, a sphere and a prolate ellipsoid. In cylindrical coordinates (ρ, φ, z) we can write for m_x and m_y:

$$m_x = -m_\varphi \sin\varphi = -F(\rho, z)\sin\varphi, \qquad m_y = m_\varphi \cos\varphi = F(\rho, z)\cos\varphi \tag{2.38}$$

where m_φ is the component of **m** in the direction of φ. Then (2.34) becomes:

$$\left[C\left(\frac{\partial^2}{\partial\rho^2} + \frac{1}{\rho}\frac{\partial}{\partial\rho} - \frac{1}{\rho^2} + \frac{\partial^2}{\partial z^2}\right) - 2K_1 - M_s\left(H_a - N_z M_s\right)\right] \cdot F(\rho, z) = 0 \tag{2.39}$$

With boundary condition (2.35), which becomes for $F(\rho, z)$:

$$\frac{\partial F}{\partial n} = 0 \qquad (2.40)$$

Let us first derive solution of (2.39) for an infinite cylinder with radius R. The normal **n** is parallel to the coordinate ρ, which leads to the equation for the Bessel functions. Nucleation field in this case has the form[3]:

$$H_n = -\frac{2K_1}{M_s} - \frac{Cq_1^2}{R^2 M_s} \qquad (2.41)$$

here q_1 is the smallest root of $\frac{dJ_1(q)}{dq} = 0$, C is the exchange constant and $J_1(q)$ is the cylindrical Bessel function of the first order. Comparison with (2.37) and considering that for an infinite cylinder $N_x = N_y = 2\pi$ and $N_z = 0$ gives the value for the critical radius R_c (Ref. 3):

$$R_c = \frac{q_1}{M_s}\sqrt{\frac{C}{2\pi}} \qquad (2.42)$$

Below this radius magnetization changes by coherent rotation and above by curling.

The second case is the magnetization reversal in a sphere. The cylindrical coordinates (ρ, φ, z) are changed to the spherical coordinates (r, θ, φ). The equation (2.34) is rewritten as:

$$\begin{bmatrix} C\left(\frac{\partial^2}{\partial r^2} + \frac{2}{r}\frac{\partial}{\partial r} + \frac{1}{r^2}\frac{\partial^2}{\partial \theta^2} + \frac{\cos\theta}{r^2 \sin\theta}\frac{\partial}{\partial \theta} - \frac{1}{r^2 \sin^2\theta}\right) \\ -2K_1 - M_s\left(H_a - \frac{4\pi}{3}M_s\right) \end{bmatrix} \cdot F(r, \theta) = 0 \qquad (2.43)$$

The analytical expression for the nucleation field is then given by[3]:

$$H_n = -\frac{2K_1}{M_s} - \frac{Cq_2^2}{R^2 M_s} + \frac{4\pi}{3} M_s \tag{2.44}$$

where q_2 is the smallest root of $\frac{dj_1(q)}{dq} = 0$ and $j_1(q)$ is the spherical Bessel function of the first order. Taking into account that $N_x = N_z$ for a sphere, from (2.44) and (2.37) we derive that the critical radius for the spherical particle now has the form:

$$R_c = \frac{q_2}{M_s}\sqrt{\frac{3C}{4\pi}} \tag{2.45}$$

Again we have a coherent rotation for particles with $R < R_c$ and a curling mode for $R > R_c$.

In an ellipsoid the nucleation field and the critical radius are written as[3]:

$$H_n = -\frac{2K_1}{M_s} - \frac{Cq^2}{R^2 M_s} + N_z M_s \qquad R_c = \frac{q}{M_s}\sqrt{\frac{C}{N_x}} \tag{2.46}$$

here R is the half-axis in the direction perpendicular to the easy axis z. The value of q is between q_1 and q_2. It can be also shown that in particles with elliptical or cylindrical shapes in addition to coherent rotation and curling modes there might be a third one called buckling[2,3,5].

These solutions for magnetization changes work only in limited cases of uniform magnetization and well-defined geometries. In practice the real shapes are different from those described in this section, hence the analytical results obtained here have only limited application. Nevertheless they are very useful in understanding reversal processes in nano-particles. Often, the most appropriate way is to use numerical simulations, calculating the dynamics of the magnetic moments in time by Landau Lifshitz Gilbert (LLG) equation[3]:

$$\frac{d\mathbf{M}}{dt} = -\gamma_0 \mathbf{M} \times \mathbf{H}_{eff} - \frac{\gamma_0 \alpha}{M_s} \mathbf{M} \times (\mathbf{M} \times \mathbf{H}_{eff}),$$

$$\mathbf{H}_{eff} = \frac{C}{M_s} \nabla^2 \mathbf{m} + \mathbf{H}_a + \mathbf{H} - \frac{1}{M_s} \frac{\partial w_a}{\partial \mathbf{m}} \qquad (2.47)$$

here γ_0 is the gyromagnetic ratio and α is the damping parameter. The LLG equation describes precession of magnetization with damping, which allows for the magnetization to decay and relax along the field direction. In this project we have used the object-oriented micromagnetic framework (OOMMF) software developed at NIST, USA[6].

2.4 References

---

[1] B. D. Cullity, *Introduction to Magnetic Materials*, Addison-Wesley Publishing Company, 1972

[2] R.C. O'Handley, *Modern Magnetic Materials*, Wiley Interscience, New York, 1999

[3] Aharoni, *Introduction to the Theory of Ferromagnetism*, Oxford University Press, 2000

[4] C. Kittel, Rev. Mod. Phys. **21**, 541 (1949)

[5] A. Aharoni, J. Phys.: Condens. Matter **9,** 10009 (1997)

[6] OOMMF Ver. 1.0; M.J. Donahue and D.G. Porter, http://math.nist.gov/oommf

Chapter 3. Experimental methods

3.1 Preparation of samples

3.1.1 Nano-scale dot and anti-dot arrays from self-assembly method

Fabrication of materials with sub-micron length scales has become an area of a wide interest during last several years due to their possible applications such as photonic crystals[1], high-density magnetic storage media[2], magnetic random access memory[3] and magnetic sensors[4]. Several techniques have been developed for production of nano-scale materials in particular e-beam lithography, x-ray and interference lithography and others[5].

In this project, highly ordered magnetic dot and anti-dot arrays were created by electrochemical deposition through the templates prepared from polystyrene latex spheres. A schematic picture of the fabrication process step by step is presented in Fig. 3.1.

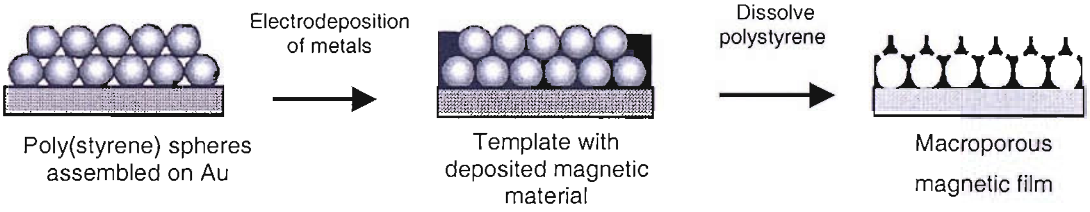

Fig. 3.1 Fabrication of anti-dot arrays – general scheme

This method starts by template preparation using self-assembly of latex spheres. For this purpose a water suspension containing 0.5 wt% of latex spheres is put on a glass substrate, which has buffer layers of Cr (10 nm) and Au (200 nm) deposited by sputtering. During a slow (3-5 days) water evaporation the capillary forces attract spheres to the edge of the water meniscus. Combined with the electrostatic repulsion between the spheres this creates a well-ordered close packed structure, resulting in a hexagonal configuration of spheres in the film plane (Fig. 3.2a). For the formation of 3D templates consisting of two and more layers of spheres evaporation was combined with sedimentation under action of gravitational force. In all cases it's important to maintain the preparation procedure slow enough and adequately controlled. A final 3D template is shown in Fig. 3.2. The spheres are packed in the fcc structure as confirmed by a cross-sectional SEM image (Fig. 3.2b). Generally spheres can be packed in two different ways forming fcc or hcp structures depending on the position of the third layer. Theoretically the fcc structure is the most favorable energetic state but the difference in the free energy is quite small so in practice the fcc structure is not always present. The period of the template can be controlled by the diameter of spheres *d* used in preparation and can be set from 50 nm upward. To achieve smaller length scales other methods have been employed based on molecular templates[6].

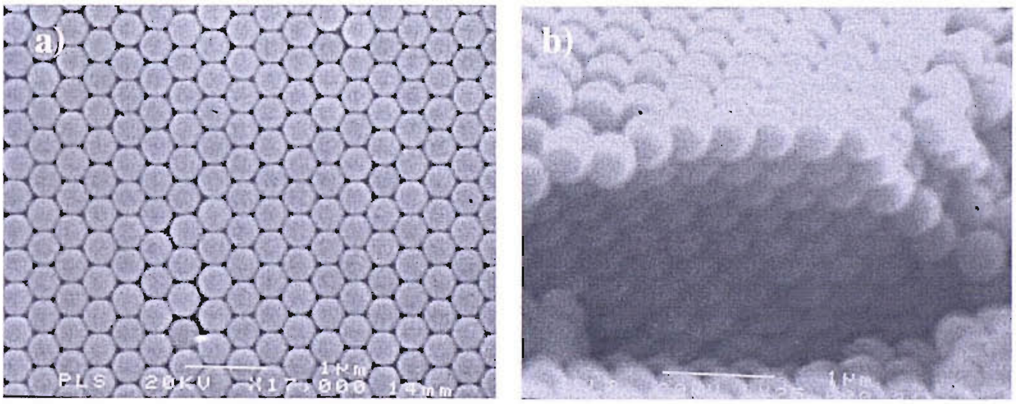

Fig. 3.2 Template prepared from 500 nm latex spheres. (111) plane (a) and cross sectional view (b) reveals the fcc structure.

Using these templates we prepared nano-porous structures from various magnetic materials such as cobalt, nickel and soft-magnetic $Ni_{50}Fe_{50}$ alloy by electro-deposition from the gold underlayer[7,8,9]. After the deposition is completed the latex spheres can be removed by dissolving in toluene. The array period and the film thickness were controlled by changing the diameter of the polystyrene spheres, used to form the template, and the amount of charge passed during the electro-deposition process respectively[7]. The advantage of electro-deposition is that this is a "bottom-up" technique, which allows producing complex structures grown from the substrate electrode into the template. Hence this reduces the probability of structural defects, shrinkages and contamination during filling of the template with a material so that inhomogeneities are only caused by defects in the template. In addition, unlike high vacuum deposition techniques, such as sputtering and evaporation, electro-deposition is an ambient temperature and pressure process. Resulting macro-porous films have a homogeneous composition of magnetic material with excellent filling of the template voids, as evident from the EDSRX studies, which allows to analyze materials by secondary electrons. Studies of nano-structured films by scanning electron microscopy (SEM) showed their hexagonal structure (Fig. 3.3) with the size of ordered domains reaching up to 1 mm and an average concentration of defects in the anti-dot lattice of about 0.1%. In comparison with standard lithographic techniques this template deposition method has a significant advantage. It allows creating structuring in the direction transverse to the film plane, which is also well ordered (Fig. 3.3b).

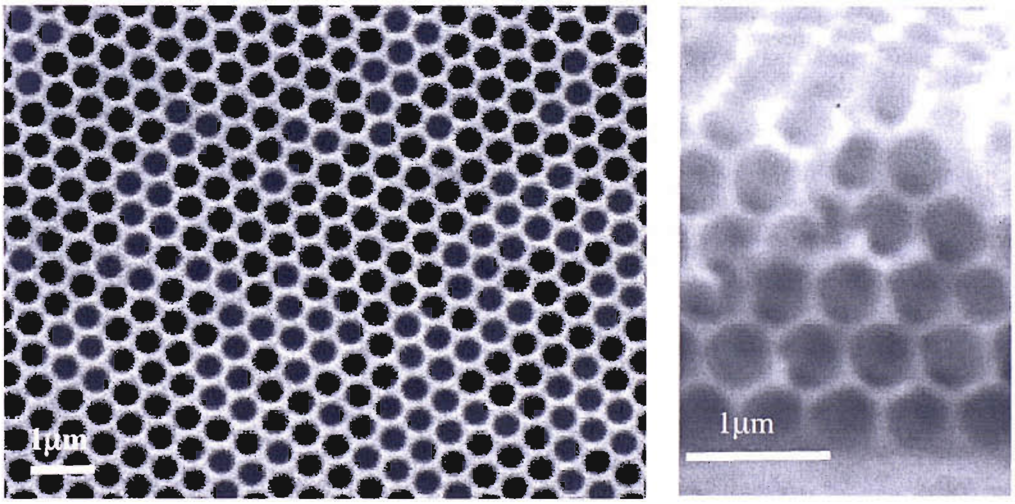

Fig. 3.3 SEM image of $Ni_{50}Fe_{50}$ *film with 500 nm pores.*

Nano-scale dot arrays have been prepared using the double template electro-deposition method (DTE). This fabrication process is schematically shown in Fig 3.4. In this technique an ordered structure of spheres forms a primary template (Fig. 3.4). This primary template is used for the electrodeposition of the conducting polymer polypyrrole resulting in a macro-porous polymer template. After the deposition of polypyrrole the polystyrene spheres are dissolved in toluene leaving a secondary polymer template. The polypyrrole is then converted into an insulator either by over-oxidation or by un-doping at a sufficiently negative potential. This insulating structure is used as the template for electrochemical deposition of magnetic material. At the point where the polystyrene spheres – prior to being removed – touched the substrate, disc-shaped areas with a diameter of ~ $d/4$ of gold surface are exposed. Electrodeposition of magnetic materials starts at these points gradually filling the spherical cavities of the polypyrrole template. More details about the preparation of secondary templates are described in Ref.

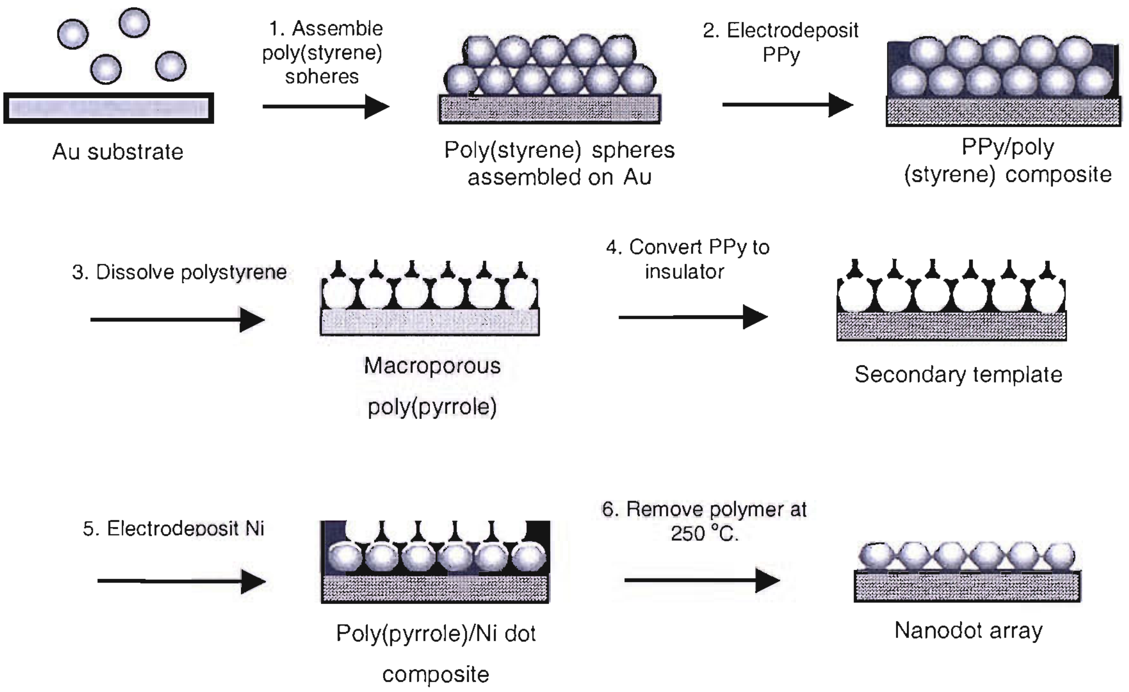

Fig. 3.4 Preparation of nano-dot arrays

10. Using this technique we have prepared ordered arrays of dots with quasi-spherical geometry. The thickness of the dots t can be controlled by varying the amount of charge passed during electrodeposition. For small values of t these structures form ordered arrays of disconnected dots but if the amount of material deposited is increased these dots join up forming ordered magnetic networks. In the former case the dots have a near-spherical or "droplet" shape with a bottom part reproducing the spherical shape of the template cavity and a top part which is dome-shaped due to the growth process. The dot array has a period d which is equal to the diameter of the polystyrene spheres used in template preparation. The morphology of the films and their nano-structure were studied using electron microscopy. Fig. 3.5 shows an SEM image of connected and isolated Ni dot arrays prepared by the double template deposition method. Fig. 3.5b also demonstrates the "droplet" shape of dots.

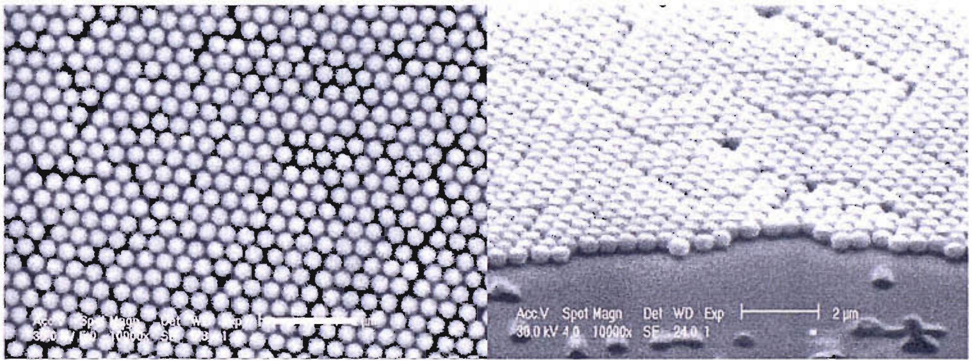

Fig. 3.5 SEM image of isolated (a) and interconnected (b) nano-dots grown using a template assembled from 500 nm spheres

3.1.2 Lithographically prepared arrays

Although an electro-chemical deposition method is low-cost and promising for producing well-ordered nano-structures, lithography remains the most widely used technique in the fabrication of arrays with sub-micron length scales today due to its flexibility in shape of the structures and essentially ideal order. This method includes resist coating, exposure and development combined with etching or lift-off techniques. Generally a lithographic process can be described briefly as follows. At the beginning a substrate or an unpatterned film is covered with a resist layer. Then the resist is exposed to the radiation source through a mask followed by baking. Depending on resist properties one can obtain a positive image of the mask (positive resist) or a negative image of the mask (negative resist). After development nanostructures can be fabricated in two general ways such as etching or lift-off.

Arrays of magnetic nano-structures studied in this work have been prepared by electron-beam lithography combined with a lift-off technique. In this method the desired pattern is produced by exposing a Si substrate covered with an electron sensitive resist layer (PMMA) to the electron beam. A schematic view of this process is shown in Fig. 3.6. The SEM is connected to the external computer, which allows writing a previously programmed pattern (Fig. 3.6a). After exposure, resist regions, which were exposed to the electron beam are removed by a developing process (Fig. 3.6b). Subsequently, magnetic materials are deposited through this PMMA template (Fig. 3.6c). At the final stage lift-off was carried out: the resist together with the film deposited on the top was removed by dissolving in acetone. Hence the magnetic material remains only on the substrate areas that had not been covered by PMMA (Fig. 3.6d). Resulting nano-structures have a high quality and excellent order.

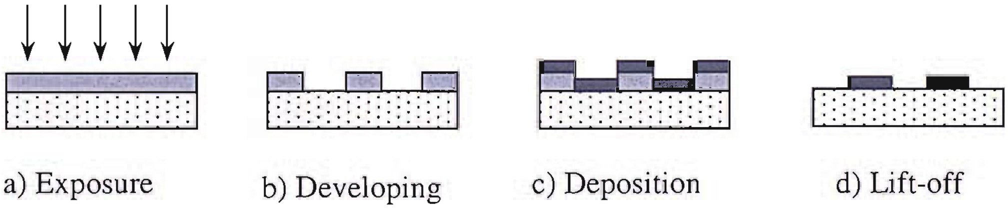
a) Exposure b) Developing c) Deposition d) Lift-off

Fig. 3.6 E-beam lithography combined with lift-off (schematic representation)

We have studied many different shapes, in particular arrays of dots, anti-dots, round and square rings prepared from NiFe and Co. Some examples of fabricated nano-structures are shown in Fig. 3.7.

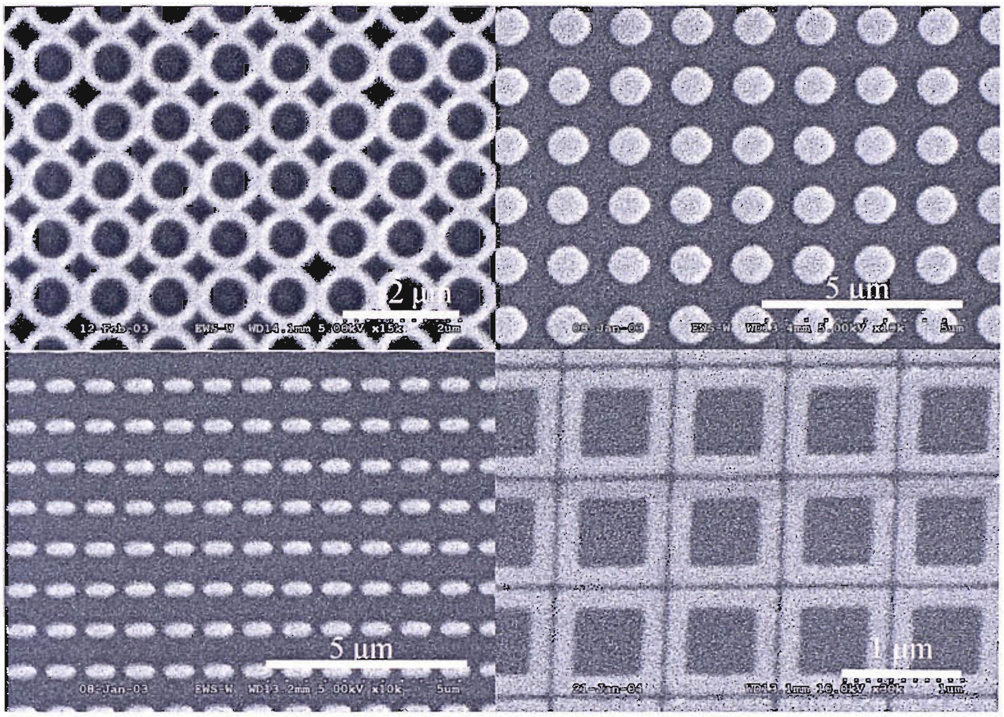

Fig. 3.7 SEM images of nano-structures prepared by e-beam lithography

3.2 Magnetometry

3.2.1 MOKE Magnetometer.

The first observation of magneto-optical effects dated to 1845 when M. Faraday found that glass placed in a magnetic field becomes optically active. The polarization of a beam of light passed through the glass was rotated. Results for changes of polarization in the beam reflected from a metal surface were not quite conclusive due to the surface roughness. Later, in 1877 J. Kerr discovered the magneto-optical Kerr effect (MOKE).

He found that the polarization of light undergoes rotation after reflection from magnetized matter.

Basic magneto-optical phenomena can be classified according to the relative orientation of propagation wave vector **k** and the magnetic field **H**. There are two basic configurations: Faraday geometry when light travels along the field direction ($\mathbf{k}||\mathbf{H}$) and Voigt geometry when light travels perpendicular to the field direction ($\mathbf{k} \perp \mathbf{H}$).

Generally the optical behaviour consists of magnetic circular birefringence and dichroism (MCB, MCD) if we deal with Faraday geometry and magnetic linear birefringence and dichroism (MLB, MLD) in case of Voigt geometry.

Microscopically these effects are explained using a theory of the Zeeman effect[11]. We can qualitatively understand these phenomena using the idea of interaction between the propagating light and orbital magnetic moments of the electrons inside the medium. Let us consider linearly polarized light as a sum of left and right circularly polarized modes. When this light propagates in a magnetized medium there are two basic effects that take place. First, the two circularly polarized modes have different refractive indices (n+ and n-), which leads to different phase shift due to their different propagating velocities. As a result the plane of polarization rotates when light travels through the medium (MCB). Secondly, if the medium exhibits absorption then absorption rates for two modes will be different which will affect the ellipticity (MCD). In the case of Voigt geometry light propagating normal to the applied field can be considered as composed of vertical and horizontal linearly polarized light, which will have different refractive indices ($n\perp$, $n||$) the case of MLB and different absorption rates (MLD).

For the magneto-optical Kerr effect three configurations can be distinguished. In the polar configuration the magnetization is parallel to the surface normal and lies in the plane of incidence. In this effect linearly polarized light becomes elliptically polarized upon reflection from the sample surface (MCB and MCD) Fig. 3.8(a). In the longitudinal Kerr effect magnetization is parallel to the surface but still in the optical plane Fig. 3.8(b). In this case an ellipticity occurs and the plane of polarization is also rotated when linearly polarized light is reflected from the sample surface. In longitudinal geometry the magnetization has a component parallel to the propagation direction and therefore MCB and MCD are also observed as in above case. In transverse configuration the magnetization is parallel to the surface and perpendicular to the optical plane Fig. 3.8(c). This effect manifests itself in intensity variation only, and there is no change in polarization state of the reflected light.

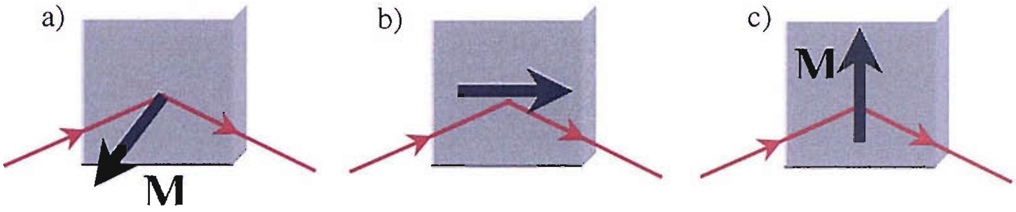

Fig. 3.8 Magneto-optical Kerr effect – three possible configurations a) polar geometry, b) longitudinal geometry, c) transverse geometry

The analysis of these effects is based on Fresnel reflection coefficients derived from a phenomenological model of the Kerr effect[12,13,14]. In this model the response of the medium to the applied field is described by the antisymmetric part of the dielectric tensor with off diagonal elements that in the general case has the form:

$$\varepsilon = \begin{pmatrix} \varepsilon_0 & ig_z & -ig_y \\ -ig_z & \varepsilon_0 & ig_x \\ ig_y & -ig_x & \varepsilon_0 \end{pmatrix} \tag{3.1}$$

Where ε_0 is a scalar dielectric constant in the absence of magnetization $\mathbf{g} = \varepsilon_0 Q\hat{\mathbf{g}}$ is a gyrotopic vector, which is parallel to the magnetization direction, and Q is magneto-optical parameter dependent on the magnetization. It's well known that there are two circularly polarized modes propagating in a magnetized medium. The off diagonal elements in the dielectric tensor alter refractive indices for the left and right circularly polarized light which obey the following equation:

$$n^{\pm} = n(1 \pm \frac{1}{2}\mathbf{Q}\cdot\mathbf{k}) \tag{3.2}$$

In the macroscopic description of the Kerr effect the components of the reflected light can be expressed from the components of the incident light via the reflectivity tensor:

$$\begin{pmatrix} E_s^{(r)} \\ E_p^{(r)} \end{pmatrix} = \begin{pmatrix} r_{ss} & r_{ps} \\ r_{sp} & r_{pp} \end{pmatrix} \begin{pmatrix} E_s^{(i)} \\ E_p^{(i)} \end{pmatrix} \tag{3.3}$$

After solving a reflection-transmission problem mathematically, the Fresnel coefficients for the longitudinal Kerr effect can be expressed as follows:

$$\begin{aligned} r_{pp}^{l} &= (n\beta - \beta')/(n\beta + \beta') \\ r_{ss}^{l} &= (\beta - n\beta')/(\beta + n\beta') \\ r_{ps}^{l} &= -r_{sp}^{l} = \frac{in^2 Q\beta \sin\theta}{n^2\beta'(n\beta + \beta')(\beta + n\beta')} \end{aligned} \tag{3.4}$$

Where $\beta = \cos\theta$ and $\beta' = \sqrt{1 - \frac{\sin^2\theta}{n^2}}$

In these formulas r_{ps} for example, is the reflection coefficient relating the incident p-wave and reflected s-wave. The notation s and p refer for the light polarized perpendicular and parallel to the optical plane respectively. The angel of incidence θ is measured from the surface normal and n is the refractive index of the material. The coefficients for the longitudinal Kerr effect describe a rotation of the incident polarization by the presence of magneto-optical parameter in the expression for r_{ps}. This means that in the presence of the magnetic field incident p-polarized light will gain an additional s-component upon reflection, which will change the polarization to elliptical with the major axis rotated Fig. 3.9. The same consideration can be also referred to the incident s-polarized wave.

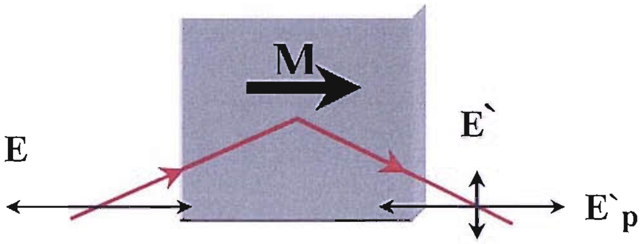

Fig. 3.9 Appearance of additional s-component for p-polarized incident light in longitudinal Kerr effect.

For the transverse Kerr effect the Fresnel coefficients derived from this model have the form:

$$r^t_{pp} = \left(\frac{n\beta - \beta'}{n\beta + \beta'}\right)\left(1 + \frac{in^2 Q \sin 2\theta}{n^2(n^2\cos^2\theta - 1) + \sin^2\theta}\right)$$

$$r^t_{ss} = (\beta - n\beta')/(\beta + n\beta') \tag{3.5}$$

$$r^t_{ps} = r^t_{sp} = 0$$

In contrast with the longitudinal effect the reflected light does not have changes in the polarization state because the off diagonal elements in the reflectivity tensor are zero. The only effect connected to the applied magnetic field in this case is an intensity variation in the reflected p-polarized light.

The fact that changes in the state of polarization are proportional to the magnetization inside the material makes MOKE potentially applicable for magnetization measurements. Especially in the study of surface magnetism because it is very sensitive to the magnetization within a depth of 10-20 nm from the surface[15]. Using the MOKE technique we can quickly obtain hysteresis loops in thin films and study anisotropy effects. In addition to the magnetization loops the MOKE imaging system can provide magnetic information by means of domain images. A further advantage of this method is that we can focus a laser beam to small areas - down to 5 μm in diameter. For example this is helpful in studying arrays of magnetic nanoparticles. All these features make the MOKE technique a central method in studying nano-magnetism. Finally it can be mentioned that an experimental setup based on the magneto optical phenomenon is relatively simple to build and to operate.

The MOKE setup used in this project is schematically given in Fig. 3.10. It allows the investigation of magnetic materials and obtains information equivalent to magnetization loops. Many different samples, including thin magnetic films, arrays of magnetic nanoparticles or antidot networks can be studied using this effect. The magnetic field is produced by an electromagnet and can reach 4 kOe.

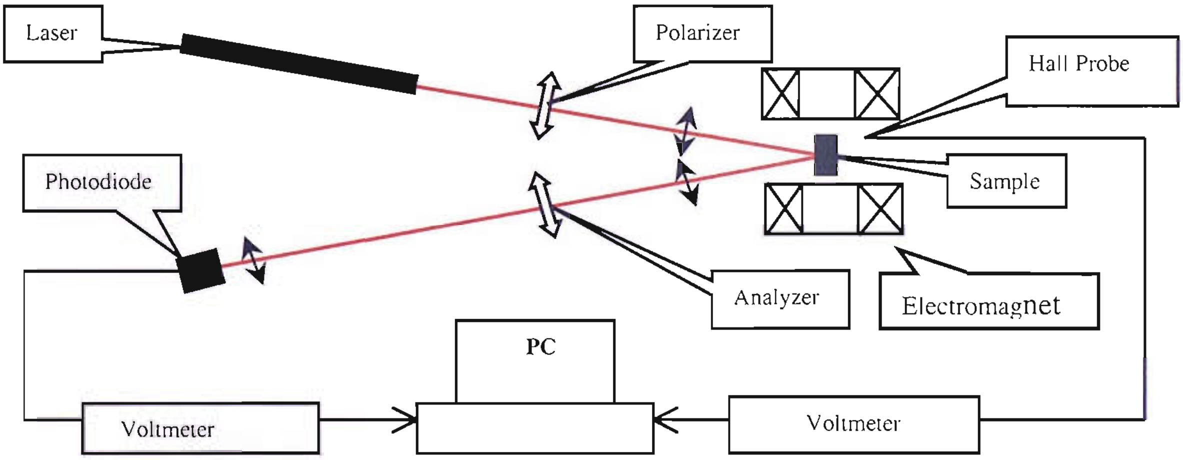

Fig. 3.10 MOKE magnetometer

For different experiments the direction of magnetic field can be set either parallel (longitudinal field LF) or perpendicular (transverse field TF) to the optical plane to work with different Kerr configurations. The schematic picture in Fig. 3.10 shows a common longitudinal Kerr geometry with longitudinal field. Along with this configuration the longitudinal Kerr effect with transverse field has been used to observe the component of the magnetization perpendicular to the applied field and in the study of in-plane anisotropy. A 15 mW He-Ne laser with wavelength of 633 nm has been used as a source of linearly polarized light. The *s*-polarized or *p*-polarized laser beam passed through a polarizer is focused into a small spot on the sample surface using a plane-convex lens with a focal length 160 mm. The diameter of the spot depends on the focal length of the focusing lens and the diameter of the laser beam as given in following expression:

$$D = \frac{4\pi}{\lambda}\frac{f}{d} \qquad (3.6)$$

Where λ is a wavelength of the light, d – diameter of the beam and f is a focal length. As follows from this formula, in order to decrease the size of the focused spot it is better to use a lens with small focal length but in this case the Faraday rotation in the lens placed close to the magnetic field should be taken into account. On the other hand the situation can be improved by using a broader laser beam. For this purpose a set of plane concave and double convex lenses with focal length 80 and 40 mm respectively are placed before polarizer to expand the laser beam up to 4 mm in diameter. The calculated diameter of the focused spot obtained using (3.6) is about 20 microns. In practice an actual size of 50 microns in diameter was achieved. This difference is due to aberration effects and instrumentation used in this magnetometer.

The magnetic samples are glued by GE-varnish to a holder attached to the *x*-*y* translation stage, which allows focusing the laser beam on different areas of the films. The step size of the translation is 20 microns and controlled by fine micrometric screws. In addition to *x*-*y* movement the sample can be rotated around the *z*-axis with angular resolution of 3 degrees, which gives an opportunity to study in-plane anisotropy properties in thin films and particle arrays.

After reflection from the sample surface the beam passes through the focusing lens and its polarization state is analyzed using a second crossed polarizer. Changes in the intensity of the beam due to the Kerr rotation are monitored by a photodiode detector with a built-in amplifier. The power supply for the magnet combined with a generator allows sweeping the magnetic field with different rates. The most appropriate rate found in experiments was between 1 and 5 mHz for this set-up. The applied magnetic field is measured using a Hall Probe placed between the poles of the electromagnet. The experiment was controlled by the PC using data acquisition software (HPVEE) developed by Hewlett Packard. This makes it possible to display magnetization loops in real time.

3.2.2 Vibrating Sample Magnetometer

Vibrating sample magnetometers (VSM) are powerful instruments for the characterization of magnetic materials. In this type of magnetometer the sample is vibrated near a set of pick-up coils and the voltage induced in these coils is proportional to the magnetization of the sample. The moving sample, when magnetized, produces a time varying magnetic flux, which induces a corresponding voltage in the pick-up coils. Generally the induced electromotive force is given by:

$$E = -\frac{d\Phi}{dt} \tag{3.7}$$

Where Φ is the magnetic flux induced by the sample. To minimize the effects of field instability and mechanical vibrations of the magnet usually two pick-up coils are used connected in series. The upper is wound in one direction and the lower in the opposite direction so that no voltage is induced by changes in the applied field; only changes in the magnetic flux induced by the magnetized sample give a signal.

Magnetization measurements were performed using a commercial Oxford Instruments 3001 VSM, which allows maximum field up to 12 T in temperature range 1.7 – 300 K. A schematic picture of this rig is shown on Fig. 3.11

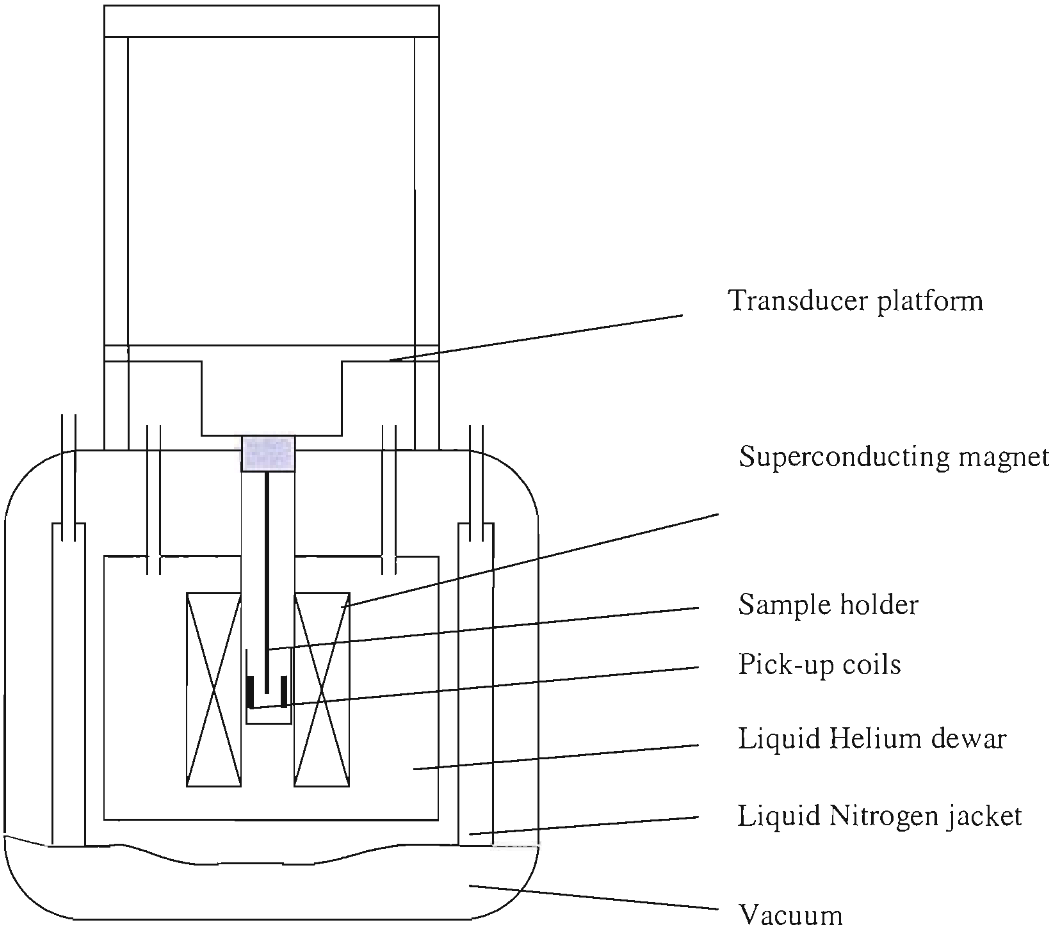

Fig. 3.11 Schematic diagram of the Oxford Instrument 12T VSM 3001

As it is shown in Fig. 11 a superconducting magnet is placed in liquid helium at a temperature 4.2 K. The magnet consists of two concentric solenoids and compensating coils, which are used to eliminate the effect of inhomogeneity in the produced magnetic field. Solenoids are wound using multifilamentary superconducting NbTi wire and surrounded by a copper matrix. The copper due to its high thermal and electrical conductivity helps to prevent thermal instabilities. The Oxford Instruments PS 120 power supply produces a current of 120 A in the voltage range ±10 V and allows to sweep the magnetic field with rate from 0.1 to 20 mT/sec.

The cryostat itself has a metal construction and consists of two vessels filled with liquid helium and nitrogen respectively. The outer and inner surfaces of both vessels are covered with multilayer superinsulator. To improve thermal stability and prevent quick evaporation of helium these two vessels are contained in 10^{-5}-10^{-6} mbar vacuum.

The VSM has a VTI (Variable Temperature Insert) unit, which is designed to control the thermal condition in the sample area. The sample is placed inside this insert and its temperature can be controlled between 2.1 and 300 K. Variation in temperature is performed by using a helium gas flow through the needle valve as a coolant with the help of an electrical heater and a thermocouple fitted close to the sample. The voltage from the thermometer is passed to the ITC4 temperature controller, which controls the power to the heater.

The sample is fixed to the sample holder by PTFE tape. The holder is screwed to a fiber rod connected to a vibrating transducer performing oscillation along the z-axis. The frequency of vibration is 66.66 Hz with amplitude 1.5 mm. For precise positioning of the sample between pick-up coils the vibrating unit can move in the z-direction with a resolution of 5 microns.

The operation of the VSM is governed by a PC using a commercial software package AEROSONIC via an RS232 interface. The magnetization measurements can be carried out as a function of the applied field, temperature, sweep or rate with resolution 10^{-5} emu.

3.2.3 SQUID Magnetometer

In studying thin magnetic films and arrays of nano-particles, magnetization measurements can become extremely difficult due to the small amount of magnetized material. This means that the sensitivity of a VSM or a MOKE magnetometer in some cases is not enough to detect such a small signal and devices with higher resolution should be used. The SQUID (superconducting quantum interference device) magnetometer, which is sensitive to the magnetization signal down to 10^{-8} emu which is 10^{3} higher, than the VSM resolution (10^{-5} emu). In our experimental work we used the Cryogenic Limited 6T rf SQUID susceptometer (Fig. 3.11). Using the SQUID magnetometer the magnetization can be measured as a function of applied field and temperature (1.5 – 300 K).

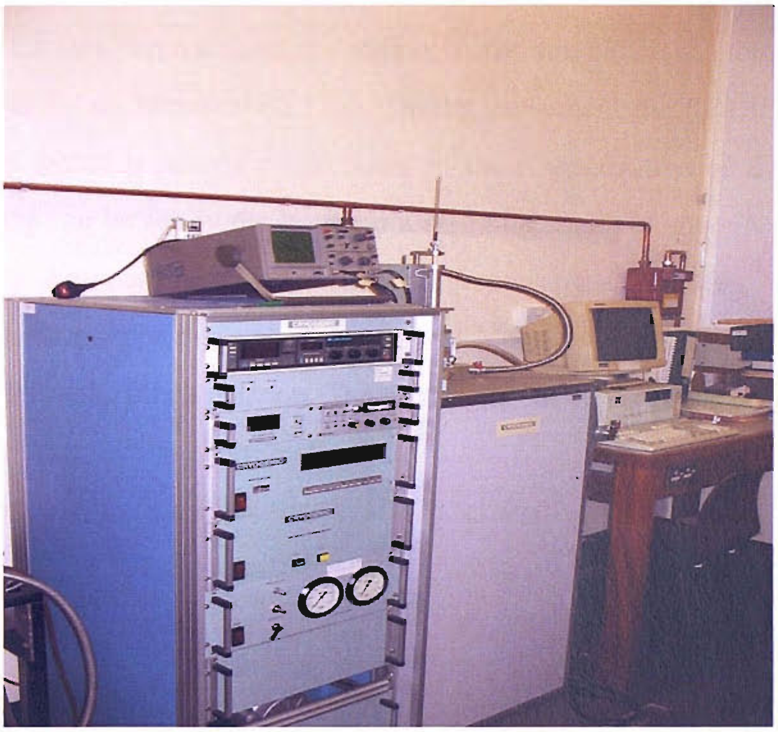

Fig. 3.11 A Cryogenic Limited 6T SQUID susceptometer

A very stable magnetic field is produced by a superconducting magnet placed in a liquid helium dewar. During each measurement the superconducting magnet is put in a persistent mode leading to a very stable applied field. In addition to stability of the field this magnet can perform a zero field oscillations in order to reduce a remanent field. For better thermal insulation there is a liquid nitrogen jacket and both vessels are vacuum isolated.

The VTI unit has a helium gas flow cooling system controlled by a needle valve combined with two temperature sensors and a heater. A temperature controller LakeShore DRC-91CA takes the information from sensors and varies heater power.

A set of three superconducting pick-up coils is used, where two coils are wound in one direction and the third one is wound in opposite direction and has twice the number of turns. These pick-up coils are coupled to the input coil of the SQUID sensor. The SQUID measures a relative flux change when a sample is moved slowly through the pick-up coils. For this purpose there is a stepper motor mounted at the top of the rig. The scan length can be set between 1-12 cm. During movement the SQUID generates an output voltage, which is strictly proportional to the magnetization of the sample. The number of scans can be set by the user and a resulting response curve is averaged over this number by the control software with background signal removed. The sample is placed in a cylindrical tube made from quartz, which produces negligible magnetic signal and two wooden sticks fix its position. The tube is attached by PTFE tape to the end of a brass rod. This setup is fully controlled by PC.

3.2.4 Transport measurements

Transport measurements play an important role in studying resistive properties of materials. In magnetic samples the resistivity is affected by the magnetization. Using a 16T transport rig, the magneto-resistive properties of ferromagnetic nano-scale structures have been investigated in magnetic fields up to 10T and temperatures down to 10 K.

The main part of the rig is an Oxford Instruments 16T cryostat (Fig. 3.12), which has two vacuum isolated vessels filled with liquid helium and nitrogen. Its superconducting magnet provides a magnetic field up to 14 T at 4.2 K and 16 T at 2.2 K.

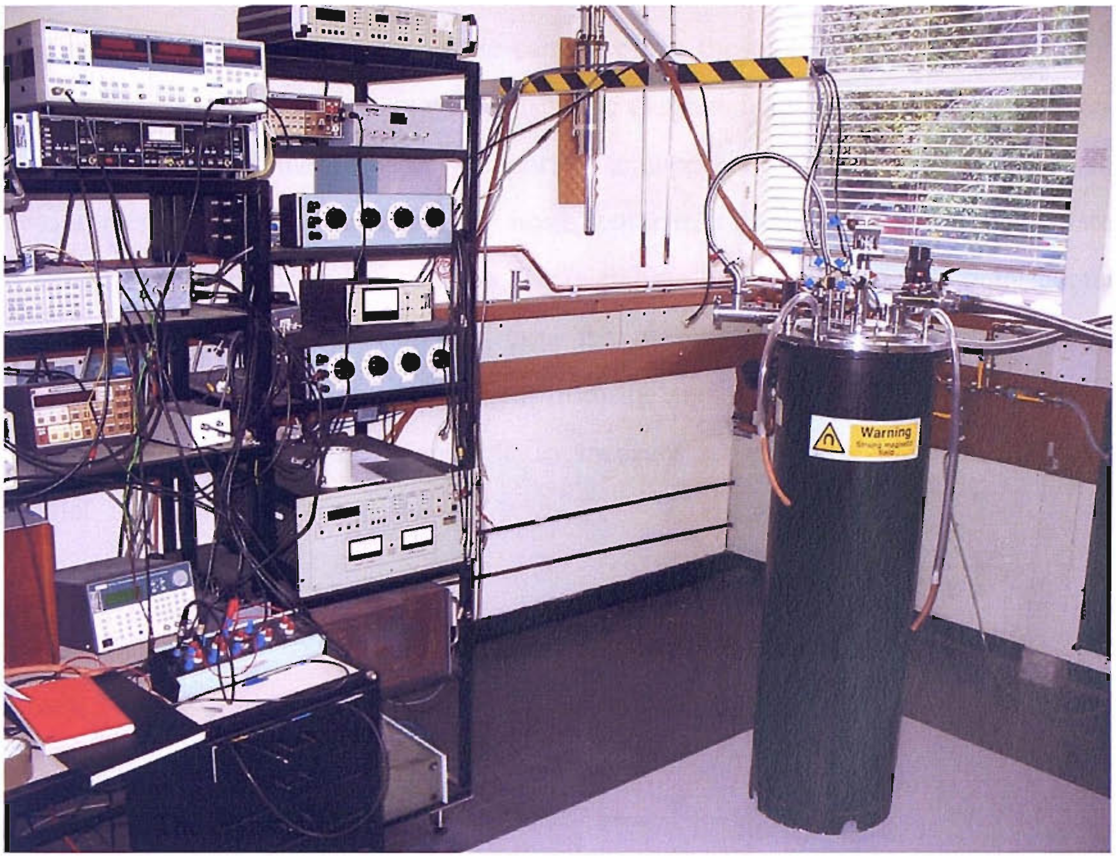

Fig. 3.12 Oxford Instruments 16T cryostat

The cryostat has a standard VTI unit with a helium gas flow cooling system. The amount of He gas is controlled by a needle valve. The system has a dual stage temperature control. The temperature inside the VTI is controlled by an ITC4 using a sensor/heater pair. The sample temperature is measured by a sensor/heater pair fixed to the sample holder (brass platform). The temperature sensor is positioned as close as possible to the sample and has a very good thermal contact with both platform and sample. The sample platform is enclosed in a casing to prevent its contact with coolant gas and placed inside the VTI. The heater output was controlled by a dual channel LakeShore 340 temperature controller, which stabilizes the temperature in the sample area with accuracy 0.5 mK in case of low temperatures and 1-2 mK in case of room temperatures. In order to perform magnetic or transport measurements with the magnetic field applied at different angles to the sample plane the platform can be rotated with angular resolution of 0.001 degrees. A schematic diagram is given in Fig. 3.13. In a low-level voltage measurement it is very important to suppress the noise and drifts from the measurement circuit. The most apparent noise source in transport measurements is related to the voltage drop across the contacts. To overcome this problem a four-point contact configuration has been used. In this case the measured voltage corresponds to the resistance of the sample only. AC current from the signal generator was applied in two different directions making it possible to measure magneto-resistance in directions parallel

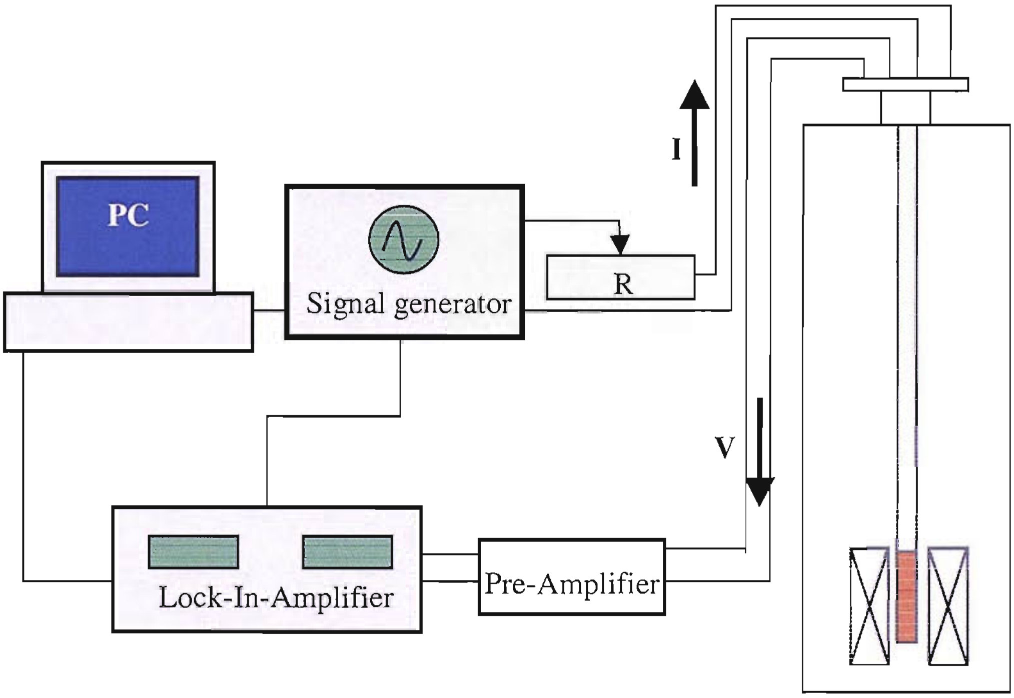

Fig. 3.13 A scheme of experimental arrangement for transport measurements

and perpendicular to the applied field. The voltage from the second pair of contacts was connected to a Stanford Research Systems SR830 Lock-In-Amplifier. Lock-in detection is the most effective method of separating a signal from the noise background and can help to eliminate a low frequency thermal drift. In addition, this rig allows performing transport measurements with DC current using an ac-modulated magnetic field. In this case a modulationg coil inside the superconducting magnet provides a modulation of the field. All equipment was controlled by the PC through IEEE interface using HPVEE software.

3.3 References

---

[1] S. Coyle et al, Phys. Rev. Lett. **87**, 176801-1 (2001)

[2] A. Moser et al. J. Phys. D: Appl. Phys. **35** R157 (2002)

[3] J. G. Zhu, and Y. Zheng, and G.A. Prinz, J. Appl. Phys. **87**, 6668 (2000)

[4] M.M. Miller et al, Appl. Phys. Lett. **81**, 2211 (2002)

[5] J. I. Martin et al, J. Magn. Magn. Mat. **256**, 449-501 (2003).

[6] P.N. Bartlett, P.N. Birkin, M.A. Ghanem, P.A.J. de Groot, M. Sawicki, J. Electrochem. Soc. **148**, C119 (2001).

[7] M. A. Ghanem, P. N. Bartlett, I. S. el-Hallag, P. A.J. de Groot, A.A. Zhukov in preparation.

[8] P.N. Bartlett, P.R. Birkin, M.A. Ghanem, Chem. Comm., 1671 (2000).

[9] P.N. Bartlett, J.J. Baumberg, P.R. Birkin, M.A. Ghanem, M.C. Netti, Chem. Mater **14**, 2199 (2000).

[10] M. A. Ghanem et al., J. Mat. Chem. **11**, 849 (2001).

[11] A.K. Zvezdin, V.A. Kotov "Modern magnetooptics and magnetooptical materials", IOP Publishing, 1997

[12] J. Zak, E.R. Moog, C. Liu, S.D. Bader, J. Appl. Phys. **68** (8) 4203 (1990).

[13] J. Zak, E.R. Moog, C. Liu, S.D. Bader, J. Magn. Magn. Mat. **89**, 107-123, (1990)

[14] Z.J. Yang and M.R. Scheifein, J. Appl. Phys. **74** (11) 6810-6824 (1993)

[15] J.A.C. Bland, M.J. Padgett, R.J. Butcher, N. Bett, J. Phys. E. Sci. Inst. **22** 308 (1989).

Chapter 4. Magnetic properties of nano-structures prepared using self-assembly method

4.1 Introduction

This chapter presents studies of magnetic properties of nano-scale anti-dot and dot arrays with 3D architectures, fabricated using self-assembly methods. In particular, investigation on anti-dot arrays were focused on coercive field, B_c, which characterizes how easily the direction of the magnetization can be switched in a magnetic material. Control over the value of B_c is a powerful tool when developing magnetic devices. It was found that the patterning perpendicular to the plane of 3D nanostructured films governs the magnetic behaviour. The coercive field was found to demonstrate an oscillatory dependence on the film thickness and changes its value for different hole diameters, reaching a maximum for the case when the diameter of the hole is close to the domain wall width. Magnetic properties of the nano-dot arrays were found to depend strongly on dot size and connectivity leading to a rich variety of reversible, vortex and square-like magnetization loops. Results have been interpreted using 2D and 3D micromagnetic simulations and by a simple domain wall model.

4.2 Coercivity of 3D anti-dot arrays

4.2.1 Coercive field and pore size

The effect of the anti-dot array pattern on the magnetic properties of nano-structured films have been investigated at room temperature with fields applied in the film plane using a vibrating sample magnetometer (VSM). The nanostructuring was found to affect significantly the shape of magnetization loops as is shown in Fig. 4.1.

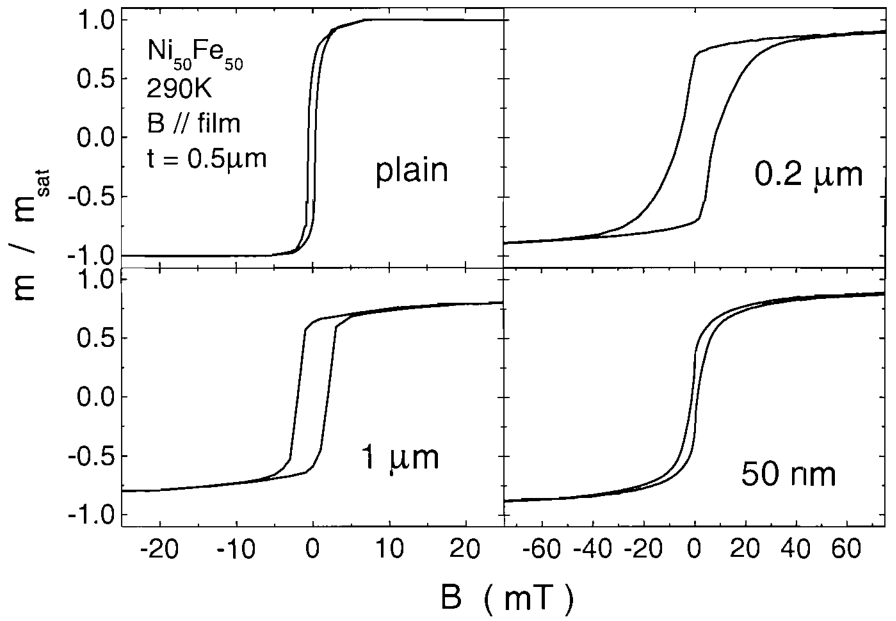

Fig. 4.1 Magnetization loops for plain and nanostructured films prepared from $Ni_{50}Fe_{50}$ *alloy. These curves were measured using VSM with the magnetic field in the plane of films.*

In this picture the magnetization loop for a plain film of $Ni_{50}Fe_{50}$ is compared with three curves for nano-structured films with different hole diameters namely 200 nm, 1000 nm and 50 nm. These loops demonstrate that together with the shape of hysteresis the nano-structuring drastically changes the coercive field B_c. A nanostructured film of $Ni_{50}Fe_{50}$ prepared using 200 nm spheres gives $B_c = 10.2$ mT in comparison with 0.6 mT for a similarly deposited plain $Ni_{50}Fe_{50}$ film. Further investigation has revealed that the coercivity increases by more than an order of magnitude for decreasing pore size (1μm ≥ $d \geq 50$ nm). After reaching a maximum, B_c decreases for further decrease of anti-dot diameter (Fig. 4.2). These data suggest that a maximum in coercivity appears when the value of the sphere radius satisfies the condition $R_{\max} \approx \delta$ where δ is the domain wall width for this material. Indeed, the domain wall width is $\delta = 14$ nm for Co[1], and estimated value of $\delta = \pi\sqrt{A/K_1} \approx 0.2\mu m$ for $Ni_{50}Fe_{50}$. This can be obtained from the anisotropy constant $K_1 = 1.3$ kJ/m^3 of this material[2] and the exchange stiffness $A = 5.8$ pJ/m, taken to be average between the values for Fe and Ni. These values are in reasonable agreement with the position of the maximum in coercivity for the Co and $Ni_{50}Fe_{50}$ data.

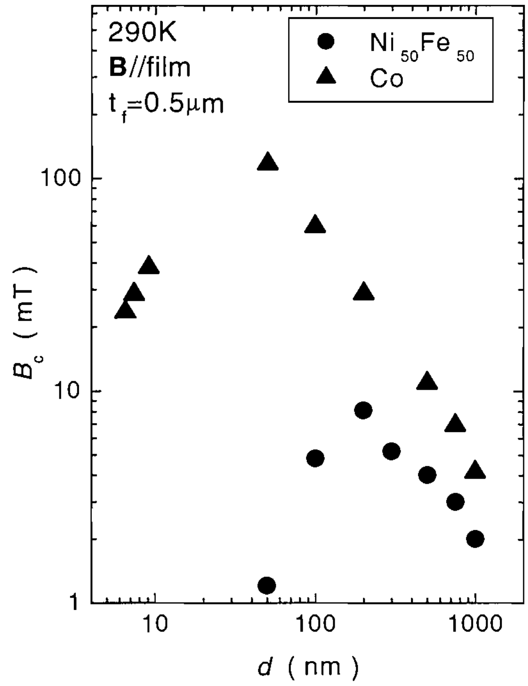

Fig. 4.2. The measured coercivities as a function of the pore size for two different magnetic materials. The samples with d below 10 nm were prepared using soft templates.

Magnetization measurements were performed at room temperature with the field applied in the plane of the films (Results for samples with d less than 20 nm were obtained by A. Zhukov)

These $B_c(d)$ data resembles that of particulate magnetic materials[1]. However, in contrast to our samples, particulate materials correspond to dot, rather than anti-dot, structures. In nano-dots, a mono-domain magnetic state is realized for small grain sizes resulting in a magnetic behaviour determined by coherent rotation of the magnetic moments. In this case the peak in B_c is usually related to the transition from purely coherent rotation to curling behavior of the magnetic moments realized by different non-collinear configurations of magnetic moments[3]. For anti-dot structures the situation is different and a mono-domain state is not favored. In this case the magnetic reversal process can be modeled by the interaction of domain walls with the voids[3]. This interaction strength is sensitive to the relation between magnetic length scales and pore sizes. As discussed above, our results for different magnetic materials suggest that the peak position appears for $R_{\max} \approx \delta$, which indicates the importance of domain wall pinning for such anti-dot structures.

4.2.2 Studies of thin anti-dot films using vector-magnetometry

Two main types of domain walls exist in magnetic films[4]. For Néel walls the magnetic moments rotate in the plane of the film. For Bloch walls the rotation of magnetic moments is perpendicular to the film plane. The transition from Bloch to Néel walls in thin magnetic films is governed by magnetostatic energy. To find out which type of domain walls is realized in our films we employed a vector VSM. Using vector magnetometry allows measuring both components of the magnetic moment (perpendicular and parallel to the film plane) and helps to clarify the type of the wall. In this method the magnetic field is aligned parallel to the film plane with 0.1% accuracy and magnetization loops are measured for two components of $\mathbf{M}$. Fig. 4.3 shows the clear existence of a transverse magnetic moment with maximum value of about 1% of the saturation value M_s. The value of $\mathbf{M}_\perp$ demonstrates sharp peaks near the coercive field. These results indicate that the rotation of magnetic moments in our films takes place in the direction transverse to the film plane. To investigate further the importance of the out-of-plane component of the magnetic moment we have studied transverse magnetization loops for different directions of the applied field. Fig. 4.3c demonstrates the dependence of the measured coercivity B_c (position of the peak on the transverse loop) on the field direction.

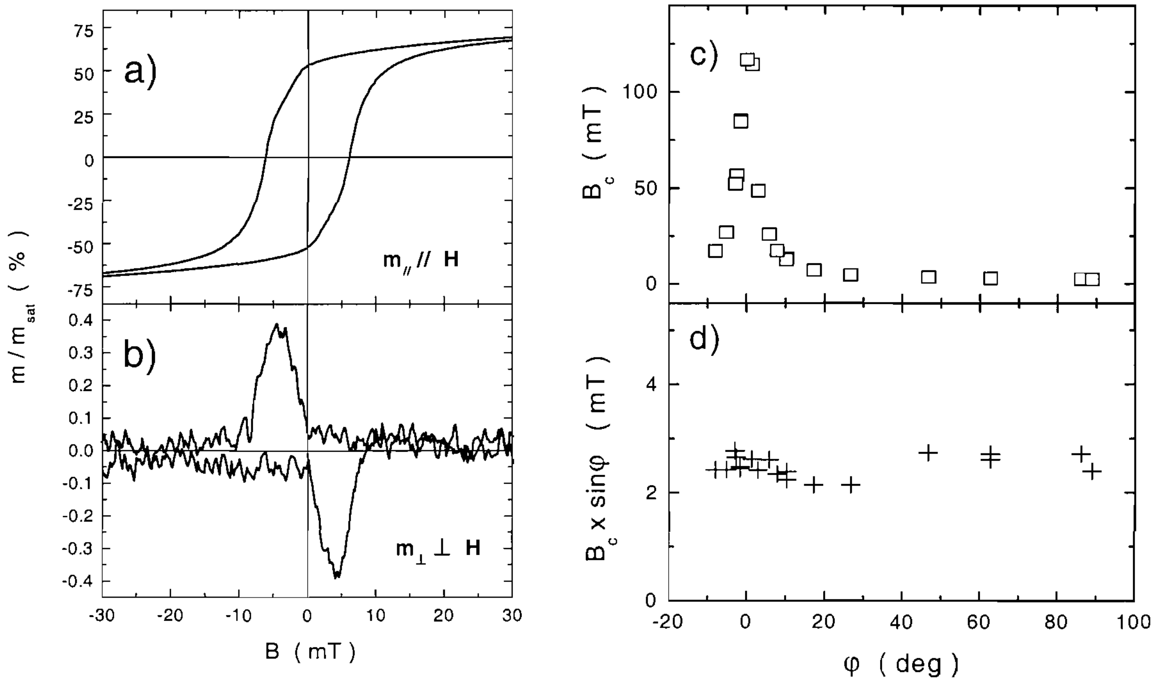

Fig.4. 3 (a) and (b) - two components of the magnetic moment for a nanostructured $Ni_{50}Fe_{50}$ film with a thickness of 700 nm prepared from latex spheres with d = 500 nm. Applied coercive field and its projection in the plane of the film versus the angle between the normal to the film and magnetic field, (c) and (d).

These data show that the coercivity is increasing when the field approaches the normal direction to the film plain. This effect is caused by shape anisotropy, which localizes magnetic moments in the film plane. Indeed the in-plane component of the field $\mathbf{B}\sin\varphi$ gives the constant value of coercivity Fig. 4.3d. Hence the transverse component of the field is relatively unimportant in accordance with in-plane localization of magnetic moments.

4.2.3 Oscillatory behaviour of the coercive field

Measurements of the dependence of B_c on the thickness of the magnetic film revealed a remarkable behaviour. Although these films have homogeneous composition of magnetic material, as evident from the EDSRX studies, we have found that for all materials investigated the coercive force changes periodically with film thickness. This is a clear manifestation of the structuring in the direction perpendicular to the film plane and the 3D architecture of these structures. Fig. 4.4 demonstrates that B_c shows clear oscillations and reaches a maximum when the top surface of the film is near the centre of a layer of close packed spherical voids. For complete spherical voids the coercive field approaches a minimum. These observations suggest that the points where the spheres are touching play an important role in domain wall pinning and hence the coercivity.

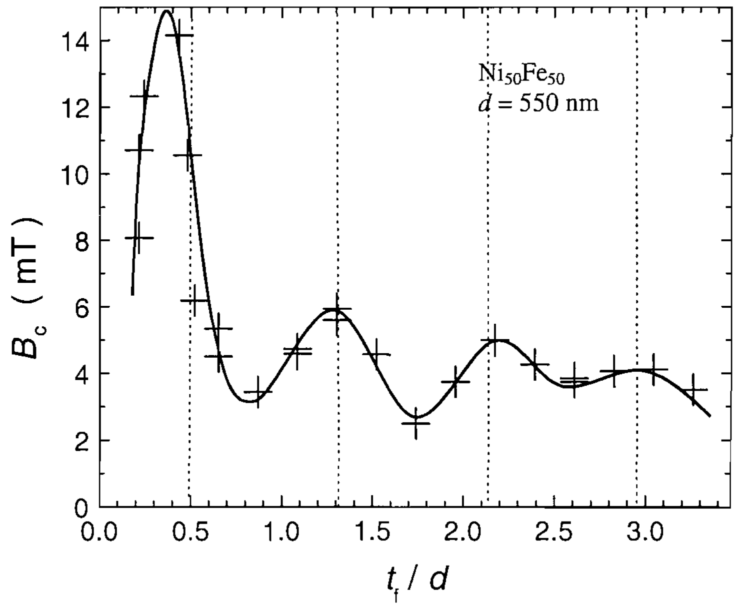

Fig. 4.4. Coercive fields for $Ni_{50}Fe_{50}$ films with different values of thickness, t_f. The dashed lines indicate the position of sphere centers for each layer in the close-packed structure. B_c shows maximum close to the sphere centers. The solid line is a guide to the eye.

4.2.4 Domain patterns from results of MFM and 2D micromagnetic simulations

Imaging of the domain structure in anti-dot films was performed using magnetic force microscopy (MFM) technique. MFM experiments have been performed by G. Karapetrov and N. Novosad at Argonne National Laborotary. Theoretically the domain structure has been studied by means of micromagnetic simulations done by H. Fangohr and R. Boardman at the School of Engineering Sciences. An MFM image in the remanent state for a relatively thin (100 nm) Co film with period $d = 700$ nm is shown on Fig. 4.5a. It demonstrates an ordered, rhombic magnetic pattern associated with the hole array. Magnetic structures for 2D array of holes were modeled using OOMF software package. Parameters for the simulation were chosen in accordance with known values for Co and hole diameters of 0.4 d.

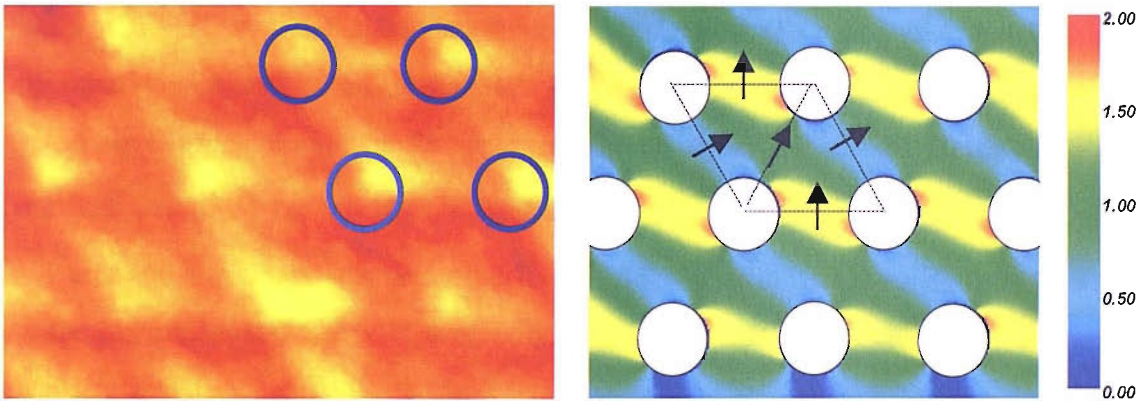

Fig. 4.5 MFM image of Co anti-dot film in the remanant state (a) and results of the micromagnetic modeling with OOMF for 2D array of holes (b). The diameter of holes is 0.4d

Results of micromagnetic modeling demonstrate that in order to decrease the total magnetic energy the structure is divided into three different domains: two in regions between nearest neighbors and the third with a diamond-shape bounded by four holes (Fig. 4.5b). The direction of magnetization in domains between nearest holes is perpendicular to the vector connecting these holes. In the diamond-shaped domains magnetic moments are aligned along the vectors connecting holes. As can be seen in Fig. 4.5 results of 2D modeling are consistent with MFM images. This is due to the small film thickness, which leads to a localization of magnetic moments in the plane of the film. The complete magnetic structure of 3D anti-dot films and oscillatory behavior of the coercivity requires a complete set of 3D micromagnetic modelling, which due to the large number of computational cells required for reliable data, is still beyond the capabilities of modern computers.

4.2.5 2D and 3D models of the domain wall pinning

We can qualitatively understand the results of coercivity measurements, assuming that the domain wall pinning is the main mechanism for the coercive properties. As we know a domain wall is a region of magnetic material separating two domains with opposite directions of magnetization. Inside the domain wall magnetic moments gradually change direction by 180 degrees. The thickness and surface energy density of the wall are given by $\delta = \pi\sqrt{A/K_1}$ and $\sigma = 4\sqrt{AK_1}$, where A, and K_1 are exchange stiffness and anisotropy constant respectively[4]. Such domain walls play an important role in the micromagnetic theory of coercivity in ferromagnetism. If we assume that domain walls in magnetic materials can move reversibly then the magnetization process goes without loss in energy and the hysteresis loop has a shape of a step-function with zero coercivity. In real materials domain walls do not move reversibly because of magnetic (with higher anisotropy) and non-magnetic defects that can increase or lower the energy of the domain wall at that particular position inside the sample. Hence these imperfections work as pinning sites for the domain walls. When the position of the non-magnetic defect is coincident with the domain wall, its energy is minimized by the amount needed to twist magnetic moments inside the volume occupied by this defect. So, the energy of the domain wall varies during its movement through the sample and there are positions when this energy reaches a minimum. The gradient in the wall energy density creates a pinning force $F = -dW_{dw}/dx$ resisting the wall motion. For a homogeneous wall, $W_{dw} = \sigma S$, where σ and S are the surface energy density and an area of the wall. When the external magnetic field is applied it induces a magnetic pressure on the domain wall: $2M_sH$ where M_s is the magnetization of saturation. For fields below H_c magnetic pressure is compensated by a pinning force arising from the gradient in the domain wall energy density. The threshold field corresponding to $(-dW_{dw}/dx)_{\max}$ is taken to be the coercive field, so that[4]:

$$H_c = \frac{(dW_{dw}/dx)_{\max}}{2M_sS} \tag{4.1}$$

In this case as we show below the narrow constriction between the spherical voids are the main pinning sites. The amount of pinning sites varies periodically with the film thickness t_f and leads to oscillatory $B_c(t_f)$ dependence. In our model similar to models of domain wall pinning by inclusions[5] we neglect magneto-static effects, which arise due to non-compensated magnetic poles at the surface of the spherical voids and the contribution to the coercivity from the magneto-crystalline anisotropy. These factors can give some quantitative corrections but will not change qualitatively the behaviour that we find in our simple approach.

Let us first consider a simplified 2D model of a flat domain wall with thickness δ pinned by a square array of holes with radius r and period d. For **B** parallel to the side of the square we can describe pinning by interaction with two holes (Fig. 4.6). For **B** = 0 the domain wall will adopt a configuration with the smallest surface energy along the line connecting the centres of the holes $W_{dw} = t_f \sigma L(x)$, where σ, t_f and $L(x)$ are the wall surface energy density, the film thickness and the length of the domain wall. Applied magnetic field induces a magnetic pressure $2M_sH$, which acts on the wall. Using the equation for the coercive field (4.1), given above we can write:

$$H_c = \frac{1}{2M_sS}\left(\frac{dW_{dw}}{dx}\right)_{\max} = \frac{\sigma}{2M_sL(x)}\left(\frac{dL(x)}{dx}\right)_{\max} \tag{4.2}$$

We have assumed that σ is constant in these calculations. The length of the wall can be derived easily using Fig. 4.6:

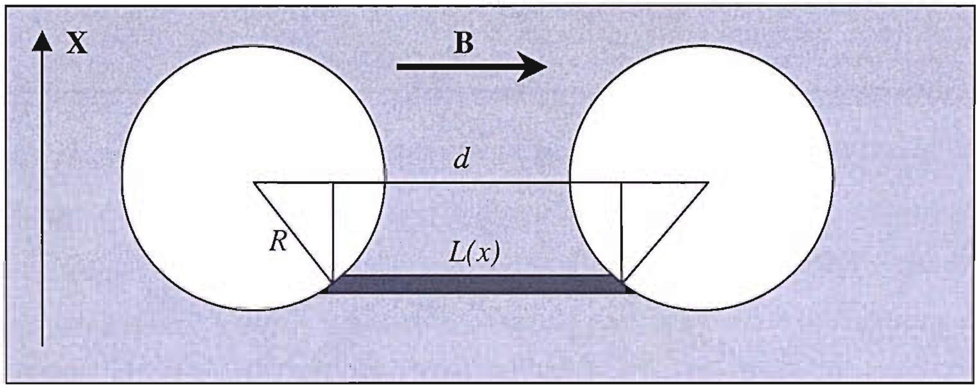

Fig. 4.6 2D domain wall pinning model consisting of a square array of holes. The gradient in surface energy of the domain wall with length L(x) produces a pinning force counteracting a pressure induced by the applied magnetic field.

$$L(x) = d - 2(R^2 - x^2)^{1/2}. \tag{4.3}$$

The derivative $\frac{dL(x)}{dx} = \frac{2x}{\sqrt{R^2 - x^2}}$ diverges for $x = R$. However, this results from neglecting the finite thickness of the wall. We assume that the pinning force has a maximum value when the center of the domain wall approaches the edge of the hole at a distance equal to half the domain wall thickness, $\delta / 2$ which corresponds to $x_{\text{max}} = R - \delta / 2$. For small domain wall widths in the limit $\delta << R$ this gives:

$$B_c = \frac{\sigma}{M_s d}\sqrt{\frac{R}{\delta}} \tag{4.4}$$

For $R = d/2$ this reaches a maximum and results in $B_c \propto d^{-1/2}$. For the weak pinning case, $\delta >> R$, a modified approach of this simple model gives $B_c \propto d$ (see also Ref. 1). Combining these two relations with opposite behavior of B_c we conclude that the coercive field reaches a maximum for $\delta \sim R$ in agreement with our data.

This simple model was extended to the case of a 3D structure of close packed spherical voids. Again we assume a flat domain wall with width δ extending in the directions perpendicular to the substrate and perpendicular to a line connecting in-plane nearest-neighbor spheres Fig. 4.7. The volume of the domain wall V_{dw} and its average surface area S_{dw} depends on its position x in the direction perpendicular to its surface. Using the same model analysis it can be shown that coercive field is now proportional to the $(S_{\text{dw}}^{-1}\, dV / dx)_{\text{max}}$. So the numerical calculations were made to find the maximum

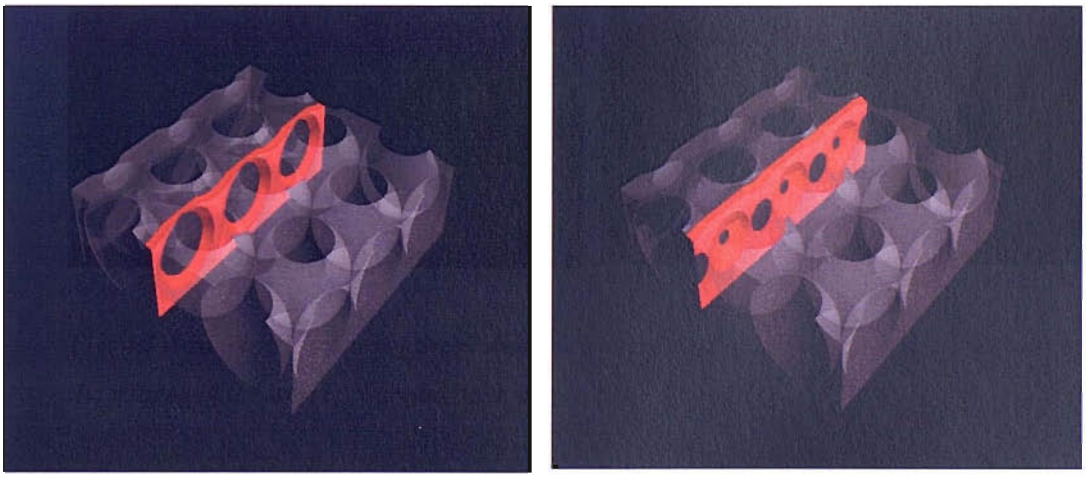

Fig. 4.7 A simple 3D model of the plain domain wall pinning. Figures (a) and (b) show how the volume of the wall is changing with its position .

values of the gradient dV / dx in the fcc structure for different parameters d and t_f. The source code written in C++ can be found in Appendix 1. This code is a set of functions calculating positions of spherical voids, volume of the domain wall V_{dw} and derivative dV / dx. A model of the sample actually corresponds to a fcc structure of spheres with interlayer distances $\varphi_x = d$, $\varphi_y = d\, 3^{1/2} / 2$ and $\varphi_z = d\, (2/3)^{1/2}$. The position for the centers of these spheres $O_{i,j,k}(x_{i,j,k},\ y_{i,j,k},\ z_{i,j,k})$ are defined by three numbers i, j and k with conditions $0 < i < N\_x$, $0 < j < N\_y$ where N_x and N_y are numbers of layers in X and Y directions respectively. The number k varies from 0 to the value restricted by the film thickness. The first task is to find the areas of the infinitely thin domain wall with pores for a discrete set of positions in x-axis and given film thickness t_f. Using integration after that we will find the volume of the domain wall. We consider a plane parallel to the YOZ plane cutting the structure of spheres at the arbitrary point x (Fig. 4.8) and calculate the area, which is cut by whole and partial spheres in this plane, for this point. Let us find two different cross-section areas cut in the plane by the whole sphere with center in $O_1(X_{n,l,m}, Y_{n,l,m}, Z_{n,l,m})$ with position numbers n,l,m and by the partial sphere with center in $O_2(X_{o,p,q}, Y_{o,p,q}, Z_{o,p,q})$ with position numbers o,p,q both satisfying a condition:

$$|x - X_i| < d / 2. \qquad (4.5)$$

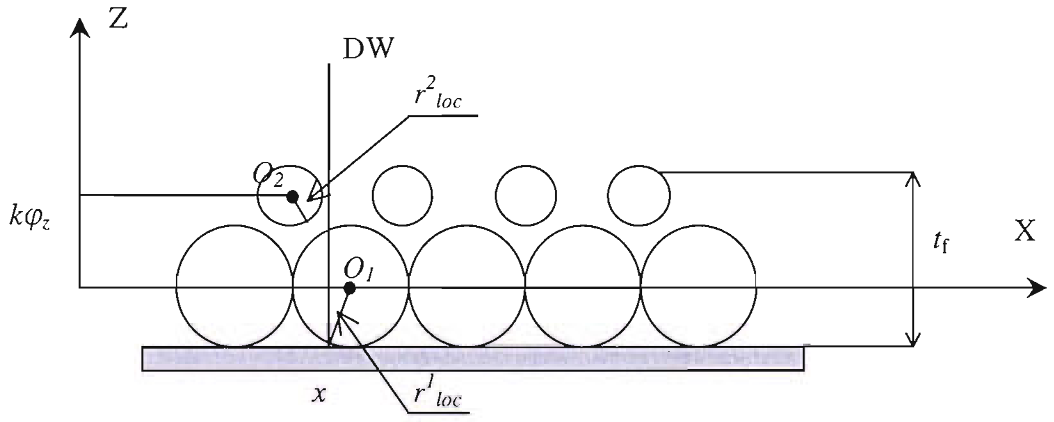

Fig. 4.8 A schematic representation of the infinitely thin domain wall cutting the fcc structure of spheres. The plane representing the domain wall is parallel to the YOZ plane and is moving in positive x-direction.

The local radius, which is a function of x, for both spheres has been computed by equation, which can be easily derived from the Fig. 4.8. This relation works for all spheres in the array satisfying the condition (4.5) and in the general case for a sphere with position numbers i,j,k has a form:

$$r_{loc}^{i,j,k} = \sqrt{\frac{d^2}{4} - \left(x - X_{i,j,k}\right)^2} \tag{4.6}$$

For the group of spheres, that are not cut by the film surface at the position of the domain wall which means that $r_{i,j,k}^{loc} \leq t_f - h$, where $h = k\varphi_z + d/2$ and $k_{\max} = Int\left(\frac{t_f - d/2}{\varphi_z}\right)$, the area subtracted from the plane is $\pi(r^{loc})^2$. Hence for the sphere with numbers n,l,m on the Fig. 4.8 the area is:

$$S_{n,l,m} = \pi(r_{n,l,m}^{loc})^2 \tag{4.7}$$

Now we consider the other group of spheres cut by the surface. The cross-section view of the sphere with a top removed is shown on Fig. 4.9 for two cases: with less and more than a half of the sphere remaining. For the former case the area of the remaining segment is computed as follows:

$$S_{i,j,k,} = (r_{i,j,k}^{loc})^2 \arccos\left(\frac{k\varphi_z + d/2 - t_f}{r_{i,j,k}^{loc}}\right) - r_{i,j,k}^{loc}\left(k\varphi_z + d/2 - t_f\right)\cdot\left[1 - \left(\frac{k\varphi_z + d/2 - t_f}{r_{i,j,k}^{loc}}\right)^2\right]^{1/2} \tag{4.8}$$

with the condition: $t_f \leq k\varphi_z + d/2$ (see Fig. 4.9a).

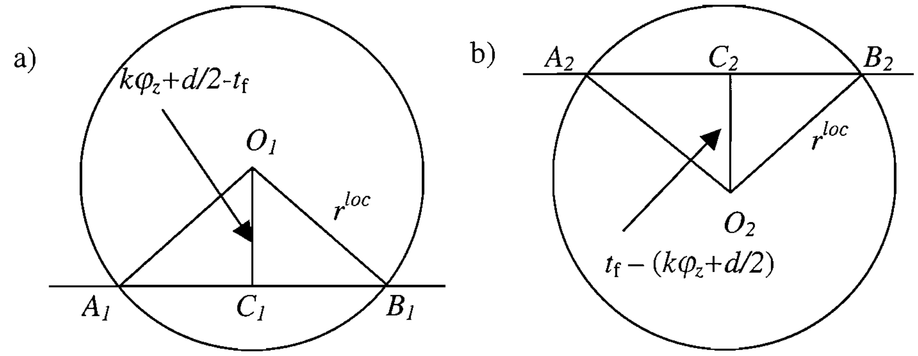

Fig. 4.9 Cross-section view of spheres, cut by the domain wall and film surface at the arbitrary position x. A_1B_1 and A_2B_2 show the intersection with the film surface.

When the sphere is cut so that $t_f > k\varphi_z + d/2$, see Fig. 4.9b, then the value $S_{i,j,k}$ is simply computed by subtracting the area of the top segment from the circular area:

$$S_{i,j,k} = \pi (r^{loc}_{i,j,k})^2 - \\ - (r^{loc}_{i,j,k})^2 \arccos\left(\frac{t_f - \left(k\varphi_z + \frac{d}{2}\right)}{r^{loc}_{i,j,k}}\right) + r^{loc}_{i,j,k}\left(t_f - \left(k\varphi_z + \frac{d}{2}\right)\right)\cdot\left[1 - \left(\frac{t_f - \left(k\varphi_z + \frac{d}{2}\right)}{r^{loc}_{i,j,k}}\right)^2\right]^{1/2} \qquad (4.9)$$

with the condition: $t_f > k\varphi_z + d/2$ (Fig. 4.9b). Thus for the sphere O_2 we will use equation (4.8) or (4.9) depending on film thickness. From calculated areas for all numbers *i,j,k* we can find the total area cut from the domain wall for the given *x*. The area of the domain wall itself is calculated than by subtracting the total area found using equations (4.7), (4.8), and (4.9) from the area of a rectangle with height t_f and length corresponding to the number of layers in the *Y* direction. Subsequent numerical integration using a trapezium approximation over the domain wall width δ gives the volume of the resulting flat domain wall similar to the one shown in Fig. 4.7. The gradient *dV* / *dx* was calculated by the simple numerical algorithm for derivatives:

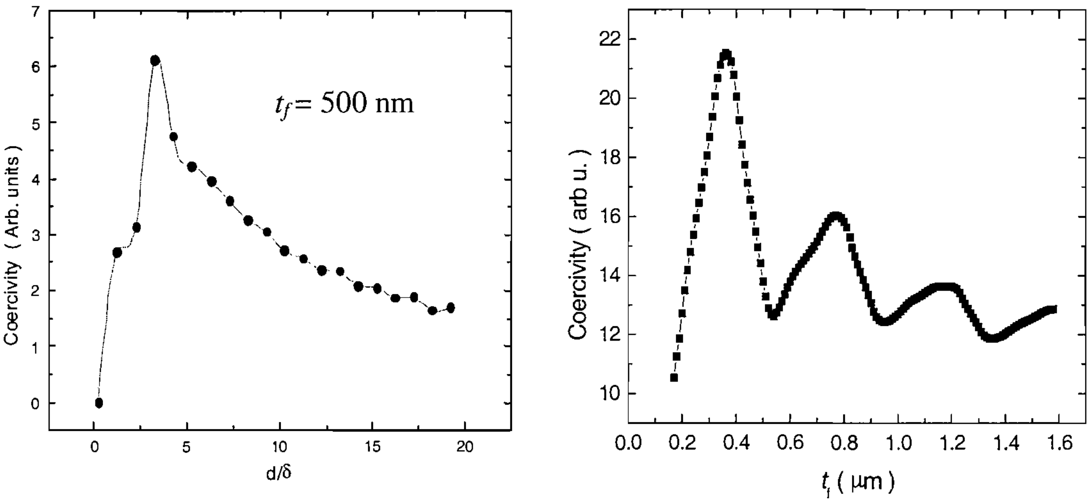

Fig. 4.10 Results of the simple 3D model for the $B_c(d)$ and $B_c(t_f)$ relations. The period of oscillations is about 0.81d in accordance with experimental data.

$\frac{dV}{dx} = \frac{V(x_{i+1}) - V(x_i)}{x_{i+1} - x_i}$ with subsequent maximum determination. Results obtained from this model reproduce the $B_c(d)$ maximum and the $B_c(t_f)$ oscillations found in hysteresis measurements Fig. 4.10.

4.2.6 Azimuthal anisotropy of the coercive field inside crystallites in anti-dot arrays

As was discussed in Chapter 3 the maximum size of crystallites in anti-dot structures can reach up to 1 mm. A crystallite is the area with nearly constant directions of the crystallographic axes. There is a small deviation from these directions induced by deformations at boundaries of crystallites. Using electron microscopy for investigation of such big areas is not convenient because the pixel size for SEM images larger than 100 micrometers is not sufficient to resolve a single sphere. Another way to investigate a crystalline structure is to analyze the diffraction pattern from the periodical array. This method is very useful in crystallography and allows the study of directions of axes and planes inside materials. In our case the incident laser beam is diffracted by the hexagonal array of spheres in a template. Diffraction can be present from these ordered structures only if the following condition is satisfied: $2R \geq \lambda$, where λ is the wavelength of the beam and R is the radius of the sphere. For the HeNe laser with λ = 638 nm this condition gives a value for $R_{\min}$ ~ 320 nm. Studies of crystallite sizes were performed on a template from 900 nm latex spheres. In this experiment the laser beam coming along the normal to the film surface is focused into a small spot ~ 50 μm. This makes it possible to scan crystallites with a relatively good resolution. The diffraction patterns from the sample, mounted on the X-Y translation stage and moved across the beam with resolution 20 μm, are shown in Fig. 4.11. During the scan the diffraction picture rotates along with the crystallographic axes in the array. Fig. 4.11a shows a typical six spot diffraction pattern for the case when the laser spot is focused inside a particular crystallite. If the spot scans inside the same crystallite, the angular positions of diffraction maxima are essentially unchanged.

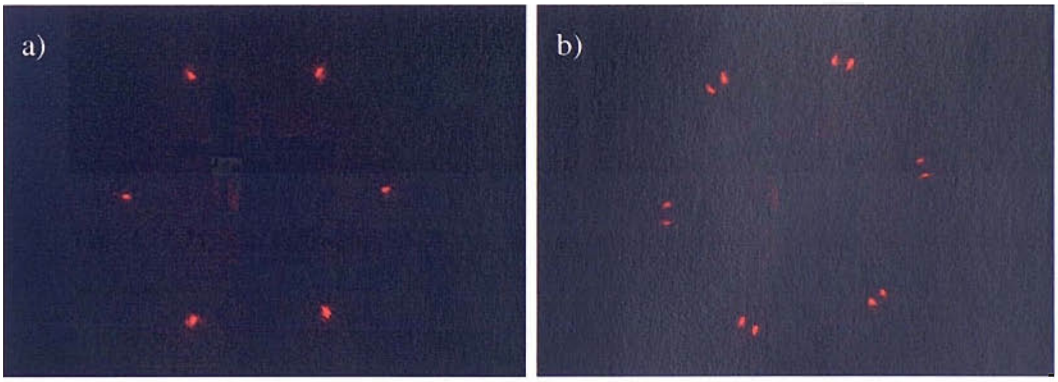

Fig. 4.11 Typical diffraction patterns from a template prepared using latex spheres with d = 900 nm.

When the laser probes two crystallites simultaneously each maximum is doubled (Fig. 4.11b) due to the different direction of crystallographic directions in those areas. Using scans of the laser spot through the sample surface we can find out the size of a particular crystallite. We carried out scanning of the surface and found that in the growth direction crystallites are large indeed. If we plot a dependence of the angular direction for a diffracted spot versus sample position we'll obtain information about the size of the crystallite Fig. 4.12. From this figure we conclude that the length of this particular area is around 700 microns.

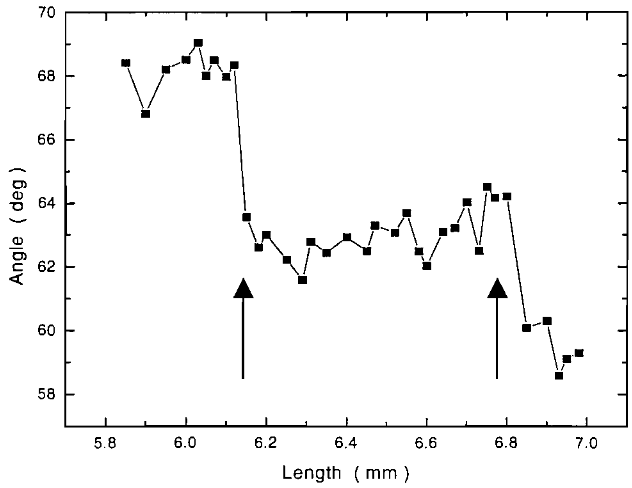

Fig. 4.12 Results of the diffraction experiment showing the size of the crystallite. Arrows mark boundaries between different crystallites

In our further studies we used the MOKE magnetometer to obtain information about the anisotropy of the coercive field inside a single crystallite. For this purpose a Ni film was prepared from the template used in the diffraction experiment and the polarized laser beam was focused onto a crystallite. Remaining in the same crystallite we have measured a set of hysteresis loops for the field applied in the plane of the film but at various angles relative to crystallographic axes. Pictures of diffraction maxima from the sample for several positions were taken to find out directions of symmetry axes in the sample. These diffraction spots represent positions of holes in a reciprocal lattice. When the real lattice rotates the reciprocal lattice rotates as well. Vectors of the reciprocal lattice can be found by formulae[6]:

$$\mathbf{A} = 2\pi\frac{\mathbf{b}\times\mathbf{c}}{\mathbf{a}\cdot\mathbf{b}\times\mathbf{c}},\qquad \mathbf{B} = 2\pi\frac{\mathbf{c}\times\mathbf{a}}{\mathbf{a}\cdot\mathbf{b}\times\mathbf{c}},\qquad \mathbf{C} = 2\pi\frac{\mathbf{a}\times\mathbf{b}}{\mathbf{a}\cdot\mathbf{b}\times\mathbf{c}} \tag{4.10}$$

Here $\mathbf{a},\mathbf{b},\mathbf{c}$ are basic vectors of the crystal lattice and $\mathbf{A},\mathbf{B},\mathbf{C}$ are vectors of the reciprocal lattice. Using these equations one can show straightforwardly that for a hexagonal crystal the reciprocal lattice is the same as the real one but rotated by 30 degrees. The magnetization data revealed an in-plane anisotropy of the coercive force, which can be associated with crystalline structure of the sample – namely the existence of 6-fold symmetry (Fig. 4.13a).

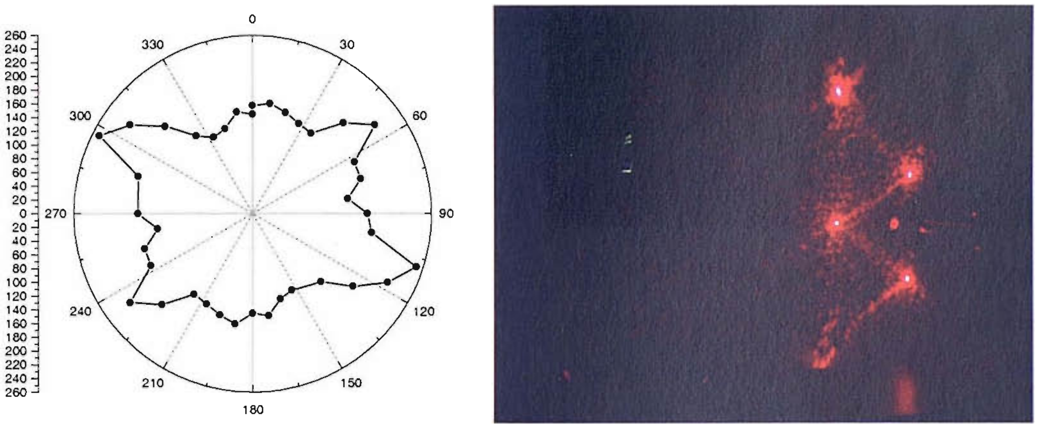

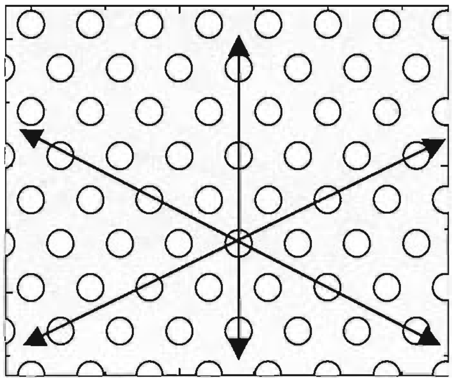

Fig. 4.13 Azimuthal anisotropy of the coercive field inside crystallites resulting from the hexagonal order of the crystallite. Figure (b) shows diffraction spots corresponding to the reciprocal lattice for the angle $\varphi = 0$ from horizontal axis, and (c) a schematic directions of easy axes.

Fig. 4.13b shows a picture of the diffraction pattern (reciprocal lattice image) corresponding to zero angle direction data in the polar plot of coercivity. This data demonstrate existence of three easy directions for the magnetization inside each crystallite. The position of these directions is schematically shown in Fig. 13c. It is worth to notice that anisotropic behavior only exist inside the crystallites and measurements of angular dependence of the coercivity for the whole film did not reveal any particular easy direction because the orientation of crystallites varies within the sample. The main source of this anisotropy must be related to shape effects in the hexagonal array because Ni is magnetically soft material and its magnetocrystalline anisotropy can be neglected. The magnetization data suggest that in our sample the magneto-static energy has extrema in the plane with a period of 30 degrees. As can be seen from Fig. 4.5b and Fig. 4.13c the domain pattern and distance between holes also change with the same angular period, which can be possible reason for the anisotropic properties. Calculations of the magnetostatic energy for nearest neighbours in the saturated state for the two dimensional array of holes using the equation for dipolar interaction did not reveal any azimuthal anisotropy in magnetostatic energy. For the non-saturated case micromagnetic simulations show clear six-fold magnetic symmetry and a six-fold anisotropy for the coercive field.

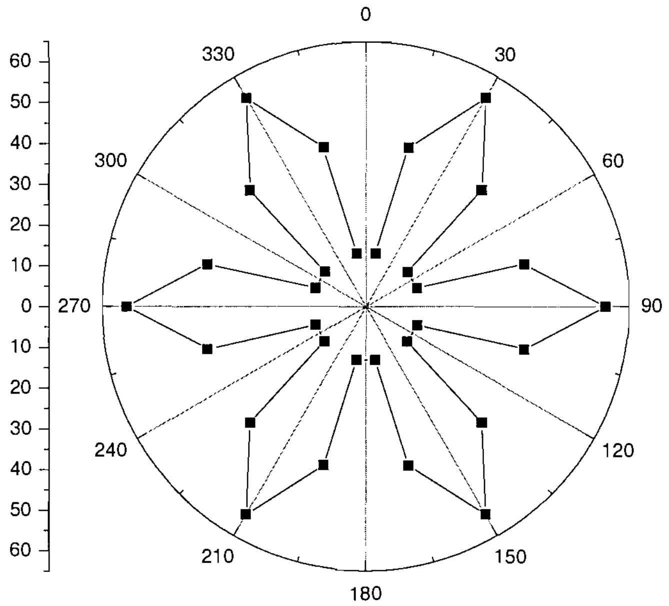

Fig. 4.14 Results of 3D micromagnetic calculations for the coercive field along three azimuthal directions in a hexagonal lattice of holes extended, using symmetry, for 360 degrees. Starting direction for the coercivity is along closest neighbours.

The magnetization is dominated by diamond-shaped domains, (Fig. 4.5b), and prefers to orient along diagonals of the rhombs to save the magneto-static energy. Fig. 4.14 shows a polar plot of coercive field found by R. Boardman using 2D simulations. The starting direction of the applied magnetic field in calculations was set along a side of triangle. These results confirm that easy directions are tilted by 30 degrees from sides of triangles.

4.3 Magnetism of nano-scale dot arrays from self-assembly method

4.3.1 Introduction

The magnetism of nano-scale dot arrays has attracted much attention due to possible application of nano-particles in patterned magnetic recording media[7]. An impressive increase has been made in recording density over the past few years and is now reaching values in excess of 100 Gb/in^2. Modern materials for recording are based on granular thin-film media composed of a regular array of isolated single-domain particles. These magnetic elements have a large remanent magnetization. Up to now, all improvements in the information recording density have been made by decreasing the dimensions of the recording grains. But today this progress is altered by the fundamental super-paramagnetic limit. This effect appears in small nano-particles and leads to a decay of remanent magnetization with time due to thermal excitations[8]. This problem encourages scientists to develop new types of recording media. One example of such novel materials is patterned media[4,7]. In this new method of recording each bit is written in a single mono-domain particle, which can increase the density of recording. But requirements for the dot arrays in this case are very strict in terms of order and periodicity.

Studying magnetic properties of small nano-particles is very important both from a fundamental and practical point of view. In contrast with anti-dot arrays, in small particles the multi-domain state is not favorable due to high cost of formation of domain walls. Calculations of the critical size for the transition between multi-domain and single-domain states in the general case is quite complicated due to the non-uniform magnetization. Exact solutions have been derived for particles with spherical and cylindrical symmetry[8,9]. The switching mode of a single-domain state depends on the balance between exchange, magnetostatic and magnetocrystalline anisotropy energies of the particle and can be as follows: coherent rotation, curling and buckling[8]. The demagnetisation energy is lowered by introducing inhomogeneity into the distribution of magnetic moments whereas the exchange energy is reduced with increasing homogeneity, tending to become a monodomain state. A balance between dipolar demagnetisation and exchange energies determines a wealth of different behaviour depending on array parameters. Recently magnetic vortex behavior, which is close to the curling mode, has been found in small nano-disks[10]. We have investigated some of these structures used both experimental studies and 3D micromagnetic simulations.

4.3.2 Magnetic hysteresis of isolated quasi-spherical dots

We have investigated the magnetic properties of Ni nano-dot arrays produced by the self-assembly method. Well isolated dots with a ratio t/d = 1/3 have been prepared from spheres of diameters d in a range from 200nm to 700nm. Magnetic measurements have been performed using a vibrating sample magnetometer and magneto-optical Kerr effect rig. Experiments have been mostly performed at room temperature with the magnetic field applied parallel and perpendicular to the film plane

The magnetisation curves of these arrays reveal different behavior depending on array parameter d. For large d we observe quasi-reversible behavior. Fig. 4.15a demonstrates a typical vortex-like magnetization curve for an array of separated quasi-spherical dots prepared from 500 nm spheres measured by MOKE magnetometer. In contrast with the results obtained from lithographically prepared nano-discs we found together with micromagnetic modeling the existence of two types of vortices in quasi-spherical dots. Due to the shape of the dot the vortex can be formed either with its core lying parallel to the top surface or pointing parallel to its symmetry axis. The energy balance is different for these two cases hence the formation of each type is controlled by the external magnetic field, shape and size of the dot.

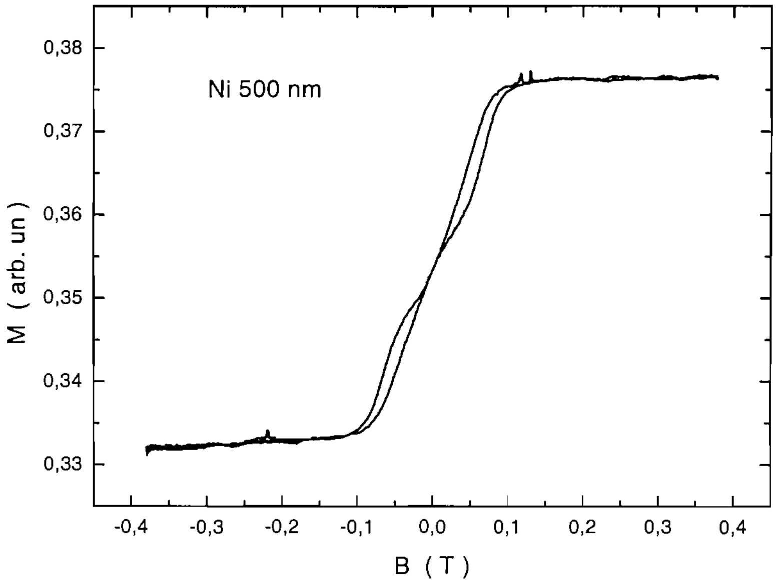

Fig. 4.15 M-H curve for the quasi-spherical dots prepared from 500 nm spheres measureb using MOKE magnetometer. The magnetic field is in the plane of the film.

The magnetization loops obtained by R. Boardman and H. Fangohr, using 3D micromagnetic modeling (see Fig. 4.16a) consists of six intervals. The starting point is a saturated state – all magnetic moments have the same direction along the applied field. As the magnetic field is reduced to the value of the first transition field, H_1, the minimum energy state becomes a vortex configuration with a core, lying in-the plane of the film. For the fields close to the saturation value the energy of the vortex core in the magnetic field is relatively large, which leads to formation of this type of vortex. At the point, corresponding to the second transition field H_2 the Zeeman energy of the core decreases to a critical value and the vortex core flips by 90^0. Movement of this transverse-core vortex corresponds to the remaining part of this loop until saturation at larger negative fields. The experimental curve in Fig. 4.15 does not show a transition from the in-plane core vortex to the transverse core vortex as the loop in Fig. 4.16a. This difference can be understood if we assume that the thickness of the dots in the experiment was less than in the simulations. Fig. 4.16b shows a calculated loop for a thinner dot with the same sphere diameter. As can be seen from this figure the in-plane-core vortex is not formed anymore, which may be the case realized in the experiment. This behaviour can be related to the strong dependence of the reversal mechanism on the dot thickness, namely a high cost in the exchange energy to form in-plane-core vortex in thinner dots. Other aspects such as magnetic coupling in the array and dot shape variations may also be an important factor.

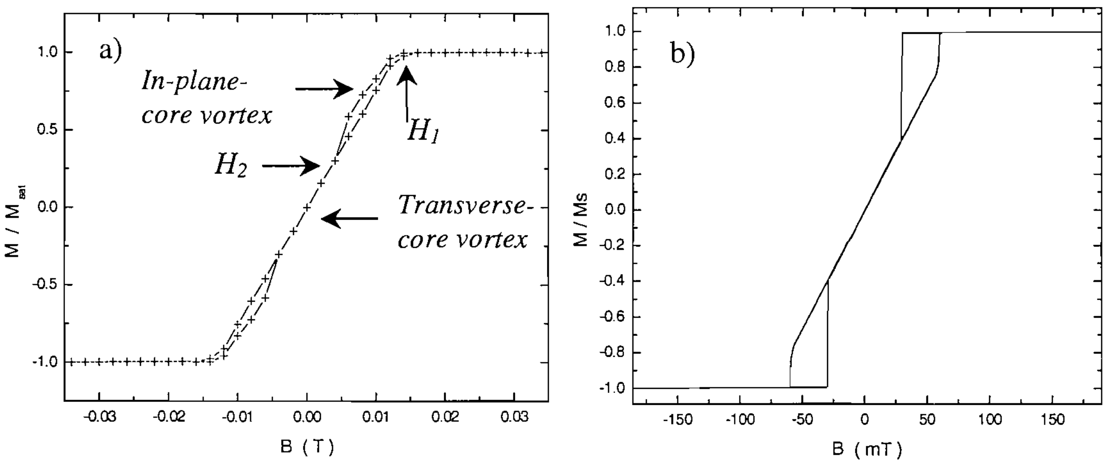

Fig. 4.16 Numerical M-H curves for quasi-spherical dots prepared from 500 nm spheres. The left curve corresponds to a dot thickness 3d/7 and the right one was calculated for a dot with thickness d/5

Results obtained using the VSM show that for large dots with periods ≥200 nm magnetisation curves are essentially linear at low fields and reversible (Fig. 4.17a). In this case the magnetisation reversal process seems to be dominated by demagnetisation resulting in reduced internal field $\mathbf{H}_i$ due to the dot shape with demagnetisation factor N: $\mathbf{H}_i = \mathbf{H}_{app} - N\mathbf{M}$. For small intrinsic coercivities, this produces a linear $\mathbf{M} = \mathbf{H}_{app} / N$ relation similar to Fig. 4.17a.

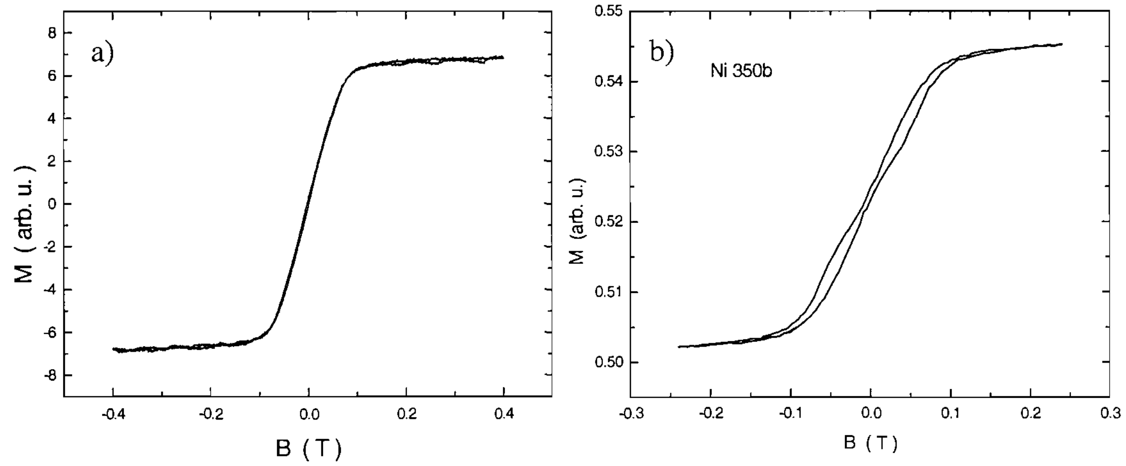

Fig. 4.17 Magnetization curves for dots with quasi-spherical shape measured using VSM and MOKE magnetometers give loops with different shapes, but the slope and the saturation field are similar.

We can estimate the saturation field and a slope of the M-H curve if we describe our dots as oblate ellipsoids. The demagnetizing factor for such ellipsoid with an aspect ratio c and magnetized along a long axis can be found by equation[4]:

$$N = \frac{1}{2}\left\{\frac{c^2}{\left(c^2-1\right)^{3/2}}\arcsin\left[\frac{\left(c^2-1\right)^{1/2}}{c}\right] - \frac{1}{c^2-1}\right\} \tag{4.11}$$

The value of c for our dots can be estimated from the relation between d and the radius of the dot: $r = d\ (2)^{1/2}/3$. Actually because of the droplet convex top this value is slightly smaller. The estimated aspect ratio from these values is equal to $r/t = \sqrt{2}$. This ratio, which is responsible for the demagnetizing factor and hence for the magnetostatic energy term, remains unchanged for all arrays. Using the equation (4.11), the value of N was found to be 0.28 and the experimental value for linear slope is in rough agreement with our estimate. Using the known value of saturation magnetisation for Ni: $4\pi M_S = 6.2$ kGs we can estimate the value of the saturation field by formula: $H_s = NM_s$. This gives ~ 1700 Oe as a transition point to saturation in good agreement with the experiment. The saturation field, as found in the experiment, is not dependent on the period d. The reason for this fact is the demagnetizing field inside dots, described above, which is not changing with period. Indeed, this field is proportional to N, which is a function of the aspect ratio and not of the size. As was discussed above the aspect ratio for all arrays has the same value.

For quasi-spherical dots we do not see the impact of the in-plane-core vortex in magnetisation curves measured by the VSM for our studied periods ≥100 nm. In MOKE we observe a clear irreversibility with behaviour characteristic of a vortex state (Fig. 4.17b). In contrast to the global magnetization measurements by VSM and SQUID, the MOKE light spot probes only the surface layer to the depth of about 10 nm[12].

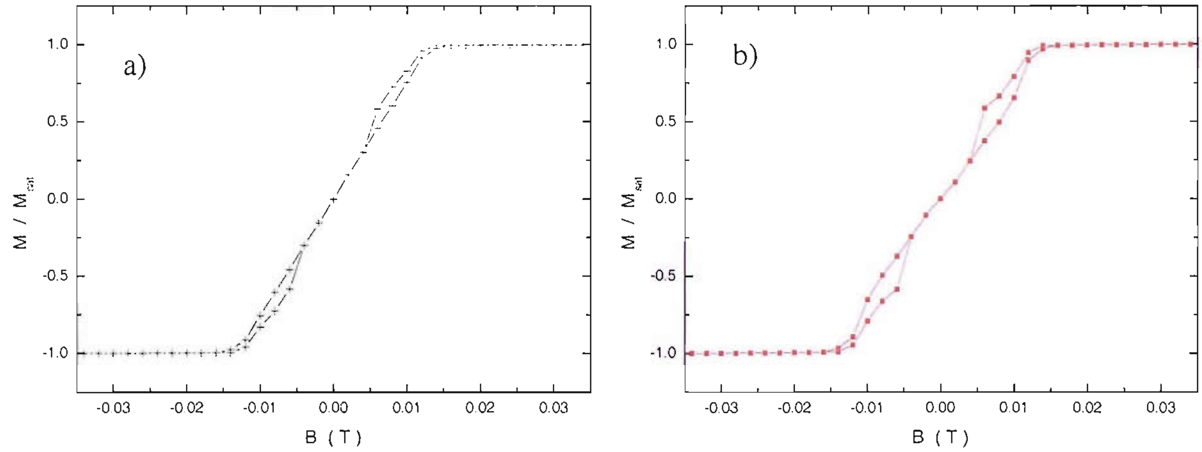

Fig. 4.18 Results of 3D micromagnetic simulations for volume (a) and surface (b) magnetization processes in quasi-spherical dots with bonding diameter 500 nm.

3D micromagnetic simulations have been performed for a quasi-spherical dot with binding diameter 500 nm. One hysteresis curve has been calculated for a whole dot and other for the surface layer only. These results are shown on fig. 4.18. Magnetization loop, obtained for volume measurements, shows two small irreversible parts (fig. 4.17a), which could be hard to detect by global magnetization measurements. The surface loop has larger irreversibility (fig. 4.17b). This interesting behaviour is not observed in 2D magnetic nano-discs where the in-plane-core vortex is not present. For comparison, Fig. 4.18 shows hysteresis curves of a 1000 nm permalloy nano-dot array with period of 2 microns and thickness of 20 nm, prepared by e-beam lithography, measured by two techniques.

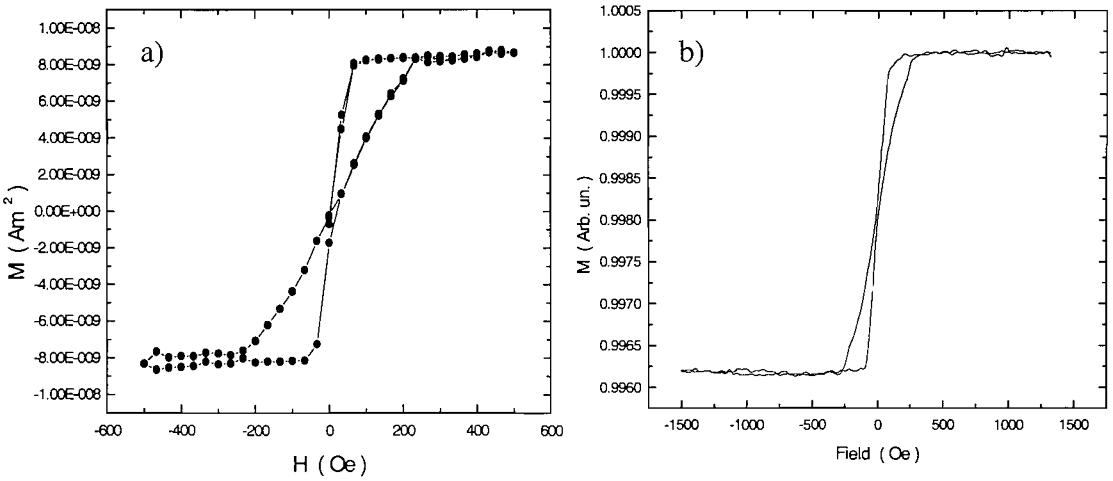

Fig. 4.18 Magnetization loops measured by SQUID (global magnetization measurements) and by MOKE (surface sensitive method) reveal vortex-like hysteresis in both cases for lithographically prepared nano-disks.

We also studied magnetization reversal for the magnetic field applied transverse to the film plane. Fig. 4.19 demonstrates a magnetization curve for dots prepared from 700 nm spheres with saturation field ~5kOe. This value is about five times larger than that observed for the magnetic field applied in the plane due to the higher demagnetizing factor in this direction. It has been confirmed using 3D micromagnetic simulations that the magnetization process involves formation of the transverse-core vortex state for intermediate fields. Let us start from a saturated state with all magnetic moments pointing perpendicular to the film. When the applied field is reduced from its saturation value, magnetic moments start to form a vortex under the action of the demagnetizing field, as confirmed by micromagnetic modeling done by R. Boardman, tilting from their aligned up directions and forming a flux-closure configuration in the plane.

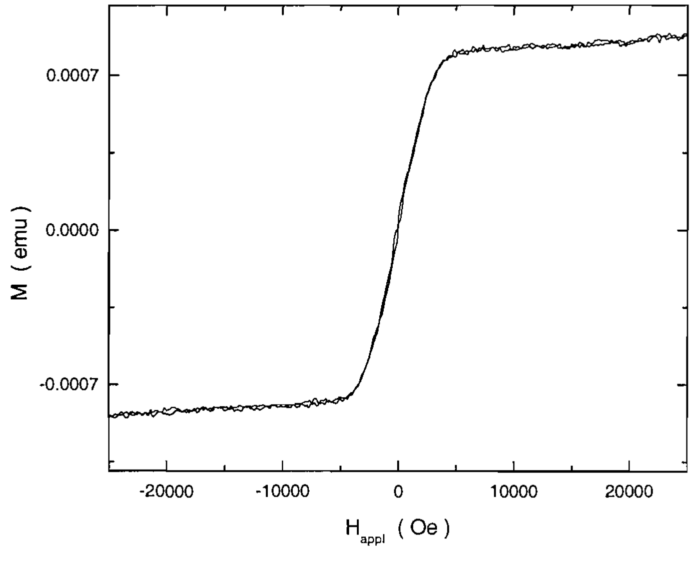

Fig. 4.19 Bulk magnetization measurements for Ni quasi-spherical dots prepared from 700 nm spheres obtained using VSM for the field applied transverse to the film

Because this vortex has a transverse core, the direction of magnetic moments inside the core coincides with the direction of the external field minimizing the Zeeman energy and as a consequence the vortex core flips up and down with the field, depending on the magnetization cycle. The saturation field and the slope of this curve can be estimated again from the demagnetizing effect. Using the value for M_s in Ni and the demagnetizing factor for the magnetization along the hard direction (N = 0.44), the saturation field H_s was found to be ~ 3 kOe in agreement with experimental data.

4.3.3 Transition from the vortex to coherent rotation mode

The critical size for the transition between vortex and coherent behaviour will be affected by dot shape, inter-dot magnetic dipolar interactions and by magneto-crystalline anisotropy of the dots. According to our measurements, unpatterned Ni films produced by the same electrochemical method, are magnetically soft with coercivity of about 50 Oe. In addition, in the arrays investigated, the dots are well separated. Hence the magnetic properties are dominated by intra-dot exchange and magnetostatic energies. Our measurements on the dot arrays allow us to study how the magnetization reversal mechanism

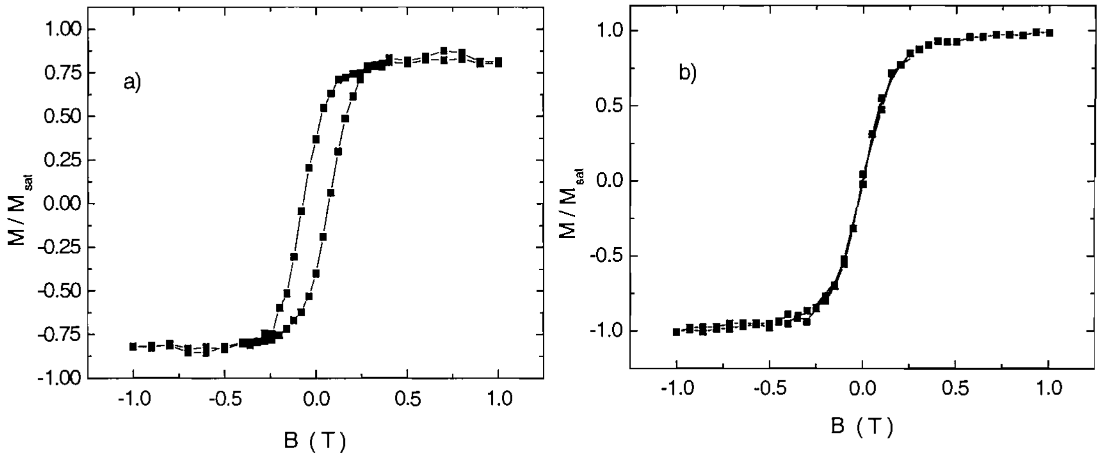

Fig. 4.20 Quasi-spherical dots prepared from 200 nm spheres show existence of the coherent rotation magnetization mode if the field is applied in the film plane (a) and vortex behavior for perpendicular fields (b)

depends on the dot size and at which size the cross-over between vortex and coherent rotation states occurs in dots with a quasi-spherical shape. In the previous paragraph we found that the magnetization process for the transverse and in-plane applied fields has a vortex nature in large dots. In arrays of smaller dots the magnetic behavior changes. Magnetization curves for a dot array with d = 200nm are shown in Fig. 4.20. It can be seen that for the magnetic field applied in the plane of the array the magnetization reversal is similar to a case when all magnetic moments rotate coherently – relatively large hysteresis with a value of the coercive field of about 720 Oe. The squareness of the loop M_{rem}/M_{sat} is 0.45. For lithographically prepared nano-discs of thickness 10nm and 15nm the transition between vortex and coherent rotation behavior takes place for somewhat smaller diameters: ~150nm[11]. This discrepancy may be caused by the difference in materials (our dots are from Ni and permalloy was used in Ref. 10), dot shape and thickness, which in our case was ~70nm. In contrast to the case of fields in the film plane, the behaviour for magnetic fields applied perpendicular to the array reveals a magnetization curve, which remains reversible. In the case of small periods the radius of the dot becomes smaller and for fields in the array plane it is energetically unfavorable for an in-plane-core vortex to form: due to the smaller length scale over which the magnetization would have to turn, the increase in exchange energy inhibits the formation of a vortex. For magnetic fields perpendicular to the array plane, the vortex is set up in the circular cross-section of the dot, which has a lower cost in exchange energy. Micromagnetic simulations have been also done for a set of dots with binding sphere size between 20 and 400 nm[13]. These studies showed that below 140 nm dots have square-like hysteresis while for larger periods the behaviour is vortex-like. This value for the critical size is quite close to the experimental value of 200 nm.

4.4 Conclusion

It has been shown that magnetic nano-structures fabricated by the self-assembly method have a number of new properties in comparison with samples prepared by different types of lithography. The crucial point for this difference is the 3D architecture of self-assembly nano-structures. Magnetic behaviour in dot and anti-dot arrays was found to depend strongly on the array parameters d and t_f. In particular, experimental data for anti-dot structures revealed that a key parameter of ferromagnetic materials, the coercive field, increases dramatically in comparison to its value in plain films. Furthermore the coercivity of these films changes with the size of the spherical voids. The $B_c(d)$ dependence has a characteristic maximum for $d \approx \delta$, where δ is a domain wall width. The main consequence of three dimensional architecture in anti-dot networks is the $B_c(t_f)$ dependence with oscillatory behaviour. Analysis of experimental data was performed by considering 2D and 3D simple approximations of domain wall pinning. These models qualitatively reproduce the results of the experiments but full 3D micro-magnetic modeling is still required to describe the magnetization process in these structures. Furthermore, the arrays of anti-dots have highly ordered structures with large crystallites and this feature resulted in a six-fold symmetry of the coercivity. The main outcome of the work done on magnetic dots is the influence of their quasi-spherical shape on the magnetization reversal mechanism. This resulted in formation of two types of vortices during the magnetization process. Coexistence of two different magnetization modes namely coherent rotation and a vortex state depending on the direction of applied field was found in smaller dots. The critical dot diameter, for the cross-over between the two reversal regimes, which was found experimentally is close to the value obtained in numerical simulations.

4.5 References

---

[1] Skomski, R. & Coey, J.M.D., *Permanent magnetism* (Institute of Physics Publishing, 1999).

[2] R.M. Bozorth, *Ferromagnetism*, Van Nostrand; Macmillan, 1951

[3] Zhukov, A. A. *et al.*, Coercivity of 3D nanoscale magnetic arrays from self-assembly template methods. *J. Magn. Magn. Mater.* Doi:10.1016/j.jmmm.2003.12. 780.

[4] R.C. O'Handley, *Modern Magnetic Materials*, Wiley Interscience, New York, 1999

[5] C. Kittel, Rev. Mod. Phys. **21**, 541 (1949)

[6] C. Kittel, *Introduction to the Solid State Physics*, New York: Wiley, 1996

[7] A. Moser et al. J. Phys. D: Appl. Phys. **35** R157 (2002)

[8] Aharoni, *Introduction to the Theory of Ferromagnetism*, Oxford University Press, 2000

[9] A. Aharoni, J. Phys.: Condens. Matter **9,** 10009 (1997)

[10] R.P. Cowburn et al. Phys. Rev. Lett. **83**, 1042 (1999)

[12] E.R. Moog et al., Phys. Rev. B **39**, 6949 (1989)

[13] R. P. Boardman et al. J. Appl. Phys. **95,** 7037 (2004)

Chapter 5. Magnetic and transport properties of lithographically prepared nano-structures

5.1 Introduction

The self-assembly method allows us to fabricate well ordered 3D structures with unusual magnetic properties, however e-beam lithography remains central technique in the preparation of high quality quasi 2D nano-scale arrays with excellent order for fundamental research. We studied arrays of different NiFe nano-structures including square arrays of anti-dots with various diameters, nano-dots with elliptical shape and aspect ratio a/b ~ 2, arrays of nano-rings with round and square shapes. All measurements were performed using a MOKE magnetometer with longitudinal or transverse geometry.

5.2 Magnetization reversal and shape effects in nano-scale elliptical dots

Arrays of nano-scale dot arrays have been intensively studied over the last few years[1,2,3,4,5]. In this section we present studies of the magnetization reversal in elliptical nano-dots prepared from $Ni_{80}Fe_{20}$ (Fig. 5.1a) using e-beam lithography. The *M-H* curves were taken with magnetic fields applied in the plane of the film and various directions with respect to the long axis of the ellipses. Using a rotational stage, magnetization curves were taken with an azimuthal step of 9 degrees. Magnetization data were averaged over a large amount of experimental loops (approximate value 400) using a Mathcad code specially developed for this project. Results of *M-H* measurement are presented in Fig. 5.1b, where only parts of the loops lying in the first and second quadrants are shown to demonstrate more clearly the impact of the elliptical shape on the coercivity and remanance.

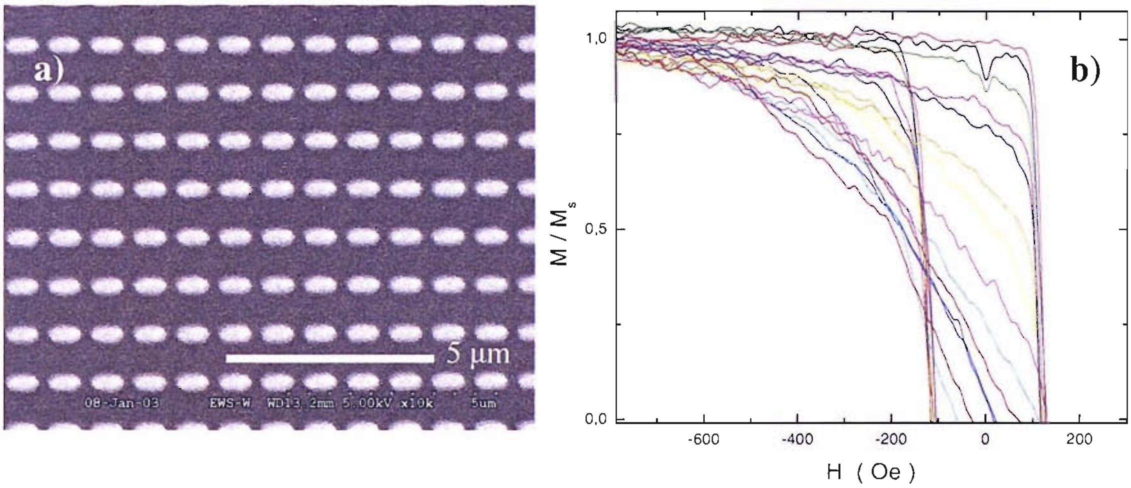

Fig. 5.1 SEM image of the 20 nm thick dot array (a). The long and short axes are 800 nm and 400 nm respectively. Figure (b) shows parts of M-H curves for various angles between the magnetic field and the long axis of the dots in a range between 0 and 90 degrees with an angular step 9 degrees. Red loop corresponds to the 0 degrees magnetization and blue one corresponds to 90 ^{0} *process.*

Hysteresis curves for the two extreme cases when the magnetic fields was applied along the long (a) and short (b) ellipse axes are presented in Fig. 5.2. As follows from the geometry of the sample and *M-H* data, the easy magnetization axis coincides with the long axis of the ellipse. Coercivity and squareness decrease from their maximum values for the easy axis loop and become zero for the hard axis direction along the short axes of ellipses. This result demonstrates a shape anisotropy – the preference for the magnetization to lie in a particular direction in a nanostructured sample from isotropic polycrystalline material.

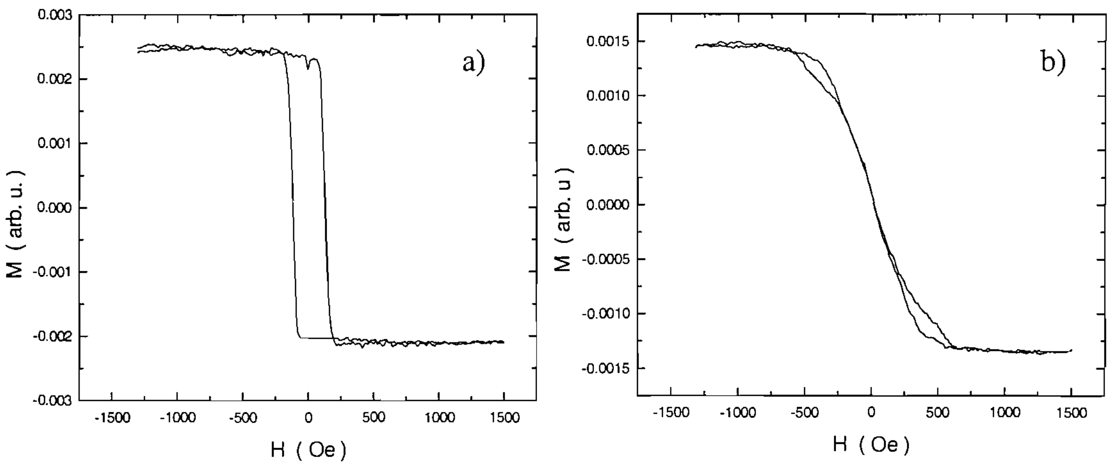

Fig. 5.2 Hysteresis loops for the easy (a) and hard (b) magnetization reversal processes

The origin of the shape anisotropy is related to the magnetostatic energy arising from the dipolar interactions between volume and surface magnetic charges. The shape anisotropy field is proportional to the maximum difference in the demagnetizing fields in two orthogonal directions[6]:

$$H_{shape} = M_s \Delta N \tag{5.1}$$

More detailed analysis gives the relation for the shape anisotropy constant[6] $K_{shape} = M_s^2 \Delta N/2$. In soft magnetic materials where the magneto-crystalline anisotropy is weak, even small demagnetizing effects can have a strong effect on the measured *M-H* response. With decreasing length scale the dipolar interaction energy increases and this effect becomes even more important, leading to large changes in magnetization hysteresis parameters (slope, coercivity, squareness etc.). The polar plot of the coercive field versus direction of the applied field is shown on Fig. 5.3a. It shows very large changes in the coercive field. This behaviour can be immediately reproduced using the Stoner-Wohlfarth (S-W) model of coherent rotation magnetization reversal model.

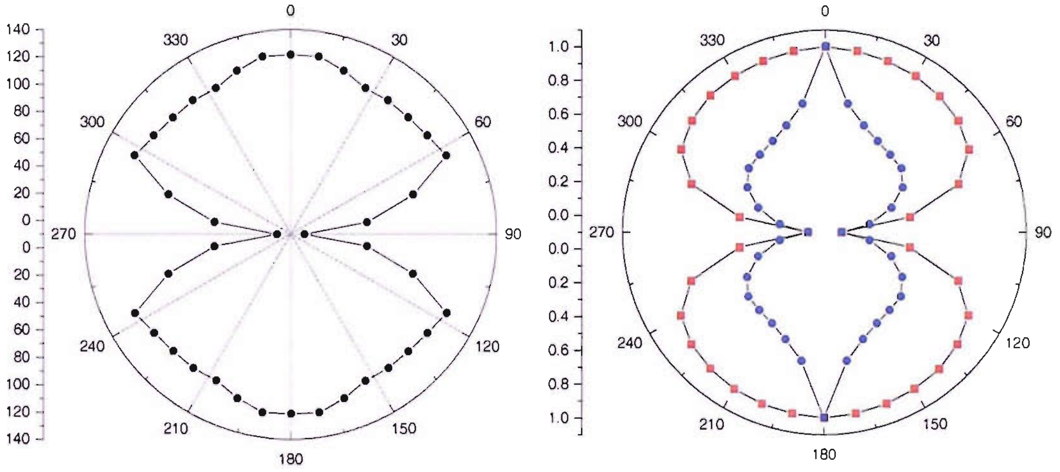

Fig. 5.3 Experimental data for the in-plane anisotropy of the coercive field (a) and results obtained from the S-W model and micromagnetic simulations (b)

This model was introduced in 1948[7]. Since that time it has been successful in describing experimental results. In S-W model the free energy of the ellipsoid is written in the form consisting of anisotropy and Zeeman energy terms[6]:

$$f = -K_u \cos^2(\vartheta - \vartheta_0) - HM_s \cos\vartheta \qquad (5.2)$$

here ϑ_0 is the angle between the field and the easy axis and ϑ is the angle between the magnetization direction and the applied magnetic field. The anisotropy constant includes both magnetocrystalline and shape parts[6]: $K_u = [H_a + (N_2 - N_1)M_s]M_s / 2$, where N_2 and N_1 are the demagnetizing factors perpendicular and parallel to the easy axis of the particle. Detailed calculations in the S-W model give switching and coercive fields. The coercive field is found by setting to zero the magnetization value as follows from the definition of H_c. The switching field is defined as the field when magnetization abruptly changes its direction. Mathematically this condition is written as: $\partial H / \partial M = 0$. Final results for reduced switching and coercive fields can be expressed as[6]:

$$h_s = \frac{H_s}{H_a} = \left(\cos^{2/3}\vartheta_0 + \sin^{2/3}\vartheta_0\right)^{-2/3} \tag{5.3}$$

$$h_c = \frac{H_c}{H_a} = \sin\vartheta_0 \cos\vartheta_0 \tag{5.4}$$

Below 45^0 $h_s > h_c$ the magnetization switches abruptly at h_s and does not follow further *m-h* curve. For $45^0 < \vartheta < 90^0$ the switching commences in the third quadrant hence $h_s < h_c$. Results for h_s below 45^0 and for h_c above this angle obtained from the S-W model are plotted in the Fig. 5.3b by blue closed circles[6]. Comparing this data with our experimental result we found that the coherent rotation approximation does not well reproduce the measured behaviour. The S-W model describes only the general trend for the coercivity fields to decrease with the angle between the magnetic field and the easy axis. The probable reason for this is that the single-domain particles do not always change their magnetization by coherent rotation. The S-W model can only be applied for ellipsoidal particles with sizes below a critical value of the order of an exchange length[8,9]. The magnetization process was also examined by micromagnetic simulations using OOMMF software. Calculations were performed for an elliptical dot of 20 nm thickness.

A damping coefficient was set to 0.5 and cell size to 5 nm. The data from our numeric simulations suggest that the magnetization reversal process along the hard axis occurs through the formation of an S-shaped single domain state (Fig. 5.4b) with zero remanent magnetization in the direction of the applied field.

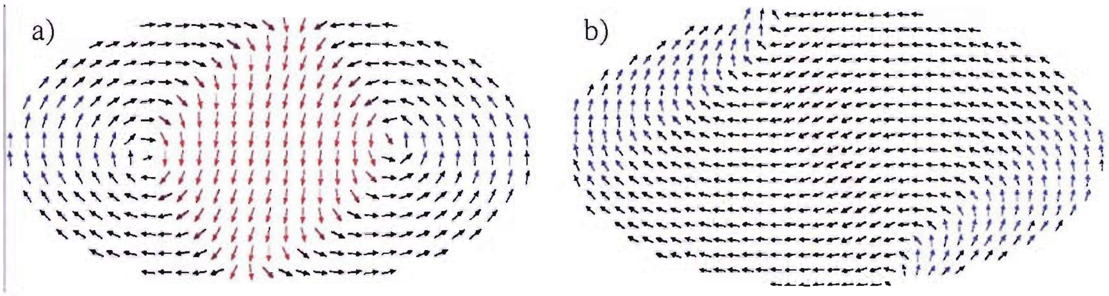

Fig. 5.4 Results of micromagnetic calculations for easy (a) and hard (b) axes reversal processes. Left picture was taken slightly after remanent state and right one was taken before the remanence.

Interestingly, the magnetization reversal for the field applied along the easy axis with a slight offset of 5 degrees involves formation of two vortices (Fig. 5.4a). To check results of simulations for hard axis reversal we have measured the transverse component of the magnetization using the vector-MOKE technique (Fig. 5.5).

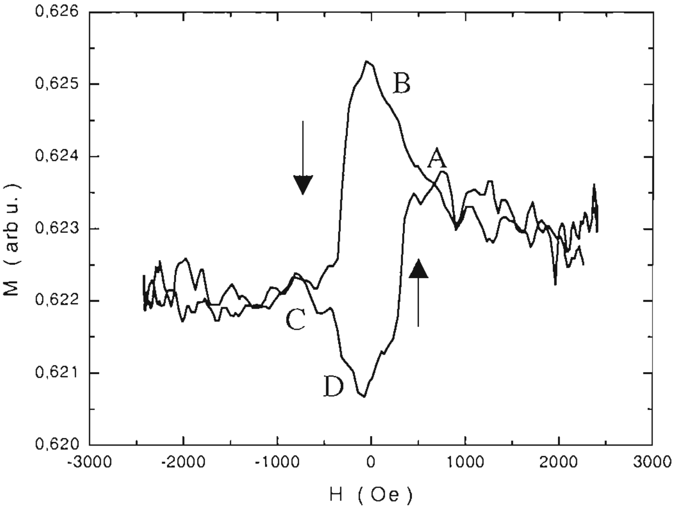

Fig.5.5 Transverse component of the magnetization for the hard-axis reversal process.

In this figure the magnetization along the easy (long) axis is plotted versus the field applied along the hard (short) axis. This loop shows a maximum for the transverse component at zero applied fields. Actually, the S-W hard-axis magnetization should also give a maximum in the transverse component at zero fields, but the shape of the loop for that case is expected to be close to a square rotated by 45 degrees. The shape of the experimental graph does not confirm a S-W reversal. The transitions AB and CD on the experimental curve can be associated with the formation of an S-shaped domain with subsequent saturation at zero fields. Subsequently, the S-shaped domain is formed in the opposite direction and the transverse component is then reduced. Two small irreversible parts in the *M-H* curve in Fig. 5.2 show that processes of formation and annihilation of the S-domain are energetically different.

In conclusion, we have found that the shape effects strongly affect the measured magnetization curves in soft magnetic materials. Attempts to reproduce experimental results on the in-plane anisotropy of the coercive field using the Stoner-Wohlfarth model gave only qualitative agreement but did not describe the reversal process in detail. Results obtained by the OOMMF simulations showed a quite good agreement with experimental data on anisotropy and were helpful in understanding the magnetization reversal mechanisms in these nano-particles.

5.3 Coercivity of square arrays of anti-dots

In this section we discuss coercivities of anti-dot arrays. These structures were prepared using e-beam lithography from 20 nm thick permalloy ($Ni_{80}Fe_{20}$) films (Fig. 5.6). They were square arrays of round holes with periods of d = 1 μm and 2 μm. We have studied magnetic properties using the MOKE magnetometer with the magnetic field applied in the plane of the film. Using rotation of the film around its normal we have studied the in-plane anisotropy of the coercive field in anti-dot films. The presence of holes changes significantly the coercivity properties of magnetic films[10,11].

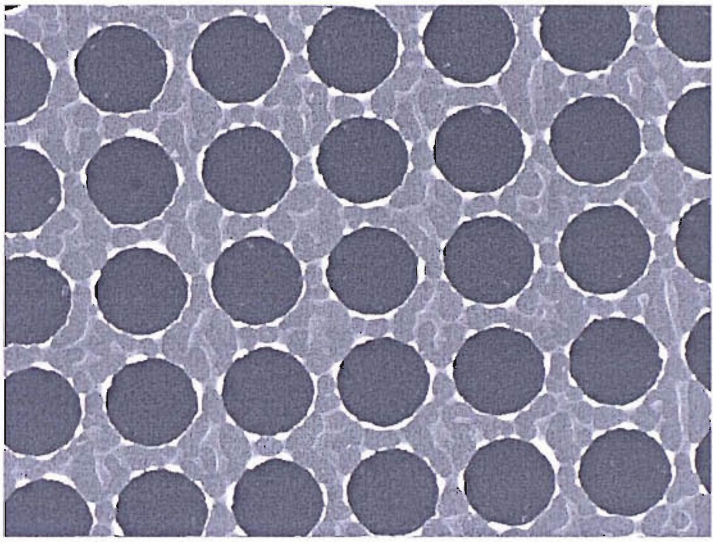

Fig. 5.6 A 20 nm thick permalloy film with anti-dots. The period of the array is 1 micron

The size of holes is also an important factor leading to changes in magnetic behavior. Fig. 5.7 shows magnetization curves of an anti-dot array with period 1μm for the field applied along the side of the square lattice and parallel to its diagonal.

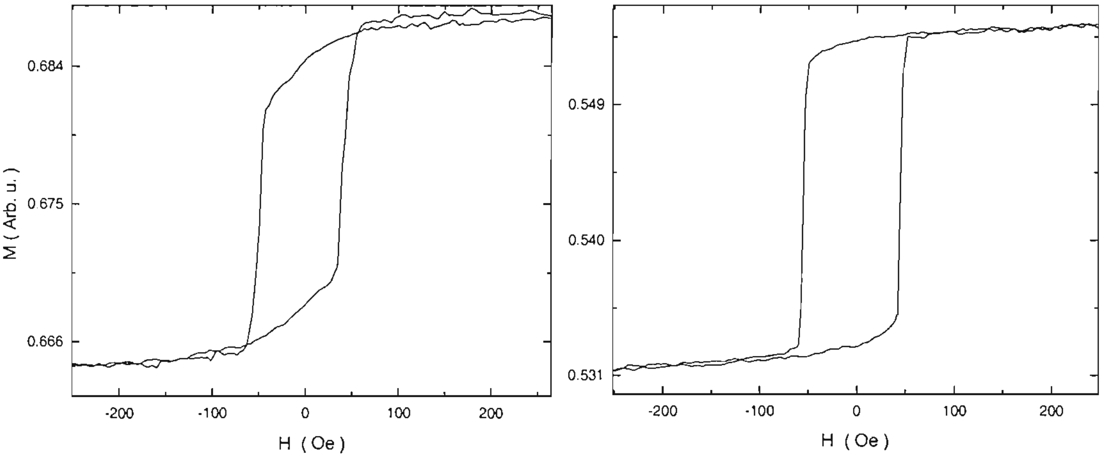

Fig. 5.7 Magnetization loops measured by MOKE for the field applied along the side of the array (a) and diagonal (b)

The magnetization reversal in Fig. 5.7a occurs more gradually with squareness 0.75 while the *M-H* loop along the diagonal (Fig. 5.7b) shows that the magnetization process in this case is abrupt with squareness 0.95. These observations allow us to conclude that the easy magnetization axis lies along the array diagonal. Using 9^0 step in sample rotation we have studied the angular dependence of the coercivity for 180 degrees range. Basing on the inversion symmetry of the *M-H* curves we extended these measurements to 360^0.

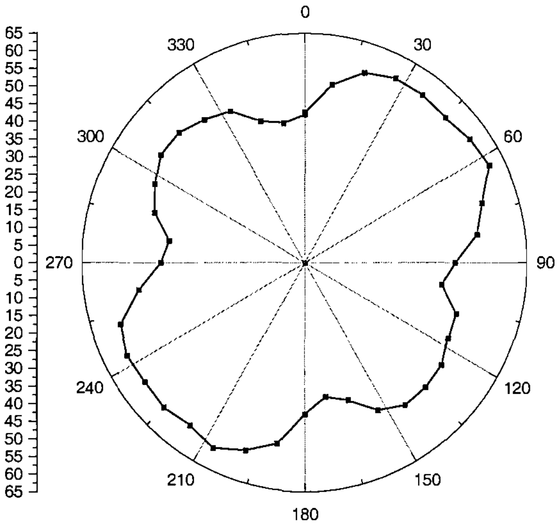

Fig. 5.8 Polar plot of the coercive field as a function of azimuthal angle between the magnetic field and the side of the array. Left side of the plot is a mirror image of the measured right part (0^0 – 180^0).

The resulting angular dependence of the coercivity is shown on Fig. 5.8. It shows the presence of four-fold in-plane anisotropy. The coercive field gradually increases from 40 Oe for the hard axis magnetization to 60 Oe for the easy axis. Four maxima define four easy directions. The maximum variation in coercive field is 27%. These results are similar to those obtained for anti-dot structures from self-assembly method however in the latter case we found six easy directions for magnetization.

We can try to evaluate the contribution of magnetostatic effects, which are responsible for this behavior, by computing a dipolar interaction between holes.

Due to the complexity of this task we were able to find the magnetostatic self-energy of this system only in the saturated states along the side of the square lattice and diagonal. In this approach each hole can be treated as a magnetic dipole and the energy of dipolar interaction between two dipoles is given by the equation:

$$U_{p_1p_2} = \frac{\mathbf{p}_1\mathbf{p}_2 - 3(\mathbf{n}\cdot\mathbf{p}_1)(\mathbf{n}\cdot\mathbf{p}_2)}{r^3} = \frac{|\mathbf{p}_1||\mathbf{p}_2|}{r^3}\left[\cos(\theta_1 - \theta_2) - 3\cos\theta_1\cos\theta_2\right] \tag{5.5}$$

Where **n** is a unit vector in the direction from dipole 1 to dipole 2. If we suppose that all holes have equal magnetic moments $\mathbf{p}_1 = \mathbf{p}_2$ and they all align in same direction (saturated state) this equation takes the form:

$$U_{dipole} = \frac{p^2}{r^3}\left(1 - 3\cos^2\theta\right) \tag{5.6}$$

Using this formula we can find the magnetostatic energy for nearest neighbours in a square lattice. However results appear equal for the array saturated along the diagonal and along the side of the lattice.

More rigorous calculations of the mutual dipolar interaction between magnetic charges in the array of holes were done numerically using a C code. In this method we also find the magnetostatic (MS) energy in saturated states for various directions. When the sample is saturated south and north poles are generated at the interfaces around the holes (see Fig. 5.9). Each magnetic pole creates a magnetostatic potential around itself. Thus if we manage to find the MS potential at any arbitrary point we could then compute the MS energy of the whole array as a sum of linear integrals $U_{ms} = \frac{1}{2}\int \sigma_l \varphi dL$, where σ_l and φ correspond to the linear density of magnetic charges around the hole and the magnetostatic potential respectively.

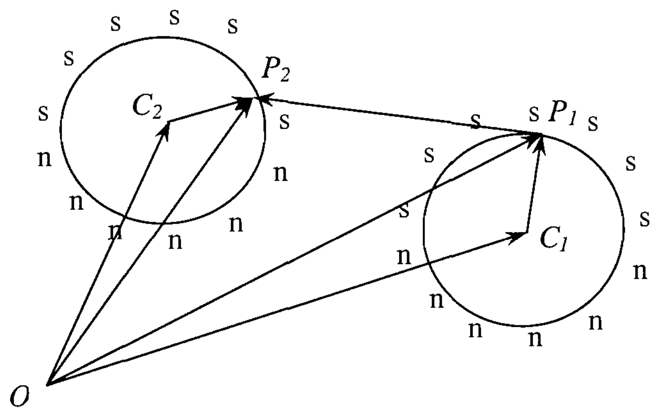

Fig. 5.9 A scheme for calculation of the MS potentials

Calculation of the MS energy using this method involves two integrating steps starting with computation of the potential φ which is used for integration of U_{ms}. Fig. 5.9 illustrates the calculation of the potential in the part dl_1 on the hole C_1 from the part dl_2 on the hole C_2.

Using this approach, the MS energy has been calculated for saturated states along the various directions in the plane of the array. Results also gave an isotropic energy distribution even for the large number of holes.

The in-plane anisotropy in permalloy anti-dot arrays was also studied by C.T. Yu et al[12]. In their work they found that magnetization is dominated by diamond-shaped domains and prefers to align along the diagonals, which leads to a four-fold anisotropy. The torque magnetometry confirmed that at saturated fields this four-fold anisotropy disappears suggesting that its origin is connected with the domain pattern[7].

We also have studied how the coercive field and anisotropy depend on array parameters. For this purpose four samples with different hole diameters were prepared. The period of the arrays was set to 2 microns for all samples. Using the MOKE technique we obtained magnetization curves for various directions of the magnetic field. The results, which we obtained for the coercivity are plotted in the Fig. 5.10a. The coercive field increases for larger holes roughly as $\sqrt{d}$ predicted by the 2D domain wall pinning model described in Chapter 4. Fig 5.10b shows the value of the anisotropy parameter, which we define as $K = \frac{H_c^{\max}}{H_c^{\min}}$ versus the hole size. This data shows that anisotropy strength increases for larger holes. We suggest that the magnetostatic energy term plays an important role in the formation of diamond shaped domains and in the reversal process. From a geometrical point of view the amount of magnetic poles, and hence shape anisotropy effects, are larger for bigger diameters. Thus we should expect an increase in anisotropy due to this effect. In addition the dipolar energy is decreasing as $1/r^3$, hence surface magnetic charges have much stronger action on the reversal in case of larger sizes of holes because they get closer. We conclude that this induced four-fold anisotropy needs more experimental and theoretical studies accompanied by reliable micro-magnetic simulations to find out in more detail the influence of shape effects on the magnetization reversal and coercivity.

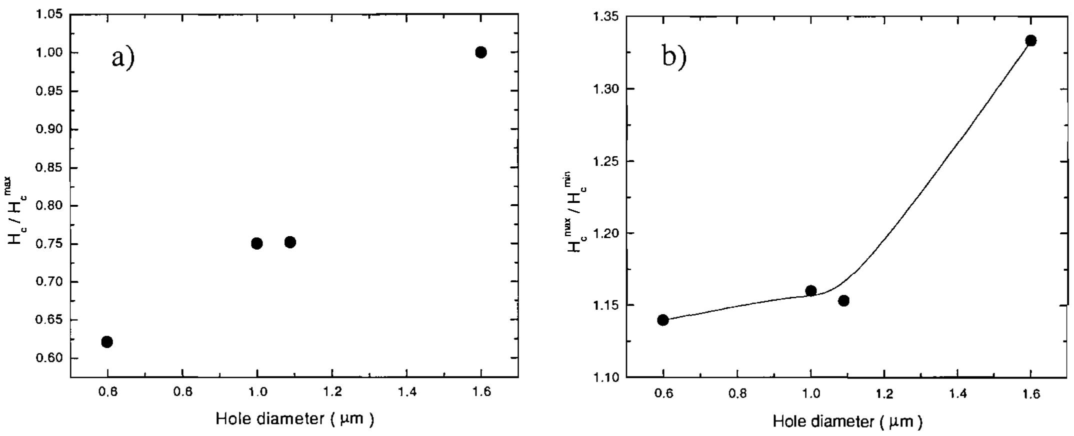

Fig. 5.10 Coercive field of anti-dots versus the hole size (a). The right graph (b) represents a dependence of the anisotropy strength $K = H_c^{\max}/H_c^{\min}$ *on the hole size. The period of the array in both cases is 2 microns*

5.4 Magnetization reversal and azimuthal anisotropy of coercivity in two-dimensional arrays of square nano-rings

The magnetic reversal processes in arrays of square-shaped nano-rings were studied by MOKE magnetometry and micromagnetic simulations. Arrays of rings had a thickness of 20 nm, lateral size of 950 nm and line width 150 nm. The separation distance between rings in the array was 75 nm (Fig. 5.11).

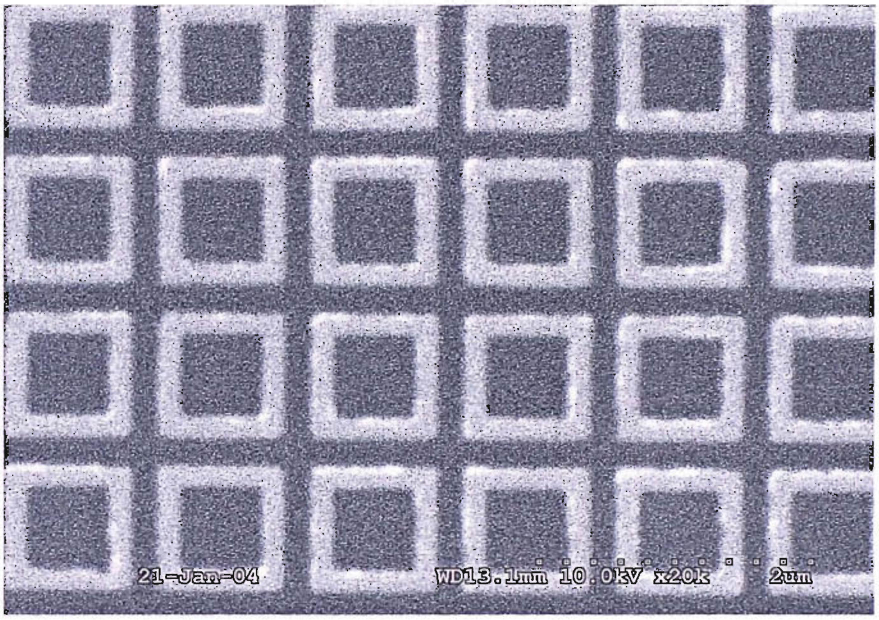

Fig. 5.11 Array of square-shaped 950 nm nano-rings with 75 nm separation. The thickness of the film is 20 nm and the width of sides is 150 nm.

Similar arrays of square-shaped nano-rings have been studied previously[13,14,15]. Using MOKE, MFM and OOMMF[11], authors have found that the magnetization reversal involves formation of intermediate metastable states (onion, vortex, horse shoe). In this paragraph we present studies of the azimuthal anisotropy of such arrays using magnetization reversal curves for various directions of the applied magnetic field.

Fig. 5.12 shows MOKE hysteresis loops for parallel and transverse components of magnetization for the magnetic field applied slightly off the edge of the ring (~5 degrees).

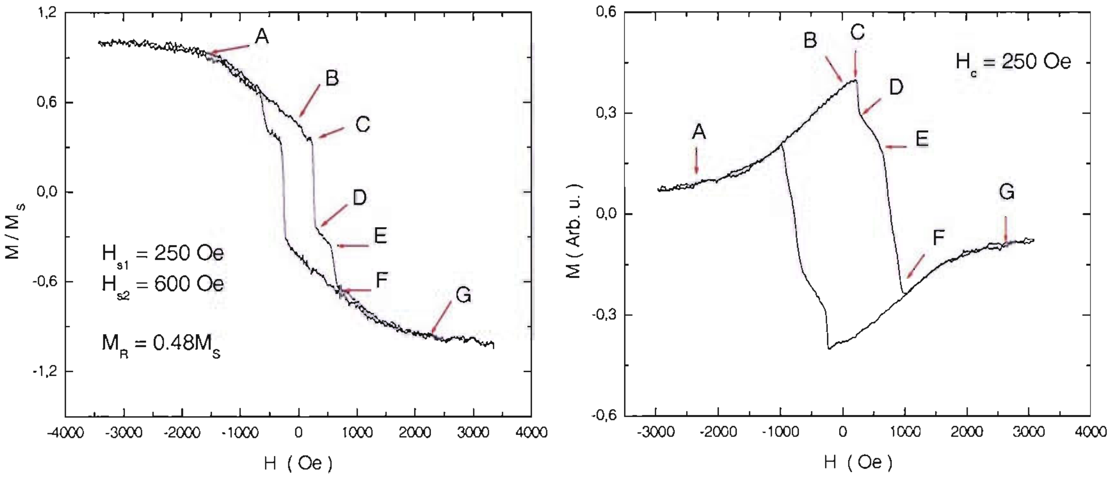

Fig. 5.12 Magnetization loops measured by longitudinal MOKE (a) and vector-MOKE techniques (b) showing components of the magnetization parallel and perpendicular to the magnetic field. The direction of the field was set along the edge of rings within 5 degrees.

The *M-H* curve in the left picture has characteristic two steps corresponding to switching fields: H_{s1}=250 Oe and H_{s2}=600 Oe. This feature means that during the reversal process the magnetization switches twice. Different letters mark characteristic regions of the loop, as discussed in the text. We can understand the reversal process in the Fig. 5.12a using the transverse component curve in Fig.5.12b and micromagnetic simulations. Simulations were made for one square ring with a cell size of 5 nm. Results are schematically shown in the Fig. 5.13. To account for an experimental error in alignment of the magnetic field we take its direction rotated clockwise by 5^0 from the Y-axis. The magnetization process in this case can be subdivided in two parts: one is related to easy axis magnetization of two sides of the ring nearly parallel to the magnetic field and the second is the hard axis magnetization of the remaining two sides perpendicular to the field. In the saturated state (Fig. 5.13.1) all magnetic moments are aligned with the field. As the magnetic field is reduced, the magnetization of ring sides perpendicular to the field starts to tilt under the action of the demagnetizing field, while in the two other parts of the ring, which have a small demagnetizing factor in the direction of the field, the magnetic moments retain their directions. This process corresponds to roughly linear parts *AB* in both graphs on Fig. 5.12. In the remanent state magnetic moments are lying along the sides due to the shape anisotropy. At two opposite corners the magnetization is changing gradually by 90^0. At the other two diagonal corners we have two transverse domain walls (Fig. 5.13.2). This state is called in the literature the onion state[8,9]. Such a configuration of the magnetization should give for the remanent magnetization a value of $0.5M_s$. The remanent state is marked by *B* on graphs in the Fig. 5.12

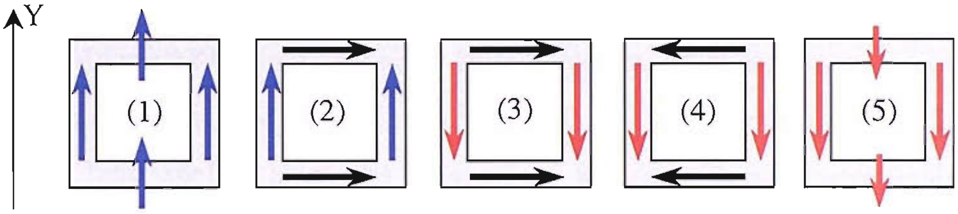

Fig. 5.13 A schematic representation of results from micromagnetic calculations for the magnetic field applied along the edge of the ring with 5 degrees offset clockwise from Y-direction.

The experimental value for the M_r taken from the graph is $0.48M_s$, which is close to the theoretical one. Taking into account the square geometry of our rings we can estimate the value of M_r for various azimuthal directions of the magnetic field by the equation:

$$M_r = \frac{M_s}{2}(\cos\varphi + \sin\varphi) \tag{5.11}$$

Where φ is the azimuthal angle. This formula gives $0.5M_s$ for the field applied along the edge, consistent with experimental and calculated values. For negative fields the hard axis magnetization continues in sides perpendicular to the field when the magnetization rotates now against the demagnetizing field: parts *BC* on the graphs. At the first switching field corresponding to the H_{s1} transverse domains start moving and the magnetization switches in sides parallel to the field. This corresponds to the branch *CD* of the magnetization loop. The resulting state is an intermediate onion state (Fig. 5.13.3). Because the field is applied slightly off the edge of the ring we observe small switching in the transverse magnetization curve as well: *CD* on the right graph. There is also a second switching field H_{s2} when the magnetization switches in sides perpendicular to the field resulting in the reversed onion state (Fig. 5.13.4). On the graphs in Fig. 5.12 this process corresponds to EF. Magnetization loops in this case again show that switching mainly affects magnetic moments lying in the sides along the x-direction. The remaining parts FG are associated with the hard axis magnetization and subsequent saturation (Fig. 5.13.5). Magnetization loops obtained from numerical calculations are presented in Fig. 5.14 giving a remanence of $0.5M_s$ and H_{s1} = 260 Oe. We have also measured *M-H* loops with the field applied along the diagonal of the ring. Results were analyzed using OOMMF micromagnetic simulations[16]. Fig. 5.15 shows measured and computed hysteresis loops for the case of diagonal magnetization process.

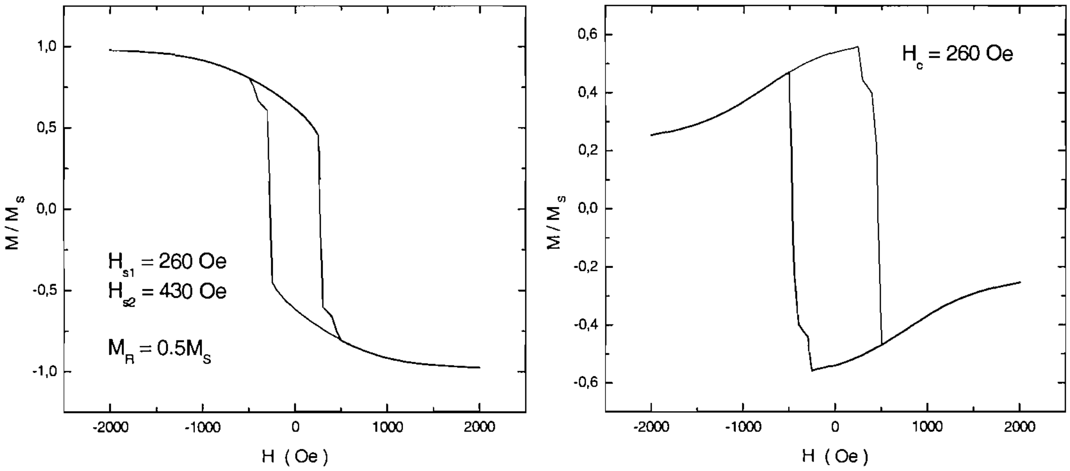

Fig. 5.14 Calculated M-H loops using OOMMF code, showing results for $\mathbf{M}_{||}$ *and* $\mathbf{M}_{\perp}$ *components of the magnetization.*

Coercive field and remanence have been increased in comparison with the previous magnetic field direction along the edge. The value $M_r = 0.67$ is in a good agreement with the computed values (OOMMF) and found by formula (5.11), which gives: $M_r = M_s/\sqrt{2}$. The saturated state can be modeled as shown in Fig. 5.16.1 with all magnetization along the applied field. When the field is decreased, the magnetic moments in all sides of the ring turn to their minimal energetic state under action of magnetostatic effects. This process resultes in an onion state at remanence (Fig. 5.16.2), which is similar to that appearing in the previous discussion. The transition to a reversed onion state shown in Fig. 5.16.4 occurs through the formation of a vortex (Fig. 5.16.3) with zero overall magnetization in the direction of the applied field. Processes 3 and 4 in Fig. 5.16 take place at a magnetic field corresponding to the coercive field. The vortex state is not seen on the *M-H* curve, however this state was found using our micromagnetic simulations. Recent results of MFM measurements also revealed that the vortex state is possible in these structures during the 45^0 reversal process[14].

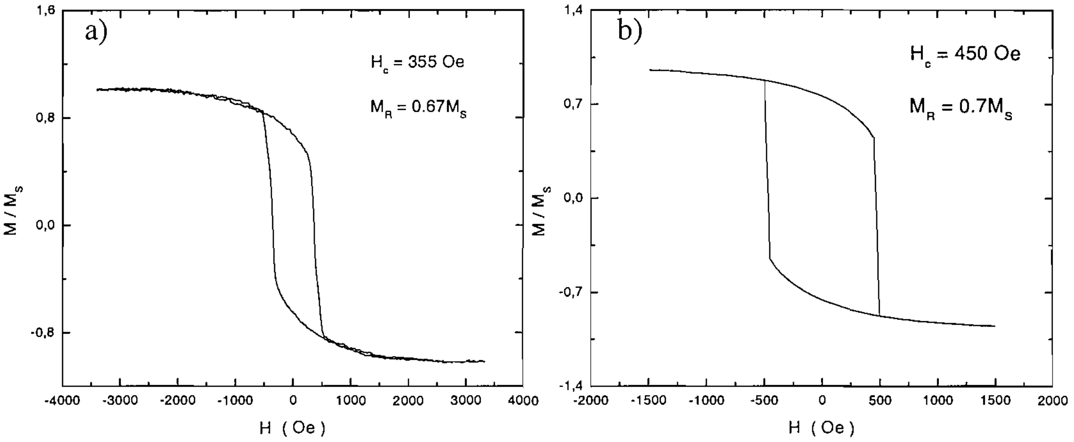

Fig. 5.15 Measured (a) and calculated (b) hysteresis loops for the square ring with the magnetic field applied along the diagonal. The shape of the curves and values of M_R are in a good agreement.

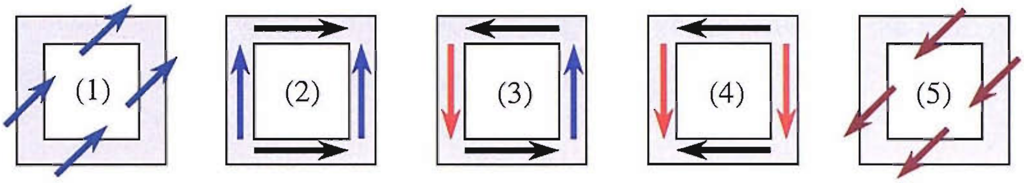

Fig. 5.16 Results of simulations schematically shown as colored arrows for the magnetic field applied along the 45 degrees angle direction. Reversal process involves formation of a vortex (3) in addition to two onion states (2) and (4).

As can be seen from the figure, state 4 should result in $-0.7M_s$ magnetization symmetrical to $+0.7M_s$ for state number 2. After the switching is complete the magnetization is saturated to its saturation value (Fig. 5.16.5). An interesting feature in the behaviour of these structures is that the second switching field, corresponding to switching in the sides of the ring along the x-direction (in our notation from Fig. 5.13) is not present in the M-H loop for the 45 degrees magnetization. This is because along the 45^0 direction all four sides have equal demagnetizing factors. Now we do not have separation for easy and hard axis switching processes and reversal from one onion state to the reversed one is taken place at one field.

Results of measurements for various directions of the magnetic field are shown in Fig. 5.17 where we plotted the first switching field H_{s1} versus azimuthal angle of the field direction in the plane of the film. This data along with the data for the remanent magnetization suggests that an easy axis is present in the rings and its direction coincides with the diagonal. We were unable to study angular dependence of the second switching field due to the difficulties in detecting it with our technique. Taking into account previous results on magnetization reversal in the rings we conclude that this second switching field should have a maximum for the case when the magnetic field is applied along the edge of the ring and decrease with the azimuthal angle because the second switching will be less affected by the hard demagnetization. We can try to describe the data in Fig. 5.17 by taking into account geometrical shape effects in the ring. As found above the remanent state in all cases is the onion state.

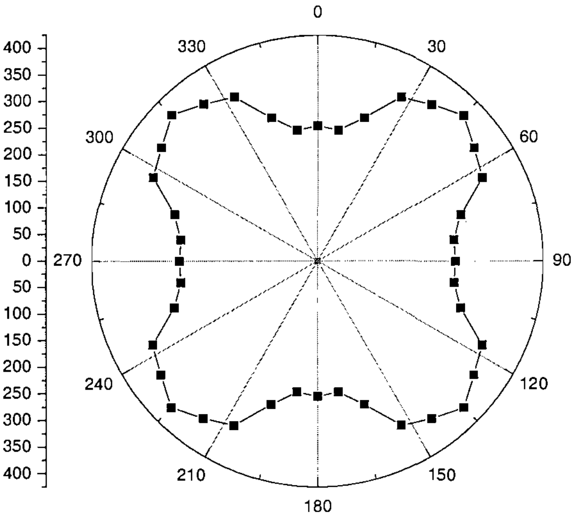

Fig. 5.17 A polar plot of the coercive field in magnetic rings versus azimuthal direction of the magnetic field. Results obtained for the coercivity presented here show existence of four easy magnetization axes along the diagonals of rings.

Our further analysis is based on the results of micromagnetic computation. We apply the field at various angles φ from the y-direction. The switching field H_{s1} is defined by switching in the sides, which are parallel to the Y-axis. The projection of the field acting on the magnetization is equal to $H_y = H_{appl}\cos(\varphi)$. This value decreases when φ changes from zero to 45 degrees. Hence the onion state formed in remanance will remain unswitched up to higher fields for increasing angles. After 45 degrees the situation changes due to the 90^0 symmetry and further increase of the angle corresponds to its decrease in other symmetric reversal with the field turned at 90 degrees, leading to the growth of the field projection and reduction of H_{s1}. A rough prediction for the anisotropy strength $K = \frac{H_{c1}^{\max}}{H_{c1}^{\min}}$ using this idea, gives a value $K = \sqrt{2}$. Taking the ratio of the measured coercivities for the easy and hard directions from Fig. 5.12 and Fig. 5.15, we get K = 1.42. Results of micromagnetic calculations give K = 1.78. This discrepancy may be caused by the relatively large field step of ~100 Oe in simulations. In addition the magnetostatic energy does not obey a cosine law, which we used in our discussion.

Another possibility to study this anisotropy is to measure the saturation fields for various azimuthal angles. Shape anisotropy suggests that the ring is harder to saturate along the edge because half of the sample is in the hard direction. These studies can be done in future work together with more detailed investigation of the anisotropy of the second switching field anisotropy. Another important phenomenon, which we did not take into account analyzing our data, is the dipolar coupling between rings. This requires more detailed experimental and theoretical investigation in the future.

In conclusion we have studied the in-plane anisotropy of the magnetic properties in a two-dimensional array of square nano-rings. The shape of the rings affects the magnetization process significantly leading to a four-fold anisotropy of the first switching field. Using micromagnetic simulations and simple geometric considerations we gave simple descriptions of the anisotropic behaviour of the switching.

5.5 Magnetic and transport properties of a square array of nano-rings

In this section we present experimental studies of magnetic and magneto-resistive properties of a square array of nano-rings. Before presenting experimental results we discuss theoretical concepts for magneto-resistance in magnetic 3*d* metals.

5.5.1 Mechanisms of electrical resistance in transition metals

Electrical resistance in metals is from the scattering of valence electrons in *s* and *p* bands that are weakly bonded in atoms and move inside the crystals relatively free. The dissipation mechanisms involve scattering of electrons at impurities and by phonons. In transition metals, electrons from localized *d*-states participate in conduction, connecting magnetism and electric transport.

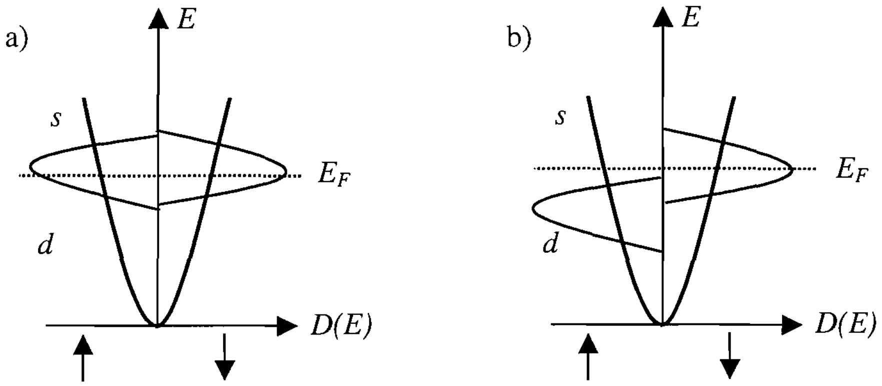

Fig.5.18 Band structures of (a) non-ferromagnetic transition metals and (b) ferromagnetic transition metals. Up and down arrows indicate majority and minority spin states.

To describe how these localized *d*-states can affect transport properties one should look at the band structures of transition metals. Fig. 5.18 shows a schematic representation of band structures for non-magnetic and magnetic 3*d* metals. In this figure the density of states is presented for *s*-electrons that have a free electron-like band structure and for d-electrons - more localized in atoms. The main difference between 3*d* metals and alkali and noble ones is that the Fermi level intersects *d* states. This structure allows the overlap of *s* and *d* states at the Fermi level, which leads to *s*-*d* hybridization. The hybridization significantly affects scattering processes in metals and changes transport properties due to the following reasons. First of all the mixing of *s* and *d* states causes an increase in the effective mass of conducting electrons because they become slightly localized. This gain in effective mass reduces the mobility of *s*-electrons leading to a larger resistivity. The crucial result of the hybridization is that the *s*-electrons now can be scattered by localized *d* states. Changes in scattering will affect the relaxation time (τ), so we can write[6]:

$$\frac{1}{\tau} = \left|V_{scat}\right|^2 N(E_F) \tag{5.12}$$

Where V_{scat} and $N(E_F)$ are the scattering potential and the density of states at the Fermi level respectively. From this we can conclude that the resistance in 3*d* metals increases due to the large density of states at the Fermi level, which is the result of overlapping of *s* and *d* states.

Electric transport properties in 3*d* metals well below T_c can be described by the two current model introduced by Mott[6]. In this model charge carriers with spin up and spin down states are moving through a circuit as shown in Fig. 5.19. Spin up and spin down *s*-electrons can be scattered into majority and minority *d* bands respectively. So this model suggest that in transition metals there are two resistivity channels one is the spin up channel and the second is the spin down channel. In each channel the resistivity is due to spin disorder, scattering in impurities and *s*-*d* scattering. Spin up and spin down resistivities are defined as $\rho^{\uparrow}$ and $\rho^{\downarrow}$. Using the formula for the resistance of parallel circuit one can write for the total resistance:

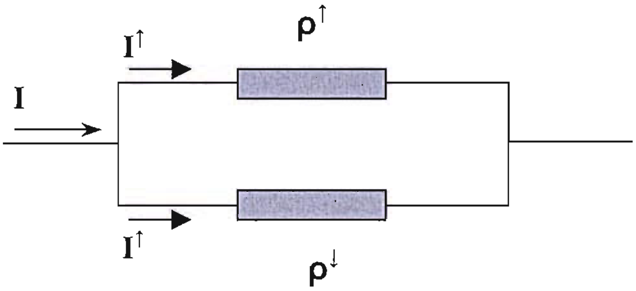

Fig. 5.19 Mott two current model of transition metals – equivalent circuit. Up and down arrows indicate spin up and spin down channels.

$$\rho = \frac{\rho^{\uparrow}\rho^{\downarrow}}{\rho^{\uparrow} + \rho^{\downarrow}} \tag{5.13}$$

Often the ratio of spin-down to spin up resistivities is defined as the asymmetry parameter: $\alpha = \rho^{\downarrow}/\rho^{\uparrow}$. This parameter is very large for Ni because it has a fully occupied majority spin band and the resistance is caused by scattering in the minority spin bands. Also the resistance in 3*d* materials depends on magnetic order. In an ordered ferromagnetic state the scattering of free charges is smaller than in a spin disordered state like the paramagnetic state. The spin disorder resistivity is given by the equation[6]:

$$\rho_{ferro} = \rho_{para}\left[1-\left(\frac{M_s(T)}{M_s(0)}\right)^2\right] \tag{5.14}$$

Another way for the resistance to increase at elevated temperatures is a spin flip process due to the creation and annihilation of magnons, which leads to mixing of spin up and spin down channels. At higher temperatures the formula (5.13) is modified giving[6]:

$$\rho = \frac{\rho^{\uparrow}\rho^{\downarrow} + \rho^{\uparrow\downarrow}(\rho^{\uparrow} + \rho^{\downarrow})}{\rho^{\uparrow} + \rho^{\downarrow} + 4\rho^{\uparrow\downarrow}} \tag{5.15}$$

Here, $\rho^{\uparrow\downarrow}$ is the spin mixing resistivity when a spin-up conduction electron is scattered to a spin down state.

To summarize this paragraph we can write that transport properties in transition metals are affected by hybridization of *s* and *d* states. This increases the density of states at the Fermi level leading to enhancement in the scattering of charge carriers. Resistance in transition metals can be described by the Mott two current model.

5.5.2 Anisotropic magnetoresistance (AMR) in ferromagnetic transition metals

Until now we considered electric transport properties in 3*d* metals in the absence of a magnetic field. The next step will be to find out how the magnetic field can affect the resistance properties. In non-magnetic materials the action of the magnetic field on electric current is described by the ordinary Hall effect[6]. The component of the magnetic field perpendicular to the current density induces an electric field transverse to the current:

$$\mathbf{E}_H = R_H[\mathbf{J} \times \mu_0 \mathbf{H}] \tag{5.16}$$

Here, R_H is the Hall constant describing the strength of the effect. From Ohm's law we can define the Hall resistivity as:

$$\rho_H = \frac{\mathbf{E}_H}{\mathbf{J}} \tag{5.17}$$

In addition to the Hall resistivity this effect changes the resistance of metals as well. Under the action of the Lorentz force, charge carriers undergo cyclotron orbits leading to a decrease of the mean free path in the direction of the applied voltage. Magnetoresistance due to the Hall effect was described by Kohler and its dependence on the applied magnetic field is known as Kohler's rule[6]:

$$\frac{\Delta\rho}{\rho} \sim \left(\frac{H}{\rho}\right)^2 \tag{5.18}$$

In ferromagnetic materials the ordinary Hall effect is accompanied by the spontaneous Hall effect, which has much stronger strength. This is due to enhancement of the magnetic field inside the ferromagnetic body. Expressions for the spontaneous Hall effect are obtained from formulae for the ordinary effect by substituting the external field **H** by a spontaneous magnetization **M**. Thus the Hall resistivity will consist of two parts in ferromagnetic metals: $\rho_H = \rho_{0H} + \rho_{sH}$. Similar, to the Hall resistivity, the magnetoresistance in ferromagnetics can be divided into two parts one for the ordinary magnetoresistance and another for spontaneous magnetoresistance. Hence Kohler's rule in the ferromagnetic case can by written as[6]:

$$\frac{\Delta\rho}{\rho} \sim a\left(\frac{H}{\rho}\right)^2 + b\left(\frac{M}{\rho}\right)^2 \qquad (5.19)$$

The anisotropic magnetoresistance in a ferromagnetics metal is caused by a difference in electrical resistances when the magnetization is parallel to the electric current (usually defined as ($\rho_{\parallel}$) or transverse to it ($\rho_{\perp}$). This effect can be easily observed in ferromagnetic sample with uniaxial anisotropy. If the electrical current is applied along the easy axis in a magnetic material then the magnetoresistance $\rho_{\parallel}$ measured in the easy direction remains unchanged if the magnetic field is applied along this direction except at the switching field. In contrast, the resistivity $\rho_{\perp}$, for the magnetic field applied in the hard direction i.e. transverse to the current, changes its value with the field quadratically. When the magnetic field reaches the value of the anisotropy field, $\rho_{\perp}$ saturates and remain unaffected by the field. So, the AMR effect can be used as a measure of the anisotropy field in ferromagnetics. Experimental data for the AMR effect in transition metals and alloys show that the magnetoresistance in the case when magnetization is along the current is bigger then for the transverse orientation. Hence, the magnetoresistive ratio: $\Delta\rho = (\rho_{\parallel} - \rho_{\perp})/\rho_0$ is positive. This behaviour cannot be explained using the Hall effect formalism. The magnetoresistance caused by the Hall effect should give rise to the $\rho_\perp$ due to Lorentz force, which makes electrons move in the cyclotron orbits and hence decreases the mean free path. This does not agree with experimental data. In order to understand the mechanism of AMR we should look at the scattering of charge carriers into *d* states. It was found that magnetoresistive effects are controlled by the spin-orbit (S-O) interaction $\mathbf{L}\cdot\mathbf{S}$. Consider the case of a transition metal with $\alpha >> 1$. In the absence of the S-O interaction the scattering through the minority *d* band is dominant and the resistance can be written, using the Mott two-current model:

$$\rho = \frac{\rho_s\left(\rho_s + \rho_{sd}^{\downarrow}\right)}{2\rho_s + \rho_{sd}^{\downarrow}} \tag{5.20}$$

Now if we take into account the spin-orbital interaction, scattering is enhanced. The reason for this enhancement is that S-O interaction is mixing spin up and spin down states. This effect allows such transitions such as $3d^{\uparrow}(m_l) \rightarrow 3d^{\downarrow}(m_{l+1})$ or $3d^{\downarrow}(m_l) \rightarrow 3d^{\uparrow}(m_{l-1})$. Thus due to the S-O interaction $s^{\uparrow}$ electrons can be scattered into the $3d^{\downarrow}$ hole states (spin flip process). In addition, $d^{\uparrow} \rightarrow s^{\downarrow}$ processes open $3d^{\uparrow}$ holes increasing scattering of $s^{\uparrow}$ electrons. After the role of the S-O interaction in the scattering process has been determined the next task is to find out why the resistance is larger when $\mathbf{J} \parallel \mathbf{M}$. To do this we can refer to the structure and shape of d orbitals. It is known that an electron can be scattered by the *d* hole if the wave vector **k** of the *s* electron lies in the plane of the classical orbit. Taking this fact into account it can be shown that when the current is parallel to the magnetization there are more empty *d* orbitals satisfying the condition for scattering[6]. If we define V_{scatt} as a potential for $s^{\uparrow} \rightarrow d^{\downarrow}$ scattering and θ as the angle between **J** and **M** then the resistance can be written as: $\rho_{sd}^{\uparrow} = \left|V_{scatt}\right|^2 \cos^2\theta$. The angular dependence is quadratic because it works in the same way for **M** parallel and anti-parallel to **J**. The potential V_{scatt} is dependent on Coulomb, spin-orbit and exchange interactions. We can write equation for the anisotropic magnetoresistance using the Mott two current model[6]:

$$\rho = \frac{\left(\rho_s + \rho_{sd}^{\uparrow}\right)\left(\rho_s + \rho_{sd}^{\downarrow}\right)}{2\rho_s + \rho_{sd}^{\uparrow} + \rho_{sd}^{\downarrow}} = \frac{\left(\rho_s + \left|V_{scatt}\right|^2 \cos^2\theta\right)\left(\rho_s + \rho_{sd}^{\downarrow}\right)}{2\rho_s + \rho_{sd}^{\downarrow} + \left|V_{scatt}\right|^2 \cos^2\theta} \qquad (5.21)$$

This formula gives a reasonable description of the AMR behaviour in ferromagnetic materials.

In this section we have reviewed electric transport properties in transition ferromagnetic metals in the presence of a magnetic field. It has been shown that the AMR effect is due to the spin-orbit interaction, which leads to anisotropic $s^{\uparrow} \rightarrow d^{\downarrow}$ scattering. We will use this knowledge in studying MR properties of lithographically prepared nano-rings in the next section.

5.5.3 Coercivity of periodic square array of permalloy rings

In this work we have studied the dependence of the coercive field on the azimuthal direction of the magnetic field in a periodic square array of interconnected nano-rings with outer and inner diameters 1 and 0.6 micrometer respectively (Fig. 5.20a). Results of this experiment are shown in Fig. 5.20b. As follows from experimental data the coercive field has a clear minimum when the magnetic field is directed along a diagonal of the array. Since a circular shape cannot give rise to azimuthal anisotropy, the source of this anisotropy must be coupling between the rings in the array. Indeed since rings are connected the exchange interaction in touching regions is strong and can affect the magnetization reversal process significantly. Taking into account the common switching

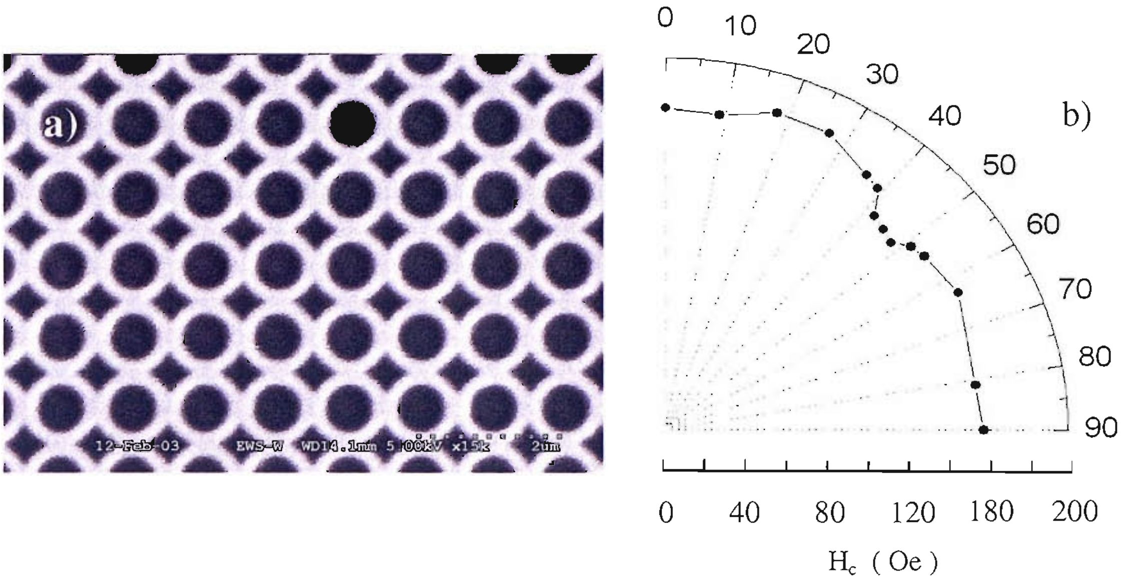

Fig. 5.20 SEM picture of 20 nm thick permalloy film with nano-rings (a) and coercivity of this array versus azimuthal direction of the applied magnetic field (b). The Zero degree point corresponds to the magnetic field along an edge of a square lattice.

process in nano-rings (onion-vortex-reverse onion)[17] we can try to understand this anisotropic effect. The onion to vortex transition is a wall depinning and propagation process[17,18]. Hence, the depinning or switching field from onion to vortex state is strongly dependent on the pinning strength.

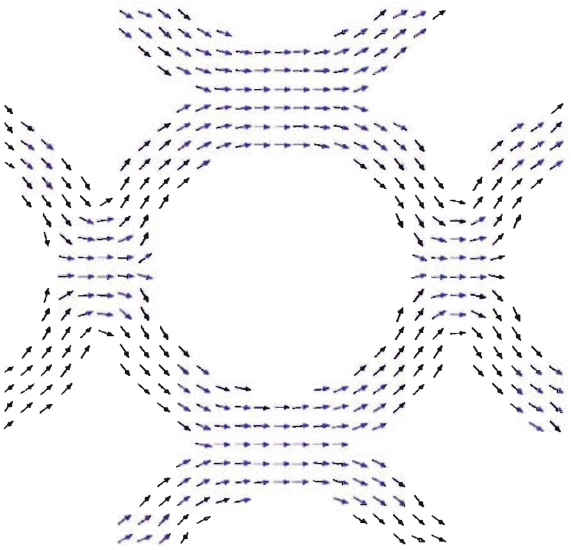

Fig. 5.21 Onion state in the array of connected rings for the field directed along the edge of the lattice.

In Fig. 5.21 we present the onion state during the reversal process obtained by 2D micromagnetic simulations for the magnetic field applied along the edge of the lattice. Regions where rings are touching can be treated as pinning centres for the transverse domain walls. As we show later the vortex state is not formed in our sample, since rings are connected. Nevertheless, there is still the "onion - reversed onion" process, and the pinning shifts the transition to higher fields giving an increase in the coercivity.

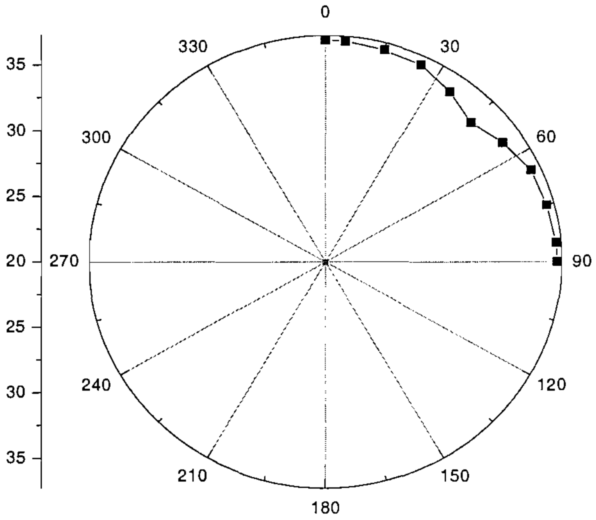

Fig. 5.22

Results of micromagnetic simulations for the azimuthal anisotropy of the coercive field in the array of connected rings. The zero degrees direction corresponds to the magnetic field along the edge of the lattice.

Results of micromagnetic simulations for the anisotropy of the coercive fields (Fig. 5.22) support the experiment, giving a minimum when the magnetic field applied along the diagonal of the lattice.

5.5.4 Magnetoresistance of a square array of nano-rings

It has been suggested that nano-ring structures are candidates for application in magnetic random access memory (MRAM)[19]. Application of nano-rings in MRAM cells requires understanding of the magnetization reversal in these structures and how this affects the resistance. Recently, the influence on the magnetoresistance of metastable magnetic states during reversal in a single ring has been studied in detail[20]. It was found that the resistance is strongly affected by the presence of transverse domain walls leading to a sharp increase in magnetoresistance when a vortex configuration is formed during reversal. This behaviour is explained by the AMR effect since the magnetization in the vortex state and the current have the same orientation. More detailed investigation of the influence of transverse domain walls on the magnetoresistance in nano-rings are presented in Ref. 21.

In this section we present an experimental study of transport properties in a square array of nano-rings. The major difference from previous studies is that rings in the array touch, allowing us to study electrical transport in the array. We investigated a sample with a square shape. Fig. 5.23 shows a schematic picture of the studied sample with four contacts and eight gold wires. This configuration allowed us to measure the resistance in two orthogonal directions "A" and "B". Using a rotational stage with high angular resolution, the magnetoresistance of the sample was measured for various directions of the magnetic field with respect to the sample plane.

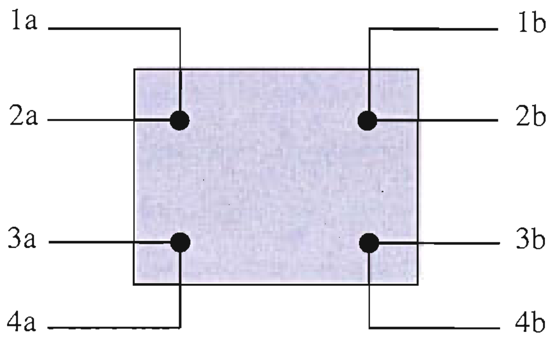

Contacts assignment:
1a-1b – Current "B"
4a-4b – Voltage "B"
2a-3a – Current "A"
2b-3b – Voltage "A"

Fig. 5.23 A contact circuit as it used in the experiment. There are two twisted pairs of wires for electric current and two for measuring a voltage drops.

Fig. 5.24 shows two configurations used in the experiment. In configuration "A" (Fig. 5.24a) the current is applied using the 2a-3a pair and the resistance measured using the 2b-3b pair. As follows from the scheme, the electric current and the in-plane component of the magnetic field are collinear.

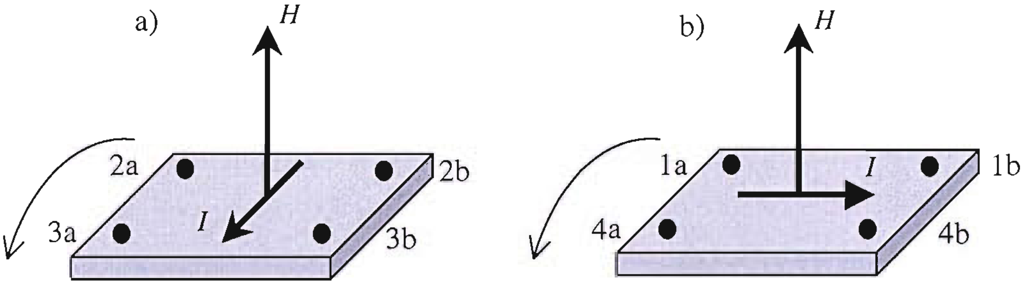

Fig. 5.24 Two configurations, "A" and "B" used in the experiment. Thin black arrows show the direction of rotation. Angles between the electric current and in-plane component of the magnetic field are 0 and 90 degrees respectively.

In configuration " B" the direction of the electric current is perpendicular to the in-plane component of the magnetic field (Fig. 5.24b).

Experimental results of resistance measurements at 10 K using configurations "A" and "B" are shown in Fig. 5.25 for the transverse magnetic field. These curves show characteristic H-squared behaviour with sharp peaks in the 500 mT region. As can be seen from the figure the direction of the peaks is negative for configuration A and positive for B. This implies that the sign of the effect strongly depends on the relative orientation of the electric current and the in-plane component of the magnetic field. The gradual H^2 increase in the resistance when the magnetic field is being reduced from its saturation value comes from the AMR effect, since the electric current is in the film plane. Using a rotational stage with high angular resolution, the magnetoresistive curves have been measured for various directions of the magnetic field with respect to the sample plane. The resistive peaks emerge at small fields when the

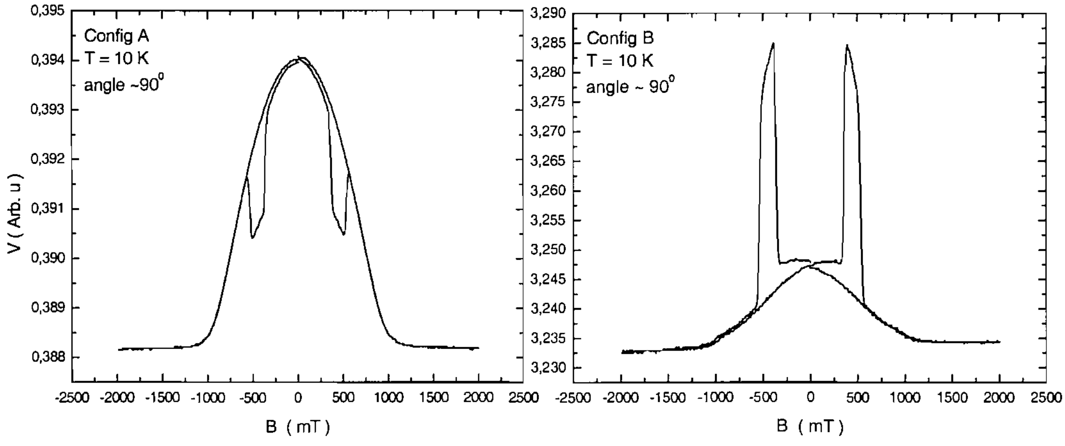

Fig. 5.25 Magnetoresistance of the sample in configurations A and B for the magnetic field applied perpendicular to the film plane.

applied field is rotated away from the perpendicular direction. The angular dependence of the peak position is shown in Fig. 5.26 where θ is the angle between the magnetic field and the film plane.

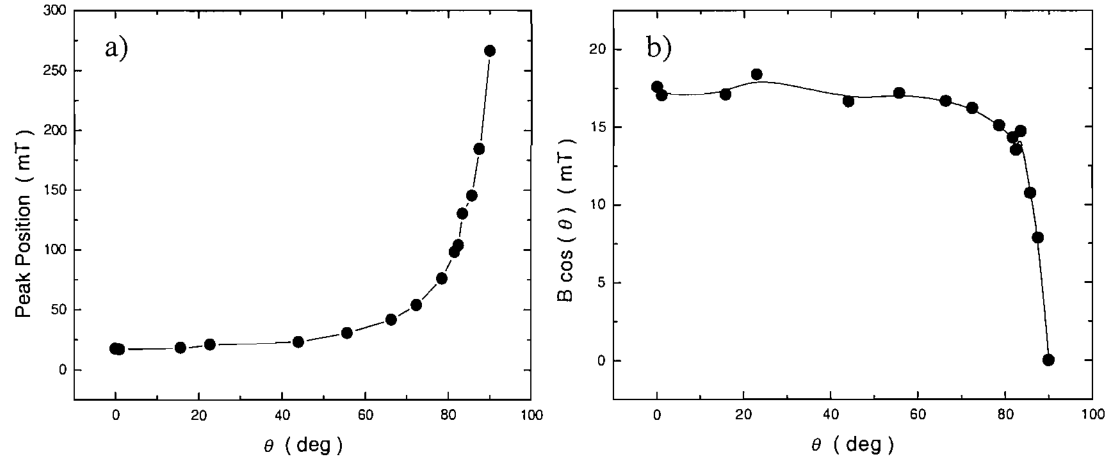

Fig. 5.26 Positions of peaks versus angular direction of the applied magnetic field (a) and angular dependence of in-plane components of peak fields. (zero angle corresponds for the in-plane magnetic field)

This behaviour of the resistance implies that the in-plane component of the applied field is important for peaks. Fig. 5.26b shows that peaks mostly appear when the in-plane magnetic field is ~150-170 Oe. Taking into account results from previous studies of magnetoresistance in nano-rings we conclude that these peaks might be related to an onion to a reversed onion transition in rings[20,21]. Our further discussion is based on the assumption that the in-plane component of the magnetic field plays a vital role. In Fig. 5.27 we show a transition from an onion state to a reversed onion state obtained from micromagnetic simulations. The magnetic field is applied along the x-direction. The sample was initially magnetized in the positive direction and then the magnetic field was reduced to zero. The remanent onion state is shown in Fig. 5.27a. At negative fields the onion state transforms to the reversed onion state through an intermediate state (Fig. 5.27b). These results suggest that the reversal process takes place without formation of a vortex in contrast to the common reversal process in a single ring[22].

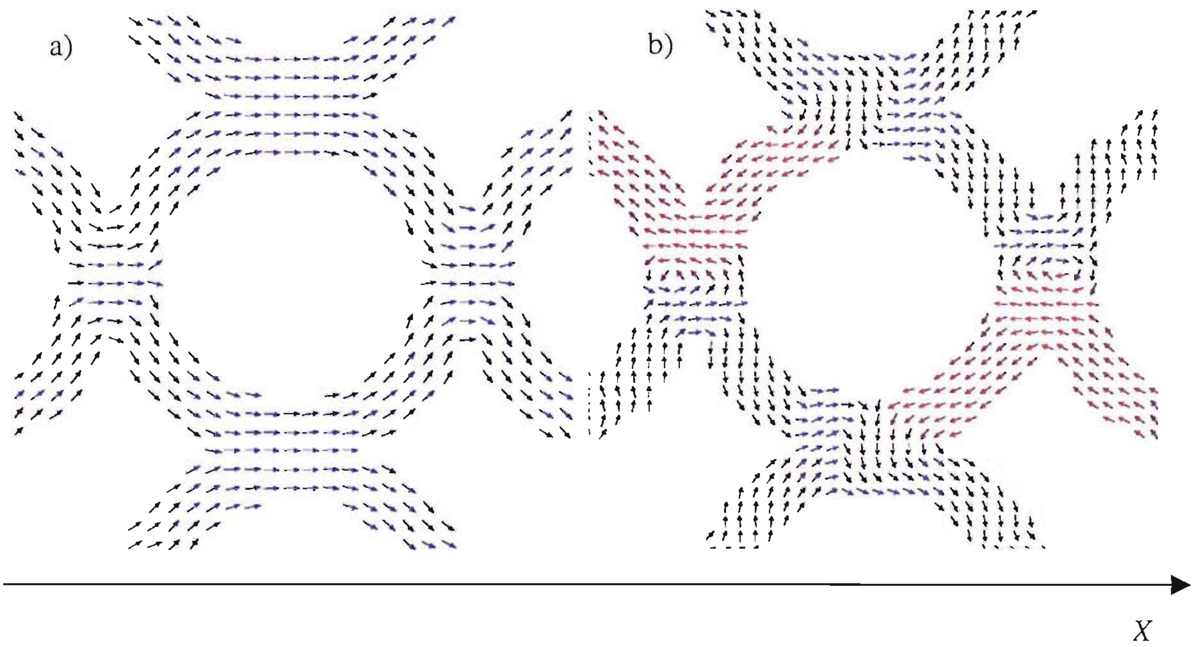

Fig. 5.25 The remanent onion state(a) and a transition from the onion to the reversed onion state (b) in connected rings obtained from micromagnetic simulations.

We can try to give a qualitative description of the observed behaviour of the magnetoresistance. Let us assume that the electric current is applied along the x-direction i.e. parallel to the magnetic field. The transition from the onion to the reversed onion state should decrease the resistance because less magnetization has direction parallel to the current (see Fig. 5.27). If the electric current is perpendicular to the applied field then from comparison of Fig. 5.27a and Fig. 5.27b one can conclude that resistance should increase since there is more magnetization, which is parallel to the current in touching regions. This qualitative picture is not full because it does not explain a size variation of the resistive peaks. We conclude that due to the complexity of the reversal mechanism in connected rings and the high sensitivity of the resistive peaks to the magnetic field and current directions it is hard to give a full and rigorous explanation at the current stage of research

5.6 References.

---

[1] J. Raabe et al, J. Appl. Phys. 88, 4437 (2000)

[2] R.P. Cowburn J. Phys. D: Appl. Phys. 33, R1-R16 (2000)

[3] M. Schneider J. Mag. Mag. Mat. 257, 1 (2003)

[4] T. Pokhil J. Appl. Phys. 87, 6319 (2000)

[5] T. Shinjo Science 289, 930 (2000)

[6] R.C. O'Handley, *Modern Magnetic Materials*, Wiley Interscience, New York, 1999

[7] E.C. Stoner and E.P. Wohlfarth, Phil. Trans. **A240**, 599 (1948)

[8] A. Aharoni, J. Phys.: Condens. Matter **9,** 10009 (1997)

[9] E.H. Frei, S. Shtrikman, and D. Treves, Phys. Rev. **106**, 446 (1957)

[10] I. Guedes et al. Phys. Rev. B **66**, 014434-1 (2002)

[11] I. Guedes et al. Phys. Rev. B **62**, 11719 (2000)

[12] C. T. Yu et al., J. Appl. Phys. **87**, 6322 (2000)

[13] X. Zhu, P. Grutter, V. Metlushko and B. Llic, J. Appl. Phys. **93**, 7059 (2003)

[14] P. Vavassori, M. Grimsditch, V. Novosad, V. Metlushko, and B. Ilic, Phys. Rev. B, **67**, 134429 (2003)

[15] P. Vavassori et al., J. Appl. Phys. **93**, 7900 (2003)

[16] OOMMF Ver. 1.0; M.J. Donahue and D.G. Porter, http://math.nist.gov/oommf.

[17] J. Rothman et al., Phys. Rev. Lett. **86**, 1098 (2001)

[18] M. Klaui et al., Appl. Phys. Lett. **81**, 108 (2002)

[19] J. G. Zhu, and Y. Zheng, and G.A. Prinz, J. Appl. Phys. **87**, 6668 (2000)

[20] Mei-Feng Lai et al., Phys. Rev. B, **67**, 104419 (2003)

[21] M. Klaui et al., J. Appl. Phys. **93**, 7885 (2003)

[22] S.P.Li, D. Peyrade et al., Phys. Rev. Let. **86**, 1102 (2001)

Chapter 6. Conclusion

In this thesis we have presented a detailed experimental investigation of the magnetization reversal processes in nano-structured magnetic materials fabricated using both "bottom-up" and "top-down" techniques. Investigations have been performed using various types of magnetometry (VSM, SQUID, MOKE) and have been accompanied by micromagnetic simulations. Results obtained in this work provided significant new insight into the magnetic reversal mechanisms in 3D self-assembled nanostructures and lithographically prepared nano-elements. We summarize these findings below.

6.1 Properties of magnetic nanostructures prepared using self-assembly method

In Chapter 4 we have presented studies of magnetic nanostructures prepared using electrodeposition through templates from polystyrene latex spheres. This method allowed us to fabricate three-dimensional dot and anti-dot arrays with various periods depending on the sphere sizes used in templates. The film thickness can be easily controlled by the amount of charge during electrodeposition. Resulting macro-porous films have a homogeneous composition of magnetic material with excellent filling of the template voids, as evident from the EDSRX analysis. Studies of nano-structured films by scanning electron microscopy (SEM) showed their hexagonal structure with the size of ordered domains reaching up to 1 mm and an average concentration of defects in the anti-dot lattice of about 0.1%. In comparison with standard lithographic techniques this template deposition method has a significant advantage. It allows creating patterning in the direction transverse to the film plane, which is also well ordered.

The major outcome of our findings is that three-dimensional nature of nanostructures can significantly change the magnetization reversal behaviour. We found that the magnetic properties are strongly dependent on array parameters such as the period d and film thickness t_f. One of the most important parameters of ferromagnetic materials, the coercive field showed a strong dependence on these parameters. Indeed, the coercivity increased drastically in anti-dot structures compared to non-patterned films. In addition, studies of arrays with various hole sizes revealed that the coercivity has a characteristic maximum for the case when $d \approx \delta$, where δ is the domain wall width. It has been also found that in anti-dot arrays the coercive field shows a clear oscillatory dependence on the film thickness. This demonstrates that the reversal mechanism is strongly affected by the three-dimensional architecture. A quantitative description has been proposed using 2D and 3D models of domain wall pinning.

Investigations of the reversal process in quasi-spherical dots also revealed a significant difference in magnetic behaviour from 2D dot arrays. In particular it was found that reversal occurs through formation of two types of vortices: one with a core lying in the plain of the film and second with a transverse core direction. In dots with smaller diameters (less than 200 nm) the magnetization process can be realized either by a coherent rotation mode or by a vortex state depending on the direction of the magnetic field.

6.2 Properties of lithographically prepared nanostrucures.

Arrays studied in the second part of this work were fabricated by e-beam lithography. This technique is briefly described in Chapter 3. The samples investigated were arrays of nano-dots with elliptical shape, arrays of sub-micron holes in NiFe films, and nano-scale rings with square and circular shapes. Lithography allows fabricating nanostructures with excellent order. It makes this method very useful for basic physical research.

The reversal process and azimuthal anisotropy of the coercive field have been studied in elliptical dots using the MOKE magnetometer and OOMMF package. The reversal process in dots with long and short axes of 800 and 400 nm respectively can occur through the formation of an S-shaped domain state or a vortex state, dependent on the direction of the applied magnetic field. An attempt to explain the observed behaviour of azimuthal anisotropy using the Stoner-Wohlfarth model did not give satisfactory results since it assumes coherent rotation mode in nano-particles. This model only reproduces a general trend for the coercivity to decrease when the field is moved away from the easy (long) axis. Subsequent micromagnetic simulations reproduced the experimental data well.

The coercivity of 2D arrays of anti-dots demonstrated a four-fold azimuthal anisotropy, which can be related to the observed rhombic domain pattern (see Ref. 7 from Chapter 5). We investigated how the strength of this anisotropy changes with the size of holes. The dependence of the coercive field on the hole size have been investigated showing $\sqrt{r}$ dependence consistent with the 2D model.

We have also studied the in-plane anisotropy of the magnetic properties of a two-dimensional array of square nano-rings. The shape of the rings affects the magnetization process significantly leading to a four-fold anisotropy of the coercive field. The magnetization reversal process in these rings involves two magnetization switchings. This results in a step-like hysteresis with two switching fields – H_{s1} and H_{s2}. Azimuthal anisotropy has been studied for the field H_{s1}. Using micromagnetic simulations and simple geometrical considerations we have given qualitative explanations of the observed behaviour. Since rings in the array were positioned close to each other (separation distance 75 nm) the dipolar coupling is likely to play an important role in the magnetization process. This effect together with the azimuthal behaviour of the second switching field H_{s2} requires further experimental investigation in the future work.

Experimental investigations of transport properties in an array of circular interconnected nano-rings showed an interesting anomaly in resistance resulting in sharp peaks in magnetoresistive curves. The sign of the effect is positive or negative dependent on the relative direction of the in-plane component of magnetic field with respect to the electric current.

Appendix 1:

3D calculations of the domain wall pinning in anti-dots

```
/*********************************************************************
*******
Copyright (C) 2004 by Alexander
avg@linux
*********************************************************************
******/


#include <stdio.h>
#include <stdlib.h>
#include <math.h>
#include <string.h>

# define PI 3.1415926

# define CUB 0
# define FCC 1
# define HCP 2

typedef struct
{

  int tp; //type of the structure (CUB, FCC,....)
  double fi_x;
  double fi_y;
  double fi_z;

}
T_struct;


void InitStruct(T_struct* struc, int tp,double d)
//initializes the fi_.. values
// the type variable should be given
{
  struc->tp=tp;
  switch(tp)
  {
  case(CUB):
    {
      struc->fi_x=d;
      struc->fi_y=d;
      struc->fi_z=d;
      break;
    }
  case(FCC):
    {
      struc->fi_x=d;
      struc->fi_y=sqrt(3)*d/2;
      struc->fi_z=d*sqrt(2)/sqrt(3);
      break;
    }
  case(HCP):
```

```
      {
        struc->fi_x=d;
        struc->fi_y=sqrt(3)*d/2;
        struc->fi_z=d*sqrt(2)/sqrt(3);
        break;
      }
    }
}

double m_div(double x, double y)
{

  double n,ostatok;

  x=x/y;
  ostatok=modf(x,&n); //returns "ostatok" and the "celuyu" part of
number x
  return n;
}

void CoordCubic(int i, int j, int k, double Center[3], double d)
{
  double X;
  double Y;
  double Z;

  double x0=0, y0=0, z0=0;

  X = x0+i*d;
  Y = y0+j*d;
  Z = z0+k*d;

  Center[0]=X;
  Center[1]=Y;
  Center[2]=Z;

}

void CoordFCC(int i, int j, int k, double Center[3],double d)
{
  double X;
  double Y;
  double Z;

  double x0=0, y0=0, z0=0, fi, fi_z;

  fi=sqrt(3)*d/2;
  fi_z=d*sqrt(2)/sqrt(3);

  if (k%3==0 & j%2==0)
  {
    X=x0+i*d;
    Y=y0+j*fi;
    Z=z0+k*fi_z;
  }

  if (k%3==0 & j%2!=0)
  {
    X=x0+i*d+d/2;
    Y=y0+j*fi;
    Z=z0+k*fi_z;
```

```
  }
  if ((k-1)%3==0 & j%2==0)
  {
    X=x0+i*d+d/2;
    Y=y0+j*fi+fi/3;//fi/3
    Z=z0+k*fi_z;
  }
  if ((k-1)%3==0 & j%2!=0 )
  {
    X=x0+i*d;
    Y=y0+j*fi+fi/3;//fi/3
    Z=z0+k*fi_z;
  }

  if ((k+1)%3==0 & j%2==0)

  {
    X=x0+i*d;
    Y=y0+j*fi+2*fi/3;//fi/3
    Z=z0+k*fi_z;
  }

  if ((k+1)%3==0 & j%2!=0)

  {
    X=x0+i*d+i*d/2;
    Y=y0+j*fi+2*fi/3;//fi/3
    Z=z0+k*fi_z;
  }

  Center[0]=X;
  Center[1]=Y;
  Center[2]=Z;

}


void CoordHCP(int i, int j, int k, double Center[3], double d)
{

  double X;
  double Y;
  double Z;


  double x0=0, y0=0, z0=0, fi, fi_z;

  fi=sqrt(3)*d/2;
  fi_z=d*sqrt(2)/sqrt(3);

  if (k%2==0 & j%2==0)
  {
    X=x0+i*d;
    Y=y0+j*fi;
    Z=z0+k*fi_z;
  }

  if (k%2==0 & j%2!=0)
  {
    X=x0+i*d+d/2;
```

```
    Y=y0+j*fi;
    Z=z0+k*fi_z;

  }
  if (k%2!=0 & j%2==0)
  {
    X=x0+i*d+d/2;
    Y=y0+j*fi+fi/3;//fi/3
    Z=z0+k*fi_z;
  }
  if (k%2!=0 & j%2!=0 )
  {
    X=x0+i*d;
    Y=y0+j*fi+fi/3;//fi/3
    Z=z0+k*fi_z;
  }

  Center[0]=X;
  Center[1]=Y;
  Center[2]=Z;

}

double DWthickness(double h)
{
  double l_ex, w_0, t,max;
  double test;
  double w;
  l_ex =4e-3;
  w_0 = 215e-3;
  //t = 1;
  max = 0.;
  for (w=0;w<=w_0;w+=0.001e-3)
  {
    test = fabs(2*PI*PI*((l_ex*l_ex)/(w_0*w_0)-
(l_ex*l_ex)/(w*w))+2*w/(w+h)-(w*w)/((w+h)*(w+h))-0.);

    if (test < 0.0001)
      if (max<w)
        max = w;
    //      printf("thickness w= %f\n",max);
  }
  return max;
}

double DWarea(double h, int N_Y, double x, double d,T_struct* struc)
{

  int i, j, k;
  double S, Si, r, fi_z, shift;
  double Center[3];
  double DW;

  double fi,fi_x;
  double temp;


  fi_x=struc->fi_x;
  fi=struc->fi_y;
  fi_z=struc->fi_z;
```

```
S=0;
r=0;

temp=m_div(h-d/2,fi_z);

for (k=0; k<=m_div(h-d/2,fi_z)+1;k++)
  for (i=m_div(x,fi_x)-1; i<=m_div(x,fi_x)+1;i++)
  {
    for (j=0; j<N_Y; j++)
    {
      Si=0;
      shift = k*fi_z+d/2;

      switch(struc->tp)
      {
      case(CUB):
        {
          //printf("CUB y %f z %f\n",fi,fi_z);
          CoordCubic(i,j,k,Center,d);
          break;
        }
      case(FCC):
        {
          //printf("FCC y %f z %f\n",fi,fi_z);
          CoordFCC(i,j,k,Center,d);
          break;
        }
      case(HCP):
        {
          //printf("HCP y %f z %f\n",fi,fi_z);
          CoordHCP(i,j,k,Center,d);
          break;
        }
      }

      if ( fabs(x-Center[0])<(d/2) )
      {
        r=sqrt((d*d/4)-(x-Center[0])*(x-Center[0]));

        if(r<=(h-shift))
          Si=PI*r*r;

        else
        {
          if ( r>fabs(h-shift) )
          {
            if ( shift-h>=0 )
              Si=r*r*acos(fabs(shift-h)/r)-
      r*fabs(h-shift)*sqrt(1-(fabs(shift-h)/r)*(fabs(shift-h)/r) );
            else
              Si=PI*r*r-r*r*acos(fabs(shift-h)/r)+
      r*fabs(h-shift)*sqrt(1-(fabs(shift-h)/r)*(fabs(shift-h)/r) );
          }
        }
      }

      S = S + Si;
    }
  }
```

```
  return S; //returns area of holes in the domain wall at the x
crossection
}


double DWvolume(double h, int N_Y, double x, double d,T_struct*
struc)
{
  // Integration using trapezium rule

  int N_x; //int N_x=50;//step of integration must not be more then
step on x
  int i;
  double h_x;
  double h_x0=0.001; //double h_x0=d/(2*400);
  double x_i;
  double V,DW,pDW;
  double x_t;
  x_t = DWthickness(h);

  N_x=m_div(x_t,h_x0)+1; //h_x=x_t/(N_x-1);
  h_x=x_t/N_x;

  V=0;

  pDW=DWarea(h,N_Y,x,d,struc);

  for(i=1;i<N_x+1;i++)
  {
    x_i=x+h_x*i;
    DW=DWarea(h,N_Y,x_i,d,struc);
    V=V+(DW+pDW)*h_x/2;
    pDW=DW;
  }


  return V;

  // Integration using mean values
  /*
    int i,j,n;
    int N_x;
    double h_x, x_i, p, q;
    double h_x0=d/(2*500);
    double integral[3];
    double F, V, DW;


      N_x=m_div(x_t,h_x0)+1;


      for (j=0; j<3; j++)
       {
          h_x=pow(0.5,j)*x_t/N_x;

          F=0;
            for (i=1; i<N_x+1; i++)
           {
                x_i=x+h_x/2+(i-1)*h_x;
                DW=DWarea(h,N_Y,x_i,d);
                F=F+DW*h_x;
```

```
             }

            integral[j]=F;
       }
     q=(integral[2]-integral[1])/(integral[1]-integral[0]);
     p=log(q)/log(0.5);
     V=integral[0]+(integral[0]-integral[1])*(integral[0]-
integral[1])/(2*integral[1]-integral[0]-integral[2]);

     return integral[0];
  */
}

double Coercivity(double h,int N_Y, double d,T_struct* struc)
{

  double x;
  double h_x=0.001;
  double x_st;
  double x_end;
  double sqP;

  double DW,pDW,nDW;

  double DerDW;

  double maxD;
  double max;
  double fi;

  fi=struc->fi_y;//sqrt(3)*d/2;

  x_st=7*d;
  x_end=9*d;

  sqP=h*(fi*(N_Y-1)+d);
  pDW=sqP-DWarea(h,N_Y,x_st,d,struc);
  DW =sqP-DWarea(h,N_Y,x_st+h_x,d,struc);

  maxD=(DW-pDW)/(h_x);
  max=maxD;

  pDW=DW;

  for (x=x_st+2*h_x; x<x_end;x+=h_x)
  {
    DW= sqP-DWarea(h,N_Y,x,d,struc);

    DerDW=(DW-pDW)/(h_x);

    if (maxD<DerDW)
    {
      maxD=DerDW;
      max=DerDW/DW;
    }

    pDW=DW;

  }
  return max;
```

```
}


double CoercivityT(double h,int N_Y,double d,T_struct* struc)
{

  double x;
  double h_x=0.01;
  double x_st;
  double x_end;
  double volP;
  double x_t;
  double x_t0 = 130e-3;
  double l_ex = 4e-3;
  double gamma;
  double DW,pDW,nDW;

  double DerDW;

  double max;
  double maxD;
  double fi;

  fi=struc->fi_y;//sqrt(3)*d/2;

  x_st=7*d;
  x_end=9*d;
  x_t = DWthickness(h);
  volP=h*(fi*(N_Y-1)+d)*x_t;
  gamma =
0.5*((x_t/x_t0+x_t0/x_t)+x_t*x_t*x_t0/(PI*PI*l_ex*(x_t+h)));
  pDW=volP-DWvolume(h,N_Y,x_st,d,struc);
  //pDW=volP-DWvolume(h,N_Y,x_st, x_t,d,struc);
  DW =volP-DWvolume(h,N_Y,x_st+h_x,d,struc);
  //DW =volP-DWvolume(h,N_Y,x_st+h_x,x_t,d,struc);

  maxD=gamma*(DW-pDW)/(h_x*(h*N_Y*d*x_t-
DWvolume(h,N_Y,x_st,d,struc)));
  //maxD=(DW-pDW)/(h_x*(h*N_Y*d-DWarea(h,N_Y,x_st+h_x/2,d,struc)));
  max=maxD;

  pDW=DW;

  for (x=x_st+2*h_x; x<x_end;x+=h_x)
  {
    DW=volP-DWvolume(h,N_Y,x,d,struc);
    //DW=volP-DWvolume(h,N_Y,x+h_x,x_t,d,struc);

    DerDW=gamma*(DW-pDW)/(h_x*(h*N_Y*d*x_t-
DWvolume(h,N_Y,x_st,d,struc)));
    //DerDW=(DW-pDW)/(h_x*(h*N_Y*d-DWarea(h,N_Y,x+h_x/2,d,struc)));

    if (maxD<DerDW)
    {
      maxD=DerDW;
      max=maxD;
    }

    pDW=DW;

  }
```

```
  return max;
}
int main()
{
  FILE* fp;
  FILE* fpCoer;
  FILE* fpCoerT;
  FILE* fpVol;

  T_struct struc;

  int N_Y=35; // number of balls in Y direction
  int N_X=50; // number of balls in X direction

  double d=0.5;
  double dh=0.01;
  double h=1.5; //z is changing from 0 to h with step dh

  double z;
  double x;
  double x_t=0.02; // DW thicknes

  double n;
  int i;
  char fname[10];
  InitStruct(&struc,FCC,d);
  /*  fpCoer=fopen("coercivity.dat","w+");
      for(z=0.01;z<h;z+=dh)
      {
            fprintf(fpCoer,"%f %f\n",z,Coercivity(z,N_Y,d,&struc));
      }
      fclose(fpCoer);
  */


  fpCoerT=fopen("coer.dat","w+");

  for(z=0.215;z<h;z+=dh)
  {
    printf("DWthickness w=%f   h=%f
Coer=%f\n",DWthickness(z),z,CoercivityT(z,N_Y,d,&struc));
    fprintf(fpCoerT,"%f %f\n",z,CoercivityT(z,N_Y,d,&struc));
  }

  fclose(fpCoerT);

  /*    fpCoerD=fopen("CoerDiam.dat","w+");
      for (d=0.01; d<20*x_t; d+=0.02)
        {
              n = d/x_t;
              fprintf(fpCoerD,"%f %f\n",n,CoercivityT(h,N_Y,x_t,d));
        }

        fclose(fpCoerD);



      for(h=200;h<=500;h+=10)
      {
            sprintf(fname,"DW%.2f.dat",h);
            printf("%s\n",fname);
```

```
            fp=fopen(fname,"w+");
            fp=fopen("suka.dat","w+");
            for(x=3;x<4;x+=0.01)
                fprintf(fp,"%f %f\n",x,DWarea(h,N_X,x,d,&struc));

            fclose(fp);
  //  }
  */
  fpVol=fopen("Volume.dat","w+");
  for (x=3;x<4;x+=0.01)
    fprintf(fpVol,"%f %f\n",x,DWvolume(h,N_Y,x,d,&struc));
  fclose(fpVol);
  return 0;
}
```

Appendix 2:

C++ code for calculation of the magnetostatic energy in an array of holes

```
#include <stdio.h>
#include <stdlib.h>
#include <string.h>
#include <math.h>

# define PI 3.1415926535897

double m_div(double x, double y)
{

        double n,ostatok;

        x=x/y;
        ostatok=modf(x,&n); //returns the rest and the int part of number x
        return n;
}


void TwoDCoordCube(int i, int j, double Center[2], double d)
{
        double X;
        double Y;
        double x0=0, y0=0;


        if (j%2==0)
                {
                        X=x0+i*d;
                        Y=y0+j*d;
          }
        if (j%2!=0)
                {
                        X=x0+i*d;
                        Y=y0+j*d;
                }
        Center[0]=X;
        Center[1]=Y;
}
```

```
/*-----------------------------------------------------------------------
 Procedure:    Potential_TwoD ID:1
 Purpose:      This function calculates a potential in the defined
            point fi_2 at the arbitrary hole from all
            other holes
 Input:        Magnetization of saturation - M;
            Diameter of the hole - d;
            Thichness of the film - h;
            Number of holes in X direction-1 - N_X;
            Number of holes in Y direction-1 - N_Y;
            Coordinates of the hole centre which used as a
            target - center2[3];
            Polar coordinate fi of the target point -
            fi_2;
Output:        Returns an overal ppotential at the target hole from
            all other holes - Psi;
Errors:
-----------------------------------------------------------------------*/
double Potential_TwoD( double M,
                                  double teta_M,
                                  double d,int N_X,int N_Y,
                                  double center2[2],
                                  double fi_2)
{
/* centre1[2] are coordinates of centres of holes we use as a sources of the
potential on hole with centre2[2]*/
 double Psi,pPsi_fi,Psi_fi, I_fi;
 double fi, center1[2];
 int Nfi = 180;
 int n, l;
 double h_fi;// step of integration for teta
 double R = d/3;// radius of holes

 double a,b,aa,bb;

 double errr, d_R;// d_R introduced to eliminate a divergence of potential
at the hole boundary

 h_fi = 2*PI/Nfi;

 errr = h_fi;
 d_R = 0.05;

 Psi = 0;

        for (l=0; l<=N_Y; l++)
              for (n=0; n<=N_X; n++)
              {
```

```
                          TwoDCoordCube(n,l,center1,d);

                                                aa = cos(fi_2);
                                                bb = sin(fi_2);

                                        I_fi = 0;

a = ((R+d_R)*aa-R*cos(0)+(center2[0]-center1[0]));  // fi starts from 0
b = ((R+d_R)*bb-R*sin(0)+(center2[1]-center1[1]));
pPsi_fi = M*R*cos(0-teta_M)/(4*PI*sqrt(a*a+b*b));

                                                for (fi = h_fi; fi<=2*PI; fi+=h_fi)
                                                {

                a = ((R+d_R)*aa-R*cos(fi)+(center2[0]-center1[0]));
                b = ((R+d_R)*bb-R*sin(fi)+(center2[1]-center1[1]));
                Psi_fi = M*R*cos(fi-teta_M)/(4*PI*sqrt(a*a+b*b));


                         I_fi = I_fi+(Psi_fi+pPsi_fi)*h_fi/2;
                                 pPsi_fi = Psi_fi;
                                                }
                                Psi = Psi +I_fi;

                         }


 return(Psi);
}

 double MSEnergy(double M,
                                 double teta_M,
                                int N_X, int N_Y,
                           double d)
{
int i,j;
int Nfi = 180;
double center2[2],fi,h_fi;
double R = d/3;
double U, U_fi, pU_fi, I_fi, Potential;

h_fi = 2*PI/Nfi;

U = 0;

           for (j=0; j<=N_Y; j++)
                for (i=0; i<=N_X; i++)
                {

                        TwoDCoordCube(i,j,center2,d);
```

```
                              I_fi = 0;

Potential = Potential_TwoD(M,teta_M,d,N_X,N_Y,center2,0);
pU_fi = 0.5*M*R*cos(0-teta_M)*Potential;

                              for (fi=h_fi; fi<=2*PI; fi+=h_fi)
                              {
     Potential = Potential_TwoD(M,teta_M,d,N_X,N_Y,center2,fi);
     U_fi = 0.5*M*R*cos(fi-teta_M)*Potential;
     I_fi = I_fi+(pU_fi+U_fi)*h_fi/2;
     pU_fi=U_fi;

                              }
          U = U + I_fi;
                         }
return(U);
}

void main()
{
 FILE* fpP;
 FILE* fp;
 FILE* fpU;

 double fi,center2[2],center1[2];
 double dfi=2*PI/180;
 double d = 2;
 double R = d/3;
 double M = 1;
 int N_X, N_Y;
 double teta;

fp=fopen("Poten.dat","w+");


          TwoDCoordCube(0,0,center2,d);

 for(fi=0; fi<2*PI;fi+=dfi)
      {
       fprintf(fp,"%f %f\n",fi,Potential_TwoD(M,0,d,0,0,center2,fi));

      }


 fclose(fp);


 fpU = fopen("MSE.dat","w+");
```

```
  N_X = 1;  // number of spheres in X direction - 1
  N_Y = 1;
  for (teta = 0; teta<=2*PI; teta+=PI/12)
        fprintf(fpU,"%f %f\n",teta,MSEnergy(M,teta,N_X,N_Y,d));

  fclose(fpU);

}
```